

SISSA

Scuola
Internazionale
Superiore di
Studi Avanzati

Physics Area - PhD course in
Statistical Physics

Harnessing long-range couplings for quantum technologies

Candidate:
Andrea Solfanelli

Advisors:
Stefano Ruffo
Nicolò Defenu

Academic Year 2023-2024



Contents

Preface	5
List of Publications	9
Acknowledgements	11
1 Long-range interacting quantum systems	13
1.1 Why long-range interactions?	13
1.2 Main features of long-range systems	15
1.2.1 Weak and Strong long-range regimes	15
1.2.2 The long-range spectrum	15
1.2.3 Universality of weak long-range systems	19
1.3 Experimental quantum simulation platforms	20
1.4 The quantum Ising chain with long-range interactions	22
1.4.1 Equilibrium properties	23
1.4.2 Dynamical properties	26
1.5 The Kitaev chain with long-range interactions	27
1.5.1 Equilibrium properties	28
1.5.2 Dynamical properties	32
2 The effective dimension approach	37
2.1 Effective dimension and scaling theory	37
2.2 Perturbative RG approach	40
2.3 Functional RG approach	41
2.4 Comparison with exact numerics	44
2.5 Closing remarks	45
3 Quantum Thermodynamics of long-range systems	47
3.1 Quantum thermodynamics	47
3.2 Quantum work statistics	48
3.3 Universal quantum work statistics in long-range systems	49
3.3.1 The sudden quench case	49
3.3.2 The slow quench case	51

3.3.3	Explicit examples of long-range advantage	54
3.4	Application to quantum heat-engines	58
3.4.1	The quantum Otto cycle	59
3.4.2	Adiabatic cycle	61
3.4.3	Heat Engine operation mode	64
3.4.4	Refrigerator operation mode	66
3.4.5	Finite time cycle	68
3.5	Closing remarks	71
4	Floquet Physics in long-range systems	73
4.1	Discrete Floquet time crystals	73
4.2	The long-range kicked quantum Ising chain	74
4.3	The strong long-range regime	76
4.3.1	Mean-field DFTC	76
4.3.2	Finite-size and finite-range effects	78
4.3.3	The order parameter	79
4.4	Quantum simulation with tunable interaction range	82
4.4.1	Stabilization of the DFTC response by increasing the interaction range	83
4.4.2	Quantum circuit implementation of the Floquet dynamics	83
4.4.3	Quantum circuit optimization	86
4.4.4	The role of noise and statistical errors	88
4.4.5	Noise mitigation and final results	91
4.5	Closing remarks	95
5	Entanglement in long-range systems	97
5.1	Entanglement in many-body quantum systems	97
5.2	Entanglement scaling in free fermionic systems	99
5.2.1	Rényi entropies and the correlation matrix	99
5.2.2	Matrix symbol of the correlation matrix	101
5.2.3	The Fisher-Hartwig expansion	102
5.2.4	Computation of the Fisher-Hartwig expansion coefficients	103
5.3	Entanglement scaling in the weak long-range regime	105
5.4	Entanglement scaling in the strong long-range regime	112
5.5	Closing remarks	117
6	Conclusions and outlooks	121

Preface

In this thesis, we delve into the unique properties of long-range interacting quantum systems. The research presented here is the culmination of a three-year PhD project, which contributes to the excitingly growing interest in long-range quantum systems. This interdisciplinary field bridges various research communities, including condensed matter physics, statistical physics, and quantum information theory.

The contribution of the present thesis is two-fold. From the fundamental side we probe the universal properties of long-range interacting quantum systems establishing a rich phenomenology which have no counter part in systems with local interactions. From the applicative point of view we identify some features which may be useful in the context of quantum technological applications, leading to several advantages with respect to standard local systems. Our transversal point of view, based on our statistical physics background, allowed us to bridge together many different subjects ranging from the out-of-equilibrium dynamics of many-body quantum systems to the theory of entanglement and quantum information. Moreover, we have explored for the first time the idea to obtain a thermodynamic advantage, coming from the presence of long-range couplings, in the context of quantum thermodynamics. Last but not least, during the PhD program, we had the opportunity to access the IBM superconducting quantum processors, this allowed us to go beyond theoretical predictions pursuing quantum simulation experiments directly on the physical hardware. The Thesis is organized as follows.

Chapter 1 is intended to summarize some known features of long-range interacting quantum systems. Section 1.1 presents the scope of the thesis and provides theoretical and experimental motivations for considering these systems as promising platforms for quantum technological applications. Section 1.2 introduces the distinction between weak and strong long-range interactions and discusses the peculiar spectral properties of long-range Hamiltonians. Section 1.3 reviews the current state of the art of experimental research in quantum computing and simulations, highlighting the pros and cons of various physical platforms, with a focus on atomic, molecular, and optical systems that allow for long-range couplings. Sections 1.4 and 1.5 detail the equilibrium and dynamical properties of two prototypical long-range models: the long-range quantum Ising chain and the long-range Kitaev chain.

Chapter 2 introduces and justifies the effective dimension approach to studying the

critical behavior of long-range systems. Section 2.1, reviews the derivation of the effective dimension relation using scaling theory and demonstrates its validity at leading order in a perturbative renormalization group (RG) analysis around the Gaussian fixed point. Section 2.2 applies known perturbative RG results to derive an explicit formula for the effective dimension, valid up to corrections of order $\mathcal{O}(\varepsilon^3)$. Section 2.3 presents a modern approach based on functional RG techniques, extending the effective dimension approximation beyond one-loop corrections by incorporating wavefunction renormalization effects. Section 2.4, compares the effective dimension approach predictions with numerical data from the conformal bootstrap for the two-dimensional Ising model with long-range interactions, demonstrating high accuracy.

Chapter 3 explores the quantum thermodynamics of long-range systems. Sections 3.1 and 3.2 introduce the field of quantum thermodynamics and the concept of quantum work statistics. Section 3.3 determines conditions under which long-range interactions reduce energy losses due to defect generation during non-adiabatic evolution, emphasizing their robustness against dynamic excitations compared to local systems. These findings are applied in Section 3.4 to optimize the performance of a finite-time quantum Otto cycle with a working substance featuring long-range couplings.

Chapter 4 presents results on Floquet physics in long-range systems. Section 4.1 introduces Discrete Floquet Time Crystals (DFTCs), a nonequilibrium many-body phase characterized by the breaking of discrete time translation symmetry and persistent oscillations of an order parameter. Section 4.2 introduces the long-range kicked quantum Ising chain as a prototypical model for studying Floquet-driven long-range systems. Section 4.3 explores the generation of DFTCs in clean systems with strong long-range interactions and introduces a novel order parameter for detecting these phases. This tool is applied to characterize the out-of-equilibrium phase diagram of the long-range kicked Ising model, revealing a rich landscape with self-similar fractal boundaries. Section 4.4 presents results from digital quantum simulations addressing qubit connectivity limitations in noisy intermediate-scale quantum devices, demonstrating how to implement couplings among physically disconnected qubits. This section also includes quantum simulation results on IBM superconducting quantum processors, benchmarking the prethermal stabilization of discrete Floquet time crystalline response with increasing interaction range.

Chapter 5 studies the behavior of the ground state entanglement entropy for Kitaev chains with long-range hopping and pairing couplings that decay as a power law of the distance. Sections 5.1 and 5.2 introduce the framework for the study of entanglement in many body quantum systems and review the main techniques for the analytic calculation of the entanglement scaling in lattice quadratic fermionic models. Sections 5.3 and 5.4 provide analytical and numerical characterizations of the ground state entanglement asymptotic growth in the large subsystem size limit, in the weak and strong long-range regimes respectively. This analysis reveals a rich phenomenology due to the model non-local nature. Notably, in the strong long-range regime, the system ground state can exhibit logarithmic, fractal, or volume-law entanglement scaling, depending on the values of the relevant

parameters.

The Thesis concludes with a summary of the main findings and potential future research directions in Chapter 6.

List of Publications

Chapter 2 of the present work is based on the following publications:

- [1] **A. Solfanelli**, N. Defenu, Universality in long-range interacting systems: the effective dimension approach, arXiv:2406.14651 (2024).

Chapter 3 of the present work is based on the following publications:

- [2] **A. Solfanelli**, N. Defenu, Universal work statistics in long-range interacting quantum systems, arXiv:2407.04101 (2024).
- [3] **A. Solfanelli**, G. Giachetti, M. Campisi, S. Ruffo, N. Defenu, Quantum heat engine with long-range advantages, New J. Phys. 25 033030 (2023).

Chapter 4 of the present work is based on the following publications:

- [4] G. Giachetti, **A. Solfanelli**, L. Correale, and N. Defenu, Fractal nature of high-order time crystal phases, Phys. Rev. B 108, L140102 (2023).
- [5] **A. Solfanelli**, S. Ruffo, S. Succi, N. Defenu, Stabilization of discrete time-crystalline response on a superconducting quantum computer by increasing the interaction range, Phys. Rev. Research 6, 013311 (2024).

Chapter 5 of the present work is based on the following publications:

- [6] **A. Solfanelli**, S. Ruffo, S. Succi, N. Defenu, Logarithmic, fractal and volume-law entanglement in a Kitaev chain with long-range hopping and pairing, J. High Energ. Phys. 2023, 66 (2023).

Other publications by the same author:

- [7] A. Santini, **A. Solfanelli**, S. Gherardini, M. Collura, Work statistics, quantum signatures, and enhanced work extraction in quadratic fermionic models, *Phys. Rev. B* 108, 104308 (2023).
- [8] A. Santini, **A. Solfanelli**, S. Gherardini, G. Giachetti, Observation of partial and infinite-temperature thermalization induced by repeated measurements on a quantum hardware, *J. Phys. Commun.* 7 065007 (2023).
- [9] A. Issoufou Arzika, **A. Solfanelli**, H. Schmid, S. Ruffo, Quantization of Integrable and Chaotic Three-Particle Fermi–Pasta–Ulam–Tsingou Models, *Entropy*, 25(3), 538 (2023).
- [10] H. Schmid, J. Dieplinger, **A. Solfanelli**, S. Succi and S. Ruffo, Tricritical point in the quantum Hamiltonian mean-field model, *Phys. Rev. E* 106, 024109 (2022).
- [11] **A. Solfanelli**, A. Santini, M. Campisi, Quantum thermodynamic method to purify a qubit on a quantum processing unit, *AVS Quantum Sci.* 4, 026802 (2022).
- [12] **A. Solfanelli**, A. Santini, M. Campisi, Experimental verification of fluctuation theorems with a quantum computer, *PRX Quantum* 2, 030353 (2021).
- [13] **A. Solfanelli**, M. Falsetti, M. Campisi, Nonadiabatic single-qubit quantum Otto engine, *Phys. Rev. B* 101, 054513 (2020).
- [14] **A. Solfanelli**, L. Buffoni, A. Cuccoli, M. Campisi, Maximal energy extraction via quantum measurement, *J. Stat. Mech.: Theory Exp.* 094003 (2019).
- [15] L. Buffoni, **A. Solfanelli**, P. Verrucchi, A. Cuccoli, M. Campisi, Quantum Measurement Cooling, *Phys. Rev. Lett.* 122 070603 (2019).

Acknowledgements

I would like to express my deepest gratitude to my supervisors, Prof. Stefano Ruffo and Prof. Nicolò Defenu, for their invaluable guidance, mentorship, and unwavering support throughout the course of my research. Their insights and encouragement have been instrumental in shaping both this work and my academic journey.

I am also profoundly thankful to all my collaborators, whose contributions have enriched this research. A special mention goes to Prof. Sauro Succi for providing me with the opportunity to access the IBM quantum processors, which played a pivotal role in advancing my work. I am equally indebted to Prof. Michele Campisi, my bachelor and master thesis advisor, whose passion for quantum thermodynamics has been a constant source of inspiration and has left an indelible mark on my academic career.

I extend my heartfelt thanks to my friends, who have been my pillars of support during these years in Trieste. I am particularly grateful to Alessandro, Giulio, Guido, Francesco, Elaheh, Cristiano, Anna, Chiara, and Cecilia. Their presence and companionship have been invaluable, and they were always there when I needed them the most, making this journey more enjoyable and meaningful.

Finally I wish to thank my parents who have always stood by my side throughout my studies, with their support and love.

Chapter 1

Long-range interacting quantum systems

1.1 Why long-range interactions?

The interest for long-range physics has steadily risen in recent years, driven by continuous advancements in experimental techniques for controlling and manipulating atomic, molecular, and optical (AMO) systems [16]. Specifically, experimental platforms such as Rydberg atoms [17], dipolar quantum gases [18], polar molecules [19], quantum gases coupled to optical cavities [20, 21], and trapped ions [22, 23, 24] have successfully realized ensembles of long-range interacting quantum particles.

These systems are powerful tools for quantum computing and quantum simulation because they enable the realization of highly entangled dynamical states [25, 26, 27]. Long-range interactions are crucial in these technological applications, as their collective nature leads to metastable states and novel forms of dynamical scaling not observed in systems with only local interactions. The physics of long-range interacting atomic assemblies provides a route to circumventing constraints such as thermalization and fast decoherence, making them promising candidates for efficient quantum technologies.

Two core questions emerge from this perspective:

1. **What novel phenomena, induced by long-range couplings, display many-body quantum correlations and may serve as proper tool for quantum information?**
2. **Which regimes are most suitable for exploiting the stability of long-range systems against external perturbations and their resilience against fast thermalization?**

These questions are the main motivation of the work presented in this Thesis. We address them by investigating the unique properties of long-range interacting quantum sys-

tems, focusing on identifying potential advantages that harness the presence of long-range coupling to enhance their utility for quantum technological applications. Additionally, we explore the universal behavior of these non-local systems near quantum critical points, aiming to isolate universal features applicable to a wide range of experimentally relevant long-range systems, regardless of the microscopic details of the model. To this end, we employ the effective dimension framework, which is introduced and justified in Chapter 2.

We focus on three main aspects of long-range systems that lead to explicit advantages over their local counterparts:

- **Quantum Thermodynamics:** One primary goal of quantum thermodynamics is developing efficient microscopic thermodynamic machines operating in the quantum regime. A significant limitation of such devices is the unavoidable trade-off between power and efficiency in finite-time thermodynamic cycles. Long-range systems stability against external perturbations reduces energy losses due to defect generation during non-adiabatic evolution, crucial for enhancing the power-to-efficiency ratio of quantum thermal devices. The quantum thermodynamics of long-range systems and its application to optimizing a finite-time quantum thermal cycle are discussed in Chapter 3.
- **Stabilization of out-of-equilibrium phases:** The efficacy of quantum technological applications depends on the ability to preserve systems out-of-equilibrium, avoiding the detrimental effects of thermalization, which lead to the loss of locally stored quantum information. Long-range systems can host long-lived quasi-stationary states with lifetimes diverging with system size, making them promising candidates for this purpose. Specifically, in periodically (Floquet) driven many-body quantum systems, long-range interactions allow the stabilization of Discrete Floquet Time Crystals (DFTCs), which are nonequilibrium many-body phases exhibiting a unique form of spatiotemporal order. The discrete time translation symmetry of the Floquet driving is broken, and an order parameter displays persistent oscillations with a period that is an integer multiple of the driving period. The Floquet physics of long-range interacting quantum systems is analyzed in Chapter 4 from both theoretical and quantum simulation perspectives.
- **Highly entangled states:** A crucial feature for systems used in quantum technologies is the ability to host highly entangled states. However, the ground state of local Hamiltonians is constrained by the entanglement area law. Long-range couplings overcome this limitation, allowing for violations of the area law even outside criticality. In Chapter 5, we provide a comprehensive analytical and numerical characterization of the asymptotic growth of ground state entanglement in the large subsystem size limit. The truly non-local nature of the model leads to an extremely rich phenomenology, with the ground state potentially exhibiting logarithmic, fractal, or volume-law entanglement scaling, depending on the relevant parameters.

1.2 Main features of long-range systems

1.2.1 Weak and Strong long-range regimes

A physical system is said to be long-range when the coupling matrix J_{ij} decays as a power law of the distance $r = |i - j|$ between the microscopic components:

$$J_{ij} \propto r^{-\alpha}/N_\alpha, \quad \text{with } \alpha > 0, \quad N_\alpha = \sum_{j=1}^n j^{-\alpha}, \quad (1.1)$$

where the factor N_α is introduced to ensure that the internal energy remains extensive [28]. In a d dimensional system, depending on the value of the decay exponent α , three different regimes can be identified:

- **The strong long range regime** ($0 < \alpha < d$): The system energy is non-additive, and standard thermodynamics is not strictly valid [29, 30].
- **The weak long range regime** ($d < \alpha < \alpha^*$): In this regime, thermodynamics is well-defined, but long-range interactions significantly affect phase transitions and the universal scaling near classical and quantum critical points [31, 32, 33, 34]. The threshold value α^* depends on the specific model and phenomenon considered.
- **Short-range regime** ($\alpha > \alpha^*$): The system's behavior mimics that of nearest-neighbor interactions.

1.2.2 The long-range spectrum

As a first minimal model of long-range quantum system we consider a generic system of particles hopping on a one-dimensional ($d = 1$) lattice with long-range translational invariant hopping amplitudes and possibly interacting among each other. This model is described by the Hamiltonian

$$\hat{H} = - \sum_{i=1}^N \sum_{i=1}^{N/2-1} t_r \left(\hat{a}_i^\dagger \hat{a}_{i+r} + h.c. \right) + \mu \sum_{i=1}^N \hat{a}_i^\dagger \hat{a}_i + \hat{H}_{\text{int}}. \quad (1.2)$$

where the \hat{a}_i^\dagger (\hat{a}_i) are the creation (annihilation) operators for quantum particles at site i of the chain and N is the total number of sites. The nature of the particles (bosons or fermions) and the specific form of the interaction Hamiltonian \hat{H}_{int} are not crucial at this stage. The long-range hopping amplitudes are defined as in Eq. (1.1).

In general, the spectrum of the interacting Hamiltonian in Eq. (1.2) can be obtained by means of perturbation theory [35]. Then, we start by diagonalizing the noninteracting part.

Assuming periodic boundary conditions, the spectrum of the noninteracting Hamiltonian is

$$\varepsilon_\alpha(k) = \mu - f_\alpha(k), \quad (1.3)$$

where

$$f_\alpha(k) = \frac{1}{N_\alpha} \sum_{r=1}^{N/2-1} \frac{\cos(kr)}{r^\alpha}, \quad (1.4)$$

is the Fourier transform of the hopping amplitudes t_r . The periodic boundary conditions impose the usual restriction on the momentum $k \equiv k_n = 2\pi n/N$ with $n \in \mathbb{Z}$ and $n = \lfloor -N/2 \rfloor, \dots, \lfloor N/2 \rfloor$ (the lattice spacing has been set to 1).

As we will see throughout this manuscript, the behavior of $f_\alpha(k)$ for different values of α , plays a crucial role in the physics of long-range quantum systems, therefore it is worth spending this Section to characterize its peculiar behavior.

First of all we notice that the Kac normalization N_α scales differently with the system size $N \gg 1$ depending on α :

$$N_\alpha \approx \begin{cases} N^{1-\alpha}/c_\alpha & \text{if } \alpha < 1 \\ \ln N & \text{if } \alpha = 1, \\ \zeta(\alpha) & \text{if } \alpha > 1 \end{cases} \quad (1.5)$$

where $c_\alpha = (1 - \alpha)2^{1-\alpha}$ and $\zeta(x)$ is the Riemann zeta function.

As long as we are in the weak long-range regime $\alpha > 1$, the Kac scaling is finite in the $N \rightarrow \infty$ limit. Accordingly the calculation proceeds similarly to the nearest-neighbor case, allowing the thermodynamic limit of Eq. (1.4) to be taken safely, substituting the discrete momentum values k_n with the continuous variable $k \in [-\pi, \pi)$. Therefore, the spectrum of the Hamiltonian for $\alpha > 1$ becomes continuous and $f_\alpha(k)$ reads [36]

$$f_\alpha(k) \approx \frac{1}{\zeta(\alpha)} \left[\text{Li}_\alpha(e^{ik}) + \text{Li}_\alpha(e^{-ik}) \right] \quad (1.6)$$

where $\text{Li}_x(z) = \sum_{n=1}^{\infty} z^n/n^x$ is the polylogarithm [37].

While the specific choice of the lattice type may influence the detailed form of $f_\alpha(k)$, the physics of long-range interacting systems is typically affected only by its asymptotic behavior at low energy. In particular, we are interested in the low k modes of the single particle spectrum, which determine the dispersion relation of the long-range system. This

is obtained by taking the Taylor expansion of Eq. 1.6 around $k = 0$ leading to [36]

$$f_\alpha(k) = 1 + \sin\left(\frac{\alpha\pi}{2}\right) \frac{\Gamma(1-\alpha)}{\zeta(\alpha)} |k|^{\alpha-1} + \mathcal{O}(k^2) \quad \text{if } 1 < \alpha < 3, \quad (1.7)$$

$$f_\alpha(k) = 1 + \frac{2\ln(k) - 3}{4\zeta(3)} k^2 + \mathcal{O}(k^3) \quad \text{if } \alpha = 3, \quad (1.8)$$

$$f_\alpha(k) = 1 - \frac{\zeta(\alpha-2)}{2\zeta(\alpha)} k^2 + \mathcal{O}(k^{\alpha-1}) \quad \text{if } \alpha > 3. \quad (1.9)$$

Then, at the gapless point $\mu = 1$, we find the α dependent dispersion relation $\varepsilon_\alpha(k) \approx |k|^{\alpha-1}$, as long as $\alpha < 3$, while we retrieve the standard dispersion relation for a nearest neighbor tight binding model $\varepsilon_\alpha(k) \approx |k|^2$ when $\alpha > 3$. Once the dispersion relation is known we can compute the low energy density of states as

$$g(\varepsilon) = \int_{-\pi}^{\pi} \frac{dk}{2\pi} \delta(\varepsilon - \varepsilon_\alpha(k)) \approx \begin{cases} g_\alpha \varepsilon^{\frac{1}{\alpha-1}-1} & 1 < \alpha < 3 \\ \varepsilon^{-1/2} & \alpha > 3 \end{cases}, \quad (1.10)$$

with $g_\alpha = (\sin(\alpha\pi/2) \Gamma(1-\alpha) \zeta(\alpha))^{-1/(\alpha-1)} / (\alpha-1)$. This result can be compared with the standard power-law scaling of the density of states in a local system, leading to the definition of the spectral dimension [38, 39]

$$g(\varepsilon) \approx \varepsilon^{d_s/2-1}. \quad (1.11)$$

This is the first example of the dimensional correspondence relating the behavior of a long-range system in $d = 1$ dimensions to that of a local system in an effective fractional dimension

$$d_{\text{eff}} = d_s = \begin{cases} 2/(\alpha-1) & \text{if } 1 < \alpha < 3 \\ 1 & \text{if } \alpha > 3 \end{cases}. \quad (1.12)$$

The threshold at which short-range physics is recovered, in this case $\alpha^* = 3$, corresponds to the value of α at which the effective dimension matches the actual spatial dimension of the system.

As we will explore in the following sections of this manuscript, this identification, which naturally arises from the fundamental spectral properties of long-range systems, proves to be a powerful tool for investigating and interpreting the universal properties of these systems (see Chapter 2).

The situation changes dramatically in the strong long-range regime $\alpha < 1$. Indeed, as shown in Eq. (1.5), the Kac normalization factor N_α diverges at large N ensuring energy extensivity. Accordingly, the thermodynamic limit of Eq. (1.4) must be carefully considered. To this aim, it is convenient to write Eq. (1.4) explicitly for large N as

$$\lim_{N \rightarrow \infty} \frac{1}{N_\alpha} \sum_{r=1}^{N/2-1} \frac{\cos(kr)}{r^\alpha} \approx \frac{c_\alpha}{N} \sum_{r=1}^{N/2} \frac{\cos(2\pi n \frac{r}{N})}{(r/N)^\alpha}. \quad (1.13)$$

Due to the $1/N$ scaling of the discrete momenta on the lattice, the summation depends only on the variable r/N . Therefore, for $N \rightarrow \infty$, we can take the continuum limit by transforming the sum over r into an integral with respect to $s = r/N$, leading to

$$f_\alpha(n) = \lim_{N \rightarrow \infty} f_\alpha(k) = \int_0^{1/2} ds \frac{\cos(2\pi ns)}{s^\alpha}. \quad (1.14)$$

Despite its simplicity, the result in Eq. (1.14) has profound physical implications: it demonstrates that the spectrum of a quantum system with long-range harmonic couplings remains discrete even as $N \rightarrow \infty$. Specifically, for $\alpha < 1$, the gap between neighboring eigenvalues $\varepsilon_{n+1} - \varepsilon_n$, labeled by the consecutive momenta k_n, k_{n+1} in Eq. (1.4), does not vanish in the thermodynamic limit, as it would for $\alpha > 1$. Consequently, the energy eigenvalues depend only on the integer index $n \in \mathbb{Z}$ rather than on the continuous momentum k :

$$\varepsilon_n = \mu - f_\alpha(n). \quad (1.15)$$

Notably, for $\alpha = 0$, we find that $f_\alpha(n) \rightarrow \delta_{n,0}$, leading to a fully degenerate discrete spectrum as described by Eq. (1.15): $\varepsilon_n = \mu$ for $n \neq 0$ and $\varepsilon_n = \mu - 1$ for $n = 0$. Additionally, it is important to observe that the energies ε_n are not densely distributed. Instead, each energy eigenvalue is isolated, with the only accumulation point occurring at the maximum energy $\max_n \varepsilon_n = \mu$. This follows from the Riemann–Lebesgue lemma [40], which implies

$$\lim_{n \rightarrow \infty} f_\alpha(n) = 0. \quad (1.16)$$

The core result in Eq. (1.14) remains robust regardless of the nature of the particles (bosons or fermions) or most interaction terms \hat{H}_{int} . This claim can be substantiated by examining the perturbative corrections to the eigenvalues of the Hamiltonian induced by the interaction term \hat{H}_{int}

$$\delta E_n = \langle \psi_n | \hat{H}_{\text{int}} | \psi_n \rangle + \sum_{n \neq n'} \frac{|\langle \psi_n | \hat{H}_{\text{int}} | \psi'_n \rangle|^2}{E_n - E_{n'}} + \dots \quad (1.17)$$

Here, $|\psi_n\rangle$ are the symmetric (or antisymmetric) products of the single-particle eigenstates $|k_n\rangle$ of the periodic chain, and E_n represents their energy. As long as the system is finite, the spectrum can be safely assumed to be discrete and nondegenerate, making the perturbative results a good approximation for the spectrum of \hat{H} under weak perturbations.

Conventionally, one might expect perturbative arguments to break down in the thermodynamic limit due to divergent contributions near critical points. However, this is not the case for strongly long-range systems, where the long-range nature of the couplings suppresses strong fluctuations [41]. Consequently, the discreteness of the noninteracting spectrum persists in the thermodynamic limit, and the perturbative contributions on the

right-hand side of Eq. (1.17), should not develop any divergence. Therefore, the discreteness of the spectrum, is expected to persist in most interacting Hamiltonians. One of the main consequences of discreteness is the suppression of strong interaction contributions in perturbation theory. Thus, the physics of thermodynamically large long-range systems resembles the one of a finite bounded Hamiltonian more closely than that of short-range many-body systems.

Summarizing, the shape of $f_\alpha(k)$ shrinks from $f_{\alpha \rightarrow \infty}(k) = \cos(k)$ (for $\alpha \rightarrow \infty$) to $f_{\alpha \rightarrow 0}(k) = \delta_{k,0}$, becoming increasingly singular at $k = 0$ as α is decreased. Moreover, in the strong long-range regime ($0 < \alpha < d$), we find that the excitation spectrum takes discrete values also in the thermodynamic limit $N \rightarrow \infty$ and that $f_\alpha(k)$ squeezes towards a delta function as $N \rightarrow \infty$ with a speed $N^{-(1-\alpha)}$ for $\alpha < 1$ and $1/\ln N$ for $\alpha = 1$. This phenomenon can be explained by the slow decay of interactions with spatial distance, which results in the system behaving like a permutationally invariant system over finite length scales. Consequently, observables cannot distinguish finite wavelengths, and only modes with extensive wavelengths $k_n \propto 1/N$, have a significant impact on physical properties. As α increases beyond d , all modes $k \neq 0$ eventually become activated.

1.2.3 Universality of weak long-range systems

The presence of non-local interactions $J(r) \propto r^{-\alpha}$ may alter the standard picture provided by the Mermin-Wagner theorem [42] allowing for transition at dimensions smaller than the lower critical one for local systems [43], as observed in various experiments [44, 45]. Depending on the parameter α three regimes can be identified: (i) for $\alpha \leq \alpha_{\text{mf}}$, where α_{mf} can be calculated in the mean-field approximation, the mean-field approximation correctly describes the universal behavior; (ii) for $\alpha_{\text{mf}} < \alpha \leq \alpha^*$ the system exhibits peculiar long-range critical exponents; (iii) for $\alpha > \alpha^*$ the critical behavior corresponds to the nearest-neighbors ($\alpha \rightarrow \infty$) one.

The effective dimension approach provides an intriguing framework for interpreting these findings. This concept suggests that the critical properties of a long-range model in dimension d with a power-law exponent α can be deduced from those of a short-range model in an effective fractional dimension d_{eff} . A relation linking this effective dimension to d and α can be determined through general renormalization group arguments leading to [46]

$$d_{\text{eff}} = \frac{d(p - \eta_{\text{SR}}(d_{\text{eff}}))}{\alpha - d}, \quad (1.18)$$

where p is the power of the low-energy dispersion relation of the short-range single particle spectrum.

A key advantage of the effective dimension approach is its ability to reproduce behaviors both within and beyond the mean-field approximation range by varying a single parameter [46]. Moreover, although Eq. (1.18) is not exact for non-Gaussian fixed points,

it serves as a highly accurate approximation. It offers an efficient means to estimate critical exponents with minimal error, achieving an accuracy higher than 97% for equilibrium critical exponents when compared to precise numerical estimates.

In Chapter 2 we provide a detailed introduction to the effective dimension framework from a renormalization group perspective and we justify the validity of the approximation leading to the dimensional correspondence in Eq. (1.18).

1.3 Experimental quantum simulation platforms

From the experimental side several platforms exist with the possibility to implement long-range couplings. In particular, in this Section we briefly summarize the current state of experimental setups for quantum technological applications with a specific focus on the physical systems which naturally host long-range interactions.

In the past decade various platforms have successfully implemented universal quantum gates and precise readouts, meeting the Di Vincenzo criteria [47]. Ongoing hardware and fabrication developments have facilitated qubit integration, enabling prototype demonstrations in quantum computing, including analog/digital quantum simulation, quantum error correction (QEC), fault-tolerant quantum operations, and quantum algorithms.

Google’s first claim of quantum supremacy, demonstrated by randomized circuit sampling on their 53-qubit Sycamore processor [48], stands as a pivotal moment in this journey. Followed by other ”quantum advantage” experiments, spanning superconducting systems [49, 50] and photon-based approaches [51, 52, 53]. Quantum annealing in commercialized quantum machines, such as D-Wave annealing machines [54] and photonic boson sampling circuits [51, 52, 53], have propelled the industrialization of quantum computing. Functional quantum simulators [55, 56] addressing preliminary problems in quantum chemistry [57] and condensed matter physics [58], stand as additional noteworthy achievements. Moreover, several experimental platforms have been explored for quantum computing, including trapped ions [60, 61, 62, 63], neutral Rydberg atoms [64, 65, 66], coherent photons [67, 52], nuclear spins in molecules [68, 69], NV centers [70, 71], semiconductor quantum dots [72], and superconducting qubits [73, 74, 75]. Each platform has distinct advantages and drawbacks [59]. Figure 1.1, shows a schematic representation of different platforms for quantum computing. Here, we will focus on only three of them which are more suited for many-body quantum simulation: superconducting qubits (Fig. 1.1a), trapped ions (Fig. 1.1b) and Rydberg atoms (Fig. 1.1e).

Superconducting qubits are relatively easy to fabricate and can be densely packed, allowing for the construction of large-scale quantum computers. This makes them a promising platform for scaling up quantum computing applications [75]. Moreover, they can be manipulated using a wide range of microwave frequencies, making them versatile and flexible for implementing various quantum gates [73]. The number of quantum simulations implemented on noisy superconducting devices has steadily risen in recent years,

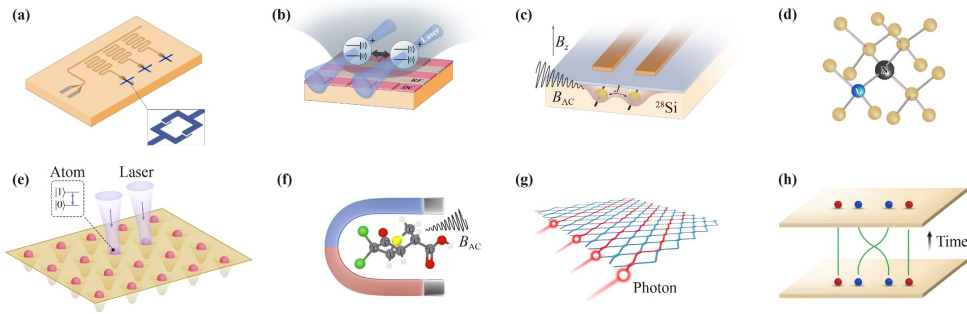


Figure 1.1: Schematic representation of different platforms for quantum computing: a) superconducting qubits, b) trapped ions, c) electron or hole spins in semiconductor (silicon) quantum dot, d) NV centers, e) Rydberg atoms, f) nuclear spins in molecules, g) photons h) topological quantum computing (physical system not found yet). Figure adapted from Ref. [59].

also thanks to the possibility to easily access these machines from remote, for example through the python based Qiskit package [76] which allows access to IBM quantum machines. A significant challenge for superconducting devices lies in their limited connectivity, since superconducting qubits are typically arranged in a one or two-dimensional grid with nearest-neighbor couplings, making them often unsuitable to target long-range enabled phenomena. In principle, to overcome this limitation, one could harness the universality of native gates for implementing couplings among physically disconnected qubits. However, this approach comes at the expense of increased circuit depth, subsequently amplifying the noise that impacts the raw quantum simulation results (see Section 4.4). To efficiently pursue this strategy, there is a critical need for enhanced noise mitigation techniques [77]. These techniques are essential to consider the influence of noise and subsequently eliminate its detrimental effects from the experimental data.

Trapped-ion systems, which involve laser-cooled atomic ions confined in ultra-high vacuum setups, provide an excellent degree of isolation from external noise sources. These systems encode high-fidelity qubits in stable pairs of electronic energy levels for each ion, resulting in long coherence times [78] and the possibility to be initialized and measured with extremely high fidelity [79]. Quantum processors built upon ion-based platforms have demonstrated efficient manipulation capabilities, handling dozens of qubits effectively [80, 81]. The prowess of ion-based systems has been exemplified in small-scale implementations of quantum algorithms, showcasing achievements such as Shor’s algorithm and Grover’s search algorithm [82, 83]. Furthermore, ion-based quantum simulators have successfully reached up to 53 qubits, enabling exploration into novel aspects of complex many-body quantum spin models [24]. Notably, trapped ions qubits exhibit long-range phonon-mediated interactions, with the coupling matrix decay, denoted as J_{ij} , following a

System	α	Comments
Trapped ions systems	$\sim 0-3$	Phonon mediated interactions
Dipolar Gases	3	Anisotropic interactions
Single-mode cavity QED systems	0	Cavity photons mediated interactions

Table 1.1: Table listing different applications where systems are governed by long-range interactions. Table adapted from Ref. [16].

power law of the distance $r = |i - j|$: $J_{ij} \propto r^{-\alpha}$. In this perspective, trapped ions are an extremely versatile tool as they allow the simulation of the entire $0 \lesssim \alpha \lesssim 3$ range.

Neutral atom arrays have emerged as a promising platform for quantum computing and particularly for quantum simulation [17]. Controlled interactions between atomic qubits are mediated by the long-range dipole-dipole interactions via Rydberg states. The inherent property of long-range Rydberg interactions enables the creation of specific quantum Hamiltonians, fostering straightforward analog quantum simulations. This distinctive feature, intrinsic to the atoms, plays a crucial role in entanglement generation within the simulator. The scalability of this model, demonstrated through experiments involving hundreds of atoms [66, 84, 85], establishes Rydberg atom arrays as a robust and versatile tool, capable to simulate complex phases of matter such as topological spin liquids [86].

Finally, quantum gases in cavities can be used to engineer all-to-all interacting, fully-connected models [87, 21], such as the Lipkin-Meshov-Glick model [88] or the Hamiltonian Mean Field model [89, 90]. Such systems are formed by neutral Bose-Einstein condensates inside an optical cavity and illuminated by a transverse standing-wave laser field, far-detuned from the atomic resonance so that the condensate behaves as a dielectric medium. By tuning the frequency of the cavity frequency, the atoms of the condensate effectively interact by scattering photons in the cavity mode and back. As such photons are delocalized over the cavity mode, this interaction is flat.

1.4 The quantum Ising chain with long-range interactions

All the experimental platforms described in the previous section, under suitable approximations, can be described in terms of a long-range spin Hamiltonian

$$\hat{H} = -\frac{1}{2} \sum_{\mu, i \neq j} J_{ij}^{\mu} \hat{\sigma}_i^{\mu} \hat{\sigma}_j^{\mu} - \sum_i \mathbf{h} \cdot \hat{\sigma}_i, \quad (1.19)$$

where the indices i, j run over the n sites of a d -dimensional lattice and $\hat{\sigma}_i^{\mu}$ represents the $\mu \in \{x, y, z\}$ components of a spin-1/2 operator, i.e. $\boldsymbol{\sigma} = (\hat{\sigma}^x, \hat{\sigma}^y, \hat{\sigma}^z)$ [21, 24, 91]. While the coupling matrices J_{ij}^{μ} can, in principle, be engineered to depend on the index μ . In this thesis we will focus on the case in which $J_{ij}^{y,z} = 0$, $J_{ij}^x = J_{ij}$ and $h^{x,y} = 0$, $h^z = h$,

namely the long-range quantum Ising model in a transverse field. Moreover, we consider the long-range coupling matrix introduced in Sec. 1.2.1, i.e., $J_{ij} \propto |i - j|^{-\alpha}$.

For ferromagnetic interactions $J_{i,j} \geq 0$ the system has an equilibrium zero-temperature phase transition for small enough $|h|$, associated with the spontaneous breaking of its \mathbb{Z}_2 spin-inversion symmetry of the x -component. The longitudinal magnetization $m_x = \langle \hat{\sigma}_j^x \rangle$ undergoes an abrupt change from $m_x = 0$ in the unique paramagnetic ground state for $|h| > h_c$ to $m_x = \pm m(h) \neq 0$ in the two degenerate ferromagnetic ground states for $|h| < h_c$.

1.4.1 Equilibrium properties

Let us start analysing this model from the strong long-range regime, with $\alpha < d$. For simplicity, we first consider the case of a completely flat interaction with $\alpha = 0$. In this case the Hamiltonian can be more conveniently written in terms of the total spin operators

$$S_\mu = \sum_i \sigma_i^\mu, \quad \mu = x, y, z, \quad (1.20)$$

and $\hat{\mathbf{S}} = (\hat{S}_x, \hat{S}_y, \hat{S}_z)$, leading to the so called Lipkin-Meshkov-Glick (LMG) Hamiltonian

$$\hat{H}_0 = -\frac{S_x^2}{N} + hS_z \quad (1.21)$$

This expression highlights that the $\alpha = 0$ Hamiltonian is a function of a single degree of freedom: the collective spin. All other non-collective spin modes are frozen. The collective spin magnitude $\hat{\mathbf{S}}^2 = \hat{S}_x^2 + \hat{S}_y^2 + \hat{S}_z^2 = S(S + 1)$, with $S = N/2, N/2 - 1, \dots, 0$ or $1/2$, is conserved $[\mathbf{S}^2, \hat{H}_0] = 0$. Moreover, it is crucial to notice that for all states with a spin magnitude S which grows with N , the thermodynamic limit $N \rightarrow \infty$ is equivalent to a semiclassical limit. Indeed, the rescaled spin satisfies commutation relations of the form [92]

$$\left[\frac{\hat{S}_\mu}{S}, \frac{\hat{S}_\nu}{S} \right] = \frac{i}{S} \epsilon_{\mu\nu\rho} \frac{\hat{S}_\rho}{S} \quad (1.22)$$

Thus, the system has an effective Planck constant $\hbar_{\text{eff}} = 1/S$ and the limit $N \rightarrow \infty$ realizes a classical limit with a continuous spin $\langle \hat{\mathbf{S}} \rangle / S \rightarrow \mathbf{S}_{\text{cl}}$ of (conserved) length 1.

The absolute ground state minimizes energy across all sectors, for ferromagnetic interactions the ground state is realized for maximal collective spin polarization, $S = N/2$. Moreover, as $N \rightarrow \infty$, the ground state expectation values $\langle \hat{\mathbf{S}} \rangle / S$ of the collective spin components converge to the minimum point \mathbf{S}_{cl}^* of the classical Hamiltonian \mathcal{H}_{cl} on the unit sphere [92].

It is convenient to define a rotated reference frame adapted to the ground state polarization, i.e., such that \mathbf{S}_{cl}^* is aligned in the new z -direction. Using spherical coordinates we can parametrize the rotation of the total spin coordinate frame as

$$\begin{pmatrix} \hat{S}_x \\ \hat{S}_y \\ \hat{S}_z \end{pmatrix} = \begin{pmatrix} \cos \theta \cos \phi & -\sin \phi & \sin \theta \cos \phi \\ \cos \theta \sin \phi & \cos \phi & \sin \theta \sin \phi \\ -\sin \theta & 0 & \cos \theta \end{pmatrix} \begin{pmatrix} \hat{\Sigma}_x \\ \hat{\Sigma}_y \\ \hat{\Sigma}_z \end{pmatrix}. \quad (1.23)$$

In particular the rotated coordinate frame is aligned with the equilibrium magnetization frame of the model by choosing

$$\theta = \begin{cases} 0 & \text{if } h > h_c \\ \arctan(h) & \text{if } h < h_c \end{cases}, \quad \phi = 0 \quad (1.24)$$

We are now in the position to consider the leading order quantum corrections to this classical limit. For this purpose we introduce the Holstein-Primakoff expansion, which shall be valid around the ground state of the LMG Hamiltonian. The expansion consists in expressing the rotated spin operator in terms of the variables of a quantum harmonic oscillator, i.e.,

$$\frac{\hat{\Sigma}_x}{N} = \frac{\hat{x}}{\sqrt{2N}} + \mathcal{O}(N^{-3/2}) = \frac{1}{\sqrt{2N}}(\hat{a}^\dagger + \hat{a}) + \mathcal{O}(N^{-3/2}), \quad (1.25a)$$

$$\frac{\hat{\Sigma}_y}{N} = \frac{\hat{p}}{\sqrt{2N}} + \mathcal{O}(N^{-3/2}) = \frac{i}{\sqrt{2N}}(\hat{a}^\dagger - \hat{a}) + \mathcal{O}(N^{-3/2}), \quad (1.25b)$$

$$\frac{\hat{\Sigma}_z}{N} = \frac{1}{2} - \frac{\hat{x}^2 + \hat{p}^2 - 1}{N} + \mathcal{O}(N^{-2}) = \frac{1}{2} - \frac{\hat{a}^\dagger \hat{a}}{N} + \mathcal{O}(N^{-2}), \quad (1.25c)$$

where \hat{x} , \hat{p} are fictitious position and momentum operators of an effective quantum harmonic oscillator that describes the quantum fluctuations of the rotated total spin operator in the proximity of the LMG ground state, while \hat{a}^\dagger and \hat{a} are the corresponding bosonic creation and annihilation operators, respectively.

In this way, using (1.25) to represent the LMG Hamiltonian, we obtain the following $1/N$ -expansion

$$\frac{\hat{H}_0}{N} \approx \mathcal{E}_0 + \frac{\hat{\mathcal{E}}_1}{\sqrt{N}} + \frac{\hat{\mathcal{E}}_2}{N} \quad (1.26)$$

where, under this approximation, all the higher-order terms in $1/N$ are neglected, and \mathcal{E}_l , with $l = 0, 1, 2$ depend on h , θ and ϕ . Then, choosing θ and ϕ as in Eq. (1.24) we obtain [93]

$$\mathcal{E}_0 = \begin{cases} -h & \text{if } h > h_c \\ -\frac{1+h^2}{2} & \text{if } h < h_c \end{cases}, \quad \hat{\mathcal{E}}_1 = 0, \quad \hat{\mathcal{E}}_2 = \frac{\hat{p}^2}{2m} + \frac{m}{2}\omega^2\hat{x}^2 + \delta e, \quad (1.27)$$

where

$$m = \begin{cases} 1/2h & \text{if } h > h_c \\ 1/2 & \text{if } h < h_c \end{cases}, \quad \omega = \begin{cases} 4h(h-1) & \text{if } h > h_c \\ 4(1-h^2) & \text{if } h < h_c \end{cases}, \quad \delta e = \begin{cases} h-1/2 & \text{if } h > h_c \\ 1/2 & \text{if } h < h_c \end{cases}. \quad (1.28)$$

As a result, the leading-order contribution of the LMG Hamiltonian to quantum fluctuations around the ground state, in terms of the Holstein-Primakoff expansion, is the term \mathcal{E}_2 which has the form of a harmonic oscillator with mass $m(h)$ and frequency $\omega(h)$. This can be diagonalized in terms of the creation and annihilation operators

$$\hat{b} = \sqrt{\frac{m\omega}{2}} \left(\hat{x} + \frac{i}{m\omega} \hat{p} \right), \quad \hat{b}^\dagger = \sqrt{\frac{m\omega}{2}} \left(\hat{x} - \frac{i}{m\omega} \hat{p} \right), \quad (1.29)$$

leading to the following form for the LMG Hamiltonian

$$\hat{H}_0 \approx N\mathcal{E}_0(h) + \delta e(h) + \omega(h)\hat{b}^\dagger\hat{b}. \quad (1.30)$$

where $\mathcal{E}_0(h)$ is the thermodynamic mean-field energy density, $\delta e(h)$ is a constant mean-field shift, while the quantum fluctuations are described by the quadratic harmonic oscillator term whose frequency is the gap $\omega(h)$.

To study the finite α corrections, we need to separate the contributions for $\alpha = 0$ and $\alpha \neq 0$:

$$H = H_{\alpha=0} + V_\alpha. \quad (1.31)$$

Next, we introduce the Fourier transform of the spin operators

$$\tilde{S}_k^\mu = \sum_j e^{ikj} \sigma_j^\mu, \quad \mu = x, y, z, \quad \tilde{S}_k^\pm = \sigma_x \pm i\sigma_y. \quad (1.32)$$

This leads to the expressions

$$V_\alpha = -\frac{J}{4N} \sum_{k \neq 0} f_\alpha(k) [S_k^+ S_{-k}^- + S_k^- S_{-k}^+ + S_k^+ S_{-k}^+ + S_k^- S_{-k}^-], \quad (1.33)$$

where the couplings are given by the function $f_\alpha(k)$, whose peculiar properties have been analyzed in detail in Section 1.2.2. In particular, $f_\alpha(k=0) = 1$ by construction, moreover as α approaches 0 the couplings $f_\alpha(k)$ decrease, and H reduces to a Hamiltonian describing a single collective degree of freedom, H_0 . When $\alpha \neq 0$ spatially modulated interactions couple the collective spin to all finite-wavelength modes representing spatially non-trivial spin fluctuations. Moreover, due to the peculiar nature of the couplings $f_\alpha(k)$, as we have seen in Section 1.2.2, as long as $\alpha < d$ long-range interactions preferentially generate coupling to long-wavelength modes only [94].

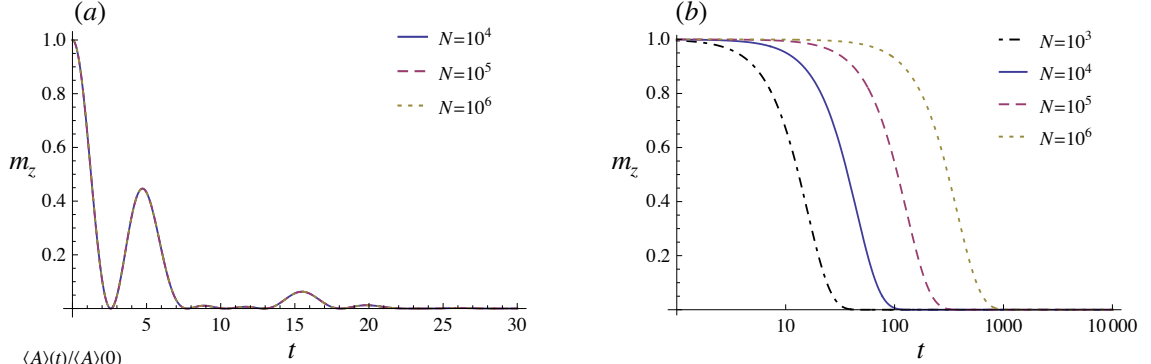


Figure 1.2: Time evolution of the expectation value of the transverse field magnetization m_z for a quench $h \rightarrow 0$ of the long-range quantum Ising chain, for different values of α and of the system size N . (a) $\alpha = 2$, an apparent decay is observed, superimposed over oscillations. The N dependence of the time evolution is so weak that the curves for the various system sizes cannot be discerned in the plot. (b) $\alpha = 0.5$, the expectation value again appears to be decaying, but on a time scale that depends strongly on the system size N (note the logarithmic scale). Figure adapted from Ref. [95].

1.4.2 Dynamical properties

The simplest evolution protocol we can think of for studying the dynamical properties of the long-range quantum Ising chain is a quench dynamics in which the transverse magnetic field is suddenly set to zero $h \rightarrow 0$. Then we consider the evolution of the transverse magnetization

$$m_z(t) = \langle \hat{S}_z(t) \rangle = \frac{1}{N} \sum_{j=1}^N \langle \hat{\sigma}_j^z(t) \rangle, \quad (1.34)$$

where $\langle \hat{\sigma}_j^z(t) \rangle = \langle \psi(0) | e^{-iH_{h=0}t} \hat{\sigma}_j^z e^{iH_{h=0}t} | \psi(0) \rangle$. Then assuming that the initial state is diagonal in the $\hat{\sigma}_j^z$ tensor product eigenbasis we find [95]

$$m_z(t) = m_z(0) \prod_{r=1}^N \cos^2(J_r t) = m_z(0) \prod_{r=1}^N \cos^2\left(\frac{Jt}{N_\alpha r^\alpha}\right), \quad (1.35)$$

where $m_z(0) = \sum_{j=1}^N \langle \psi(0) | \hat{\sigma}_j^z | \psi(0) \rangle / N$. The above expression describes a relaxation from the initial value $m_z(0)$ to its equilibrium value $\lim_{t \rightarrow \infty} m_z(t) = 0$. The time scale for such relaxation in the thermodynamic limit can be estimated by using the following inequality [95]

$$\lim_{N \rightarrow \infty} |m_z(t)| \leq |m_z(0)| e^{-cN_\alpha t^2}. \quad (1.36)$$

where c is a positive constant. As long as $\alpha > 1$ the large- N limit of the normalization N_α is finite and strictly positive (see Eq.(1.5)), proving a stretched exponential approach of m_z to its equilibrium value (see Fig. 1.2 (a)).

On the other hand, in the strong long-range regime $0 < \alpha < 1$, because of the divergence of the factor N_α in the large N limit (see Eq.(1.5)), it can be shown that the timescale on which the relaxation happens diverges with N , so that in the thermodynamic limit the system is trapped in a quasi-stationary state (see Fig. 1.2(b) and Ref. [95]).

In general to handle the finite time case, we need to generalize the Holstein–Primakoff approach introduced in Section 1.4.1, to the non-equilibrium context [92]. When the system is driven out of equilibrium, the direction of the collective spin configuration (parametrized by the polar coordinates $\theta(t)$ and $\phi(t)$) moves along the corresponding classical trajectory on the unit sphere. We thus let the adapted frame of reference $(\hat{\Sigma}_x(t), \hat{\Sigma}_y(t), \hat{\Sigma}_z(t))$ in Eq.(1.23) vary in time, in such a way that the new z-axis follows the instantaneous direction of the collective spin $\langle \hat{\mathbf{S}}(t) \rangle$ [92]. This is achieved through a time-dependent rotation generated by

$$V(t) = e^{-i\phi(t)S^z} e^{-i\theta(t)S^y}. \quad (1.37)$$

The spin components in this time-dependent frame are governed by the inertial Hamiltonian

$$\tilde{H}(t) = VH(t)V^\dagger + iVV^\dagger. \quad (1.38)$$

Holstein–Primakoff transformations are then applied to the individual rotating spins. The resulting transformed Hamiltonian can be organized as

$$\tilde{H}(t) = H_0(t) + H_1(t) + H_2(t) \dots \quad (1.39)$$

The leading-order term in the $N \rightarrow \infty$ limit, $H_0(t)$, describes the classical motion of the global spin $\langle \mathbf{S}(t) \rangle$. The $H_1(t)$ Hamiltonian describes a single harmonic mode corresponding to the $k = 0$ leading spin-wave excitation. Finally, the dynamics of finite α corrections is described, at quadratic order, by the $H_2(t)$ Hamiltonian.

1.5 The Kitaev chain with long-range interactions

Another approach for approximating the Hamiltonian in Eq. (1.19) involves using a truncated Jordan–Wigner transformation. Specifically, we apply the standard Jordan–Wigner mapping of spin variables onto fermionic ones as follows

$$\hat{\sigma}_j^z = 1 - 2\hat{c}_j^\dagger \hat{c}_j, \quad (1.40a)$$

$$\hat{\sigma}_i^x = - \left[\prod_{m=1}^{j-1} (1 - 2\hat{c}_m^\dagger \hat{c}_m) \right] (\hat{c}_j + \hat{c}_j^\dagger), \quad (1.40b)$$

$$\hat{\sigma}_i^y = -i \left[\prod_{m=1}^{j-1} (1 - 2\hat{c}_m^\dagger \hat{c}_m) \right] (\hat{c}_j - \hat{c}_j^\dagger), \quad (1.40c)$$

where \hat{c}_j^\dagger and \hat{c}_j are the fermionic creation and annihilation operators at site j , satisfying the canonical anticommutation relations $\{\hat{c}_l, \hat{c}_j\} = 0$ and $\{\hat{c}_l, \hat{c}_j^\dagger\} = \delta_{l,j}$. Applying this transformation to the Hamiltonian of the long-range quantum Ising chain yields its fermionic form

$$\begin{aligned} \hat{H} = & - \sum_{j=1}^N \sum_{r=1}^{N/2} J_r \left(\hat{c}_j^\dagger - \hat{c}_j \right) \left[\prod_{l=j+1}^{j+r-1} \left(1 - 2\hat{c}_l^\dagger \hat{c}_l \right) \right] \left(\hat{c}_{j+r}^\dagger + \hat{c}_{j+r} \right) \\ & - h \sum_{j=1}^N \left(1 - 2\hat{c}_j^\dagger \hat{c}_j \right). \end{aligned} \quad (1.41)$$

This Hamiltonian is not exactly solvable due to the presence of higher-than-quadratic terms in the fermionic operators. Therefore, we employ the approximation

$$\prod_{l=j+1}^{j+r-1} \left(1 - 2\hat{c}_l^\dagger \hat{c}_l \right) = 1, \quad (1.42)$$

for every $r \geq 2$, neglecting the string operators in the first line of Eq. (1.41). This truncated Jordan-Wigner transformation leads to the quadratic Hamiltonian

$$\begin{aligned} \hat{H}_{\text{LRK}} = & - \sum_{j=1}^N \sum_{r=1}^{N/2-1} \left[t_r \hat{c}_{j+r}^\dagger \hat{c}_j + \Delta_r \hat{c}_{j+r}^\dagger \hat{c}_j^\dagger + h.c. \right] \\ & - h \sum_{j=1}^N \left[1 - 2\hat{c}_j^\dagger \hat{c}_j \right], \end{aligned} \quad (1.43)$$

which we refer to as the long-range Kitaev chain [96, 97, 98]. More generally, we can allow the hopping and pairing amplitudes t_r and Δ_r to have different dependencies on the intersite distance r . Specifically, we choose the generic power law behaviors

$$t_r = \frac{1}{N^{\alpha_1}} \frac{J}{r^{\alpha_1}}, \quad \Delta_r = \frac{1}{N^{\alpha_2}} \frac{\Delta}{r^{\alpha_2}}, \quad (1.44)$$

with the hopping exponent $\alpha_1 > 0$, the pairing exponent $\alpha_2 > 0$, and the Kac normalization factor $N_\alpha = \sum_{r=1}^{N/2} r^{-\alpha}$. The integrable nature of this model makes it amenable to both analytical and numerical treatment.

1.5.1 Equilibrium properties

The quadratic nature of the Hamiltonian (1.43) allows its exact diagonalization in Fourier space via the Bogolyubov transformation

$$\hat{c}_k = \cos \frac{\phi_k}{2} \hat{\gamma}_k + \sin \frac{\phi_k}{2} \hat{\gamma}_{-k}^\dagger. \quad (1.45)$$

Here, \hat{c}_k represents the momentum space fermionic operators defined as

$$\hat{c}_k = \frac{e^{-i\frac{\pi}{4}}}{\sqrt{N}} \sum_{j=1}^N e^{ikj} \hat{c}_j, \quad (1.46)$$

where $k = 2\pi n/N$ and n is an integer such that $n = -N/2 + 1, \dots, N/2$. The Bogoliubov angles ϕ_k are defined by the conditions

$$\tan \phi_k = \tilde{\Delta}_k / (h - \tilde{t}_k) \quad (1.47)$$

with the Fourier transforms of the hopping and pairing amplitudes given by

$$\tilde{t}_k = \frac{J}{N\alpha_1} \sum_{r=1}^{N/2-1} \frac{\cos(kr)}{r^{\alpha_1}}, \quad \tilde{\Delta}_k = \frac{\Delta}{N\alpha_2} \sum_{r=1}^{N/2-1} \frac{\cos(kr)}{r^{\alpha_2}}. \quad (1.48)$$

Hereafter, we set $J = \Delta = 1$ as the energy scale and work in units of $\hbar = 1$. In terms of the Bogoliubov fermions, the Hamiltonian then takes the diagonal form

$$\hat{H}_{\text{LRK}} = \sum_k \omega_k(h) \left(\hat{\gamma}_k^\dagger \hat{\gamma}_k - 1/2 \right), \quad (1.49)$$

with the quasiparticle spectrum

$$\omega_k(h) = 2\sqrt{(h - \tilde{t}_k)^2 + \tilde{\Delta}_k^2}. \quad (1.50)$$

Since $\omega_k(h) \geq 0$, the ground state corresponds to the Fock space vacuum for the Bogoliubov modes, defined by the condition $\hat{\gamma}_k|\text{gs}\rangle = 0, \forall k$. Moreover, the properties of the single particle spectrum in Eq. (1.50) crucially depend on the values of α_1 and α_2 .

As shown in Section 1.2.2, in the weak long-range case, $\alpha_1, \alpha_2 > 1$, when the system size goes to infinity, we can safely perform a continuum limit in the k variable. In particular, Eq. (1.48) may be written as

$$\tilde{t}_k = \text{Re} \left[\text{Li}_{\alpha_1}(e^{ik}) \right] / \zeta(\alpha_1), \quad \tilde{\Delta}_k = \text{Im} \left[\text{Li}_{\alpha_2}(e^{ik}) \right] / \zeta(\alpha_2), \quad (1.51)$$

where $\text{Li}_\alpha(z)$ denotes the polylogarithm function. This leads to a continuum spectrum ω_k characterized, at the critical points, by a dispersion relation that depends on α_1 and α_2 . In particular, for $\alpha_1, \alpha_2 > 1$, the system possesses two different phases separated by two quantum critical points $h_c = 1, -1 + 2^{1-\alpha_1}$, in correspondence of which the dispersion relation becomes gapless near the critical mode $k_c = 0, \pi$, respectively [99, 16]. The critical modes of the spectrum are shown in Fig. 1.3(a) where $\omega_{0(\pi)}$ (blue (red) lines in the plot) is plotted as a function of h for different values of $\alpha_1 = \alpha_2$. The nature of the transition is

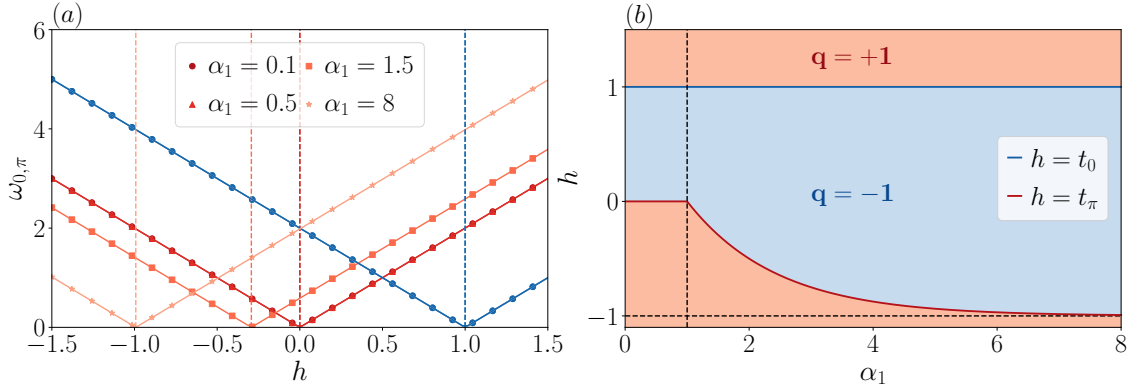


Figure 1.3: (a) Critical modes $k = 0, \pi$ of the quasiparticle spectrum as a function of the chemical potential h for different values of $\alpha_1 = \alpha_2$, two critical points emerge at $h = \tilde{t}_0, \tilde{t}_\pi$ where, in the thermodynamic limit, $\tilde{t}_0 = 1 \forall \alpha_1$, while $\tilde{t}_\pi = -1 + 2^{1-\alpha_1}$ if $\alpha_1 > 1$, and $\tilde{t}_\pi = 0$ if $0 < \alpha_1 < 1$. (b) Phase diagram of the long-range Kitaev chain in the plane (α_1, h) , for the pairing decay exponent $\alpha_2 = \alpha_1$, α_1 is the hopping decay exponent and h is the chemical potential. The topological order parameter is $q = -1$ in the topological phase (blue shaded region) and $q = +1$ in the trivial phase (red shaded region). The phase space boundaries correspond to the solid lines $h = \tilde{t}_0$ and $h = \tilde{t}_\pi$.

topological and the two topological phases can be distinguished by the value of the bulk topological invariant [100]

$$w = \oint \frac{d\phi_k}{2\pi} = \begin{cases} 1 & \text{if } h \in [-1 + 2^{1-\alpha_1}, 1] \\ 0 & \text{otherwise} \end{cases}. \quad (1.52)$$

Moreover, in the nontrivial phase with $w = 1$, the ground state is doubly degenerate, and can support Majorana edge modes [101].

In the strong long-range regime $0 < \alpha_1, \alpha_2 < 1$ the scenario is more involved. Indeed, as shown in Section 1.2.2, in this case, the hopping and pairing amplitudes $\tilde{t}_k, \tilde{\Delta}_k$, remain discrete also in the thermodynamic limit and they are labeled by the integer n , reading

$$\lim_{N \rightarrow \infty} \tilde{t}_k = c_{\alpha_1} \int_0^{1/2} ds \frac{\cos(2\pi ns)}{s^{\alpha_1}} = \tilde{t}_n, \quad (1.53)$$

$$\lim_{N \rightarrow \infty} \tilde{\Delta}_k = c_{\alpha_2} \int_0^{1/2} ds \frac{\sin(2\pi ns)}{s^{\alpha_2}} = \tilde{\Delta}_n, \quad (1.54)$$

with $c_\alpha = (1 - \alpha)2^{1-\alpha}$. Therefore, the presence of long-range couplings leads to a discrete spectrum $\omega_k \rightarrow \omega_n = 2\sqrt{(h - \tilde{t}_n)^2 + \tilde{\Delta}_n^2}$ also at $N \rightarrow \infty$. The persistence of the discrete

spectrum in the thermodynamic limit does not allow us to define a continuous theory and hinders the conventional definition of quantum critical points in the Kitaev chain. In particular, the winding number in Eq. (1.52) is ill-defined as a consequence of the discontinuity in the Bogolyubov angle distribution [100]. Yet, the transition can still be characterized by the quantity

$$q = \text{sign}[(h - \tilde{t}_0)(h - \tilde{t}_\pi)] = \begin{cases} 1 & \text{if } h \in [\tilde{t}_\pi, \tilde{t}_0] \\ -1 & \text{otherwise} \end{cases}. \quad (1.55)$$

This quantity has proven to be a good topological invariant in cases in which the winding number turns out to be ill-defined [100, 102]. Then, also in the strong long-range regime, the behavior of the order parameter q is still consistent with a change of phase at the critical points $h = \tilde{t}_0, \tilde{t}_\pi$ [103]. However, as shown in [104], the bulk boundary correspondence turns out to be weakened by the presence of strong long-range couplings. Consequently, the change of q at the critical points is not guaranteed to be in one-to-one correspondence with the appearance of boundary topological edge states. Nevertheless, we expect bulk properties to remain consistent with a change of phase. Figure 1.3(b) shows the model phase diagram as characterized by the value of $q = \pm 1$ as a function of the chemical potential h and of the hopping power law decay exponent α_1 . Two quantum critical lines appear when varying the α_1 parameter. In particular, we notice that the location of the critical point corresponding to $\omega_0 = 0$ is fixed to $h = \tilde{t}_0 = 1$ for any value of α_1 (blue bold line in Fig. 1.3(b)). On the contrary, the critical point corresponding to $\omega_\pi = 0$ (red bold line in Fig. 1.3(b)) is α_1 dependent with two different behaviors in the weak and strong long-range regimes, in particular in the thermodynamic limit we find

$$\lim_{N \rightarrow \infty} \tilde{t}_\pi = \begin{cases} -1 + 2^{1-\alpha_1} & \text{if } \alpha_1 \geq 1 \\ 0 & \text{if } 0 < \alpha_1 < 1 \end{cases}. \quad (1.56)$$

Finally, the mean-field case with $\alpha_1 = \alpha_2 = 0$ needs to be treated separately. Indeed, in this case, the spectrum becomes strongly degenerate and this may alter the nature of the ground state. In particular, for completely flat couplings the sums in Eq. (1.48) can be exactly computed and, in the thermodynamic, they read

$$\tilde{t}_n(\alpha_1 = 0) = \delta_{n,0}, \quad \tilde{\Delta}_n(\alpha_2 = 0) = \frac{1 + (-1)^{n+1}}{\pi n}. \quad (1.57)$$

Accordingly, the single-particle spectrum becomes

$$\omega_n^0 = \begin{cases} 2|h| & \text{if } |n| \text{ even} \\ 2\sqrt{h^2 + 4/(\pi n)^2} & \text{if } |n| \text{ odd} \\ 2|h - 1| & \text{if } n = 0 \end{cases}, \quad (1.58)$$

where we have introduced the shortcut notation $\omega_n^0 = \omega_n(\alpha_1 = 0, \alpha_2 = 0)$. It follows that an extensive number of single-particle energy levels corresponding to all the even modes become degenerate. In particular, when the chemical potential is zero $h = 0$ all the even modes become zero modes since at this point we have $\omega_{2n}^0(h = 0) = 0$, $\omega_{2n+1}^0(h = 0) = 2/|\pi n|$ and $\omega_0^0(h = 0) = 1$. This fact deeply affects the nature of the many-body ground state which is no more given by the Bogoliubov vacuum, on the contrary, it allows for a finite population of Bogoliubov fermions in an extensive number of zero modes. More precisely, the ground state for $\alpha_{1,2} = 0$ and $h = 0$ is given by a generic superposition of the form

$$|\text{gs}\rangle_{\alpha=0,h=0} = \sum_{n_0=0}^{N_0} C_{n_0} |n_0\rangle, \quad (1.59)$$

where n_0 is the number of fermions occupying the N_0 available zero modes. This ground state is highly degenerate indeed each $|n_0\rangle$ state can be realized in $\binom{N_0}{n_0}$ ways, leading to the exponential degeneracy

$$\text{Deg}[|\text{gs}\rangle_{\alpha=0,h=0}] = \sum_{n_0=0}^{N_0} \binom{N_0}{n_0} = 2^{N_0}. \quad (1.60)$$

As a concluding remark for this section, we stress the importance of the Kac scaling in the stabilization of the topological order in the strong long-range regime. Indeed, had we considered not properly rescaled couplings, the presence of long-range hopping $\alpha_1 < 1$ would have moved the critical point to $h_c = \mathcal{O}(N^{1-\alpha_1}) \rightarrow \infty$, thus destroying the transition.

1.5.2 Dynamical properties

In general, the unitary evolution generated by $\hat{H}_{\text{LRK}}(h(t))$ is such that it only mixes the states $|0_k, 0_{-k}\rangle$ and $|1_k, 1_{-k}\rangle$, where $|1_k\rangle = \hat{c}_k^\dagger |0_k\rangle$, for each value of k . Consequently, the dynamics of the Kitaev chain can be exactly described by N independent evolution equations, each restricted to the two-dimensional subspace associated with the corresponding k -mode [105]. These can be cast into a matrix evolution for the Bogoliubov coefficients u_k, v_k :

$$i \frac{d}{dt} \begin{pmatrix} u_k \\ v_k \end{pmatrix} = \mathcal{H}_k(t) \begin{pmatrix} u_k \\ v_k \end{pmatrix}, \quad (1.61)$$

with $\mathcal{H}_k = (h(t) - t_k)\sigma_k^z + \Delta_k \sigma_k^x$, where $\sigma_k^{(a)}$, $a = x, y, z$ are the sigma Pauli operators.

As a first example, we consider a sudden quench dynamics in which h abruptly changes from $h_i \gg 1$ to $h_f < 1$ in a long-range Kitaev chain with $\alpha = \alpha_1 = \alpha_2$. In this case Eq. (1.61) can be solved analytically leading to

$$\begin{pmatrix} u_k(t) \\ v_k(t) \end{pmatrix} = \begin{pmatrix} \cos(\omega_k t) - i \cos(\phi_k) \sin(\omega_k t) & i \sin(\phi_k) \sin(\omega_k t) \\ i \sin(\phi_k) \sin(\omega_k t) & \cos(\omega_k t) + i \cos(\phi_k) \sin(\omega_k t) \end{pmatrix} \begin{pmatrix} u_k(0) \\ v_k(0) \end{pmatrix} \quad (1.62)$$

where the ϕ_k are the Bogoliubov angles diagonalizing the final Hamiltonian.

As for the case of the quantum Ising chain, we study the dynamics of the transverse magnetization, which is related to the density of fermionic excitations produced during the dynamics as

$$m_z = 1 - \frac{2}{N} \sum_{j=1}^N \langle \hat{c}_j^\dagger \hat{c}_j \rangle. \quad (1.63)$$

As long as $\alpha > 1$, the time evolution of m_z is consistent with the expectations for an integrable system. At $t = 0$ the observable has its initial value and, then, rapidly equilibrates to a different constant expectation, which is maintained along the entire dynamics apart from a few rapid time fluctuations appearing at the Poincaré recurrence times. The fluctuations become increasingly more uncommon as the system approaches the thermodynamic limit, in agreement with the expected divergence of the recurrence times (See Fig. 1.4 (a) and (b)).

The picture is radically altered in the $\alpha < 1$ case (See Fig. 1.4 (c) and (d)). At intermediate system sizes the qualitative features remain similar to the $\alpha > 1$ case, with the transverse magnetization rapidly moving from its initial value $m_z(0) \approx 1$ to a different long-time expectation, around which it steadily oscillates. However, as the system size is increased the discrepancy with the traditional case is noticed. At larger N the large-time magnetization value tends to steadily grow, approaching the initial value $m_z = 1$. Moreover, the timescales of the oscillatory fluctuations are not altered by the increase in the system size, but rather manifest at almost equal time intervals at all sizes, consistent with the existence of finite recurrence times in the long-range systems at $\alpha < d$. These observations are consistent with the presence of quasi stationary states in the long-range Kitaev chain and are analogous to the picture obtained in the long-range Ising Hamiltonian in Section 1.4.2.

Another example in which the system dynamics is analytically solvable is the case of a linear driving of the form $h(t) = 1 - vt$. In this case Eq. (1.61) can be mapped onto a Landau-Zener-Stückelberg-Majorana (LZSM) problem [106, 107, 108, 109, 105] by means of the transformation $t' = \Delta_k(t_k - h + vt)/v$, leading to

$$i \frac{d}{dt'} \begin{pmatrix} u_k \\ v_k \end{pmatrix} = \begin{pmatrix} -\Omega_k t' & 1 \\ 1 & \Omega_k t' \end{pmatrix} \begin{pmatrix} u_k \\ v_k \end{pmatrix}, \quad (1.64)$$

where $\Omega_k = \delta/\Delta_k^2$. The exact general solution of Eq. (1.64) can be written in terms of Weber (or parabolic cylinder) D-functions $D_\nu(z)$, (see Ref. [105]), leading to

$$v_k(t') = a D_{-s-1}(-iz) + b D_{-s-1}(iz), \quad (1.65)$$

$$u_k(t') = \left(\Omega_k t' - 2i \frac{\partial}{\partial t'} \right) v_k(t'), \quad (1.66)$$

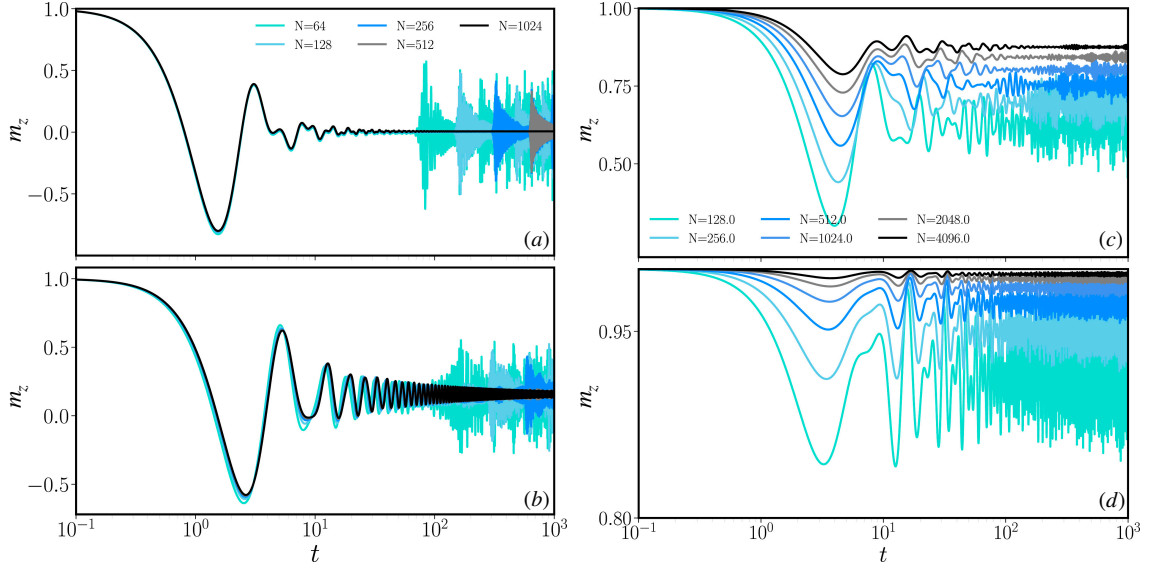


Figure 1.4: Transverse magnetization $m_z(t)$ after a quench in the long-range Kitaev chain with $h_i > 1$ and $h_f < 1$, for different values of α and of the system size N . (a) $\alpha \gg 3$, (b) $\alpha = 1.75$, (c) $\alpha = 0.9$, (d) $\alpha = 0.4$. Figure adapted from Ref. [103].

with $s = (4i\Omega_k)^{-1}$, $z = \sqrt{\Omega_k}t'e^{i\pi/4}$, and a, b arbitrary complex parameters to be fixed by the initial conditions $u_k(t_i)$, $v_k(t_i)$. Accordingly, the solution of Eq. (1.61) reads

$$|\psi(t)\rangle = \prod_k |\psi_k(t)\rangle, \quad (1.67)$$

$$|\psi_k(t)\rangle = u_k(t)|0_k, 0_{-k}\rangle + v_k(t)|1_k, 1_{-k}\rangle, \quad (1.68)$$

where $u_k(t) = u_k(t'(t))$, $v_k(t) = v_k(t'(t))$.

We can introduce the instantaneous eigenstates of the two-level Hamiltonians $\mathcal{H}_k(t)$ at time t , given by

$$|\phi_k^\pm(t)\rangle = \bar{u}_k(h(t))|0_k, 0_{-k}\rangle \pm \bar{v}_k(h(t))|1_k, 1_{-k}\rangle, \quad (1.69)$$

with $\bar{u}_k(h) = \cos(\phi_k(h)/2)$, $\bar{v}_k(h) = \sin(\phi_k(h)/2)$, where $\phi_k(h) = \arctan(\Delta_k/(h - t_k))$ is the Bogoliubov angle for a chemical potential $h = h(t)$. The non-adiabatic transition probabilities then read

$$\begin{aligned} p_k(t) &= 1 - |\langle \phi_k^\pm(t) | \psi_k(t) \rangle|^2 \\ &= 1 - |\bar{u}_k(h(t))u_k(t) + \bar{v}_k(h(t))v_k(t)|^2. \end{aligned} \quad (1.70)$$

By inserting the expression for u_k , v_k in Eqs. (1.65), (1.66), in the above expression, one obtains an analytical expression for $p_k(t)$ [110]. This exact solution, however, is rather

cumbersome. Considering the limit of a slow driving protocol $v \rightarrow 0$, with final time $\tau = |h_f - h_i|/v \rightarrow \infty$ allows for a simpler description that captures and better grasp the relevant physics involved in the dynamics. In this regime, the first non-trivial correction to p_k takes the celebrated LZSM form

$$p_k \simeq \exp\left(-\frac{\pi\Delta_k^2}{v}\right) + \mathcal{O}(v^2). \quad (1.71)$$

See Ref. [111] for its derivation using adiabatic perturbation theory. Although for finite Δ_k the $\mathcal{O}(v^2)$ contributions is leading, as the transition point is crossed, the physics is dominated by the soft modes with small Δ_k . As a consequence, in any relevant thermodynamic quantity, the $\mathcal{O}(v^2)$ contribution in the r.h.s. of (1.71) is negligible with respect to the non-analytic exponential one.

Chapter 2

The effective dimension approach

Before delving into the potential advantages of incorporating long-range interacting systems in quantum technological setups, we first review some methodological aspects that will be useful in exploring the universal properties of these systems throughout the thesis. Specifically, we examine the effective dimension approach (already introduced in Section 1.2.3 of the introduction), which connects the scaling exponents of a critical system in d spatial dimensions with power-law decaying interactions $J(r) \propto r^{-\alpha}$ to those of a local system with finite-range interactions in an effective fractal dimension d_{eff} . This method simplifies the study of long-range models by leveraging known results from their local counterparts.

Although the validity of this approximation beyond the mean-field level has been debated, in this Chapter we demonstrate that the effective dimension approach, while approximate for non-Gaussian fixed points, accurately estimates the critical exponents of long-range models with an accuracy typically exceeding 97%. This result validates the application of this method in the following chapters and enables a concise overview of the primary techniques used to investigate the critical properties of long-range systems.

To this end, we review perturbative renormalization group (RG) results, extend the validity of the approximation using functional RG techniques, and compare our findings with precise numerical data from conformal bootstrap for the two-dimensional Ising model with long-range interactions.

2.1 Effective dimension and scaling theory

We begin our analysis by showing how the effective dimension relation in Eq.(1.18) can be obtained using scaling theory. Our prototypical model belongs to the family of classical

$O(N)$ -symmetric spin models, characterized by the Hamiltonian

$$H = -\frac{1}{2} \sum_{i \neq j} J_{i,j} \mathbf{S}_i \cdot \mathbf{S}_j, \quad (2.1)$$

where \mathbf{S}_i is an N -component spin vector with unit modulus, $J_{i,j} > 0$ are ferromagnetic translational invariant couplings, and the indices i and j run over all the sites of any d -dimensional regular lattice of V sites. Specifically, we consider the case of power law decaying couplings $J_{i,j} = J/r_{i,j}^\alpha$, where $r_{i,j}$ is the distance between two sites. Since in this Chapter we will be dealing only with weak long-range systems with $\alpha > d$, it is convenient to rewrite the power-law exponent as $\alpha = d + \sigma$, with $\sigma > 0$.

From a field-theoretic perspective, the Hamiltonian in Eq. (2.1) lies in the same universality class as the continuous action

$$S = \int \frac{d^d k}{(2\pi)^d} \omega(k) |\varphi(k)|^2 + u \int d^d x |\varphi(x)|^4, \quad (2.2)$$

where the dispersion relation encodes only the low-energy momentum contribution $\omega(k) = a_\sigma k^\sigma + a_2 k^2 + r$ and φ is an N -component bosonic field [112]. At a Gaussian level ($u = 0$), long-range interactions become relevant for $\sigma < 2$, so that, at this level, the threshold of σ above which the universal properties are the one of the local model is $\sigma^* = 2$. The corresponding length dimension of the bosonic field is given by

$$[\varphi] \sim \begin{cases} L^{-(d-\sigma)/2} & \text{for } \sigma < 2 \\ L^{-(d-2)/2} & \text{for } \sigma > 2 \end{cases}. \quad (2.3)$$

Accordingly, at criticality, for $\sigma < 2$, we find

$$\langle \varphi(x) \varphi(0) \rangle \sim \frac{1}{x^{d-\sigma}} = \frac{1}{x^{d-2+\eta_{\text{LR}}}}, \quad (2.4)$$

where $\eta_{\text{LR}} = 2 - \sigma$ is the anomalous dimension computed with respect to the canonical dimension of the local theory. Thus, it quantifies the deviation in the decay of correlations from those in a local system.

Let us now introduce interactions into our framework as a perturbation to the Gaussian theory. Considering the quartic term in the action (2.2), we have $[\varphi^4] \sim L^{-2(d-\sigma)}$ for $\sigma < 2$, so that the perturbation is irrelevant as long as $\sigma < d/2$. Consequently, in this regime, mean-field results are exact, and for $O(N)$ models the threshold below which the universality becomes the mean-field one is $\sigma_{\text{mf}} = d/2$.

To probe values of σ beyond the mean-field region, we can use perturbative RG around the $d = 4, \sigma = 2$ Gaussian fixed point, expanding in terms of $\varepsilon = d - 2\sigma$. This problem was addressed in the seminal papers by Fisher and Sak [112, 43]. A key finding from these studies is that the $\propto k^\sigma |\varphi(k)|^2$ term in the action (2.2) does not acquire anomalous scaling.

This can be intuitively understood, as the perturbative expansion can only generate integer powers of k^2 , leaving the non-analytic $\propto k^\sigma$ behavior unaffected.

As a consequence, even in the presence of interactions, the scaling dimension of the long-range kinetic term in the Hamiltonian is given by

$$\Delta_\sigma = 2\Delta_\varphi + \sigma. \quad (2.5)$$

However, when interactions are present, the actual scaling of the local theory reads

$$\Delta_\varphi = (d - 2 + \eta_{\text{SR}})/2, \quad (2.6)$$

leading to [112]

$$\Delta_\sigma = d + \eta_{\text{SR}} - \eta_{\text{LR}}. \quad (2.7)$$

Thus, the boundary between long-range and local behavior must be identified at the value σ^* such that $\eta_{\text{LR}}(\sigma) = \eta_{\text{SR}}$. By comparing the scaling behaviors of the two interacting theories, we can justify the effective dimension relation in Eq. (1.18).

To elucidate this, we follow the procedure introduced in Refs. [113, 46] and consider the general scaling form of the singular part of the free energy density for a long-range system in d dimensions and a local system in d_{eff} dimensions. Equating them, we get

$$\begin{aligned} f_s &= \frac{1}{V} \Phi_{\text{LR}}(V y_\tau^{\text{LR}}/d, V y_h^{\text{LR}}/d, V y_u^{\text{LR}}/d) \\ &= \frac{1}{V} \Phi_{\text{SR}}(V y_\tau^{\text{SR}}/d_{\text{eff}}, L y_h^{\text{SR}}/d_{\text{eff}}, V y_u^{\text{SR}}/d_{\text{eff}}), \end{aligned} \quad (2.8)$$

where V is the total number of spins, τ is the reduced temperature, h is the reduced magnetic field, and u is the coupling of the irrelevant operator that gives the leading corrections. The exponents y_τ , y_h , y_u are connected to the eigenvalues of the linearized form of the RG transformation around the critical fixed point. The connection between long-range and short-range exponents is thus

$$y^{\text{LR}}/d = y^{\text{SR}}/d_{\text{eff}}. \quad (2.9)$$

Combining this condition with the relations of the y s with the critical exponents, we obtain [46]

$$\begin{aligned} d\nu_{\text{LR}} &= d_{\text{eff}}\nu_{\text{SR}}, & \frac{2 - \eta_{\text{LR}}}{d} &= \frac{2 - \eta_{\text{SR}}}{d_{\text{eff}}} \\ \gamma_{\text{LR}} &= \gamma_{\text{SR}}, & \omega_{\text{LR}}/d &= \omega_{\text{SR}}/d_{\text{eff}}. \end{aligned} \quad (2.10)$$

Interestingly, the critical exponents describing the scaling of global quantities, such as γ , directly correspond within the two theories, while the finite-size scaling exponents, such as ν correspond once scaled via the effective dimension.

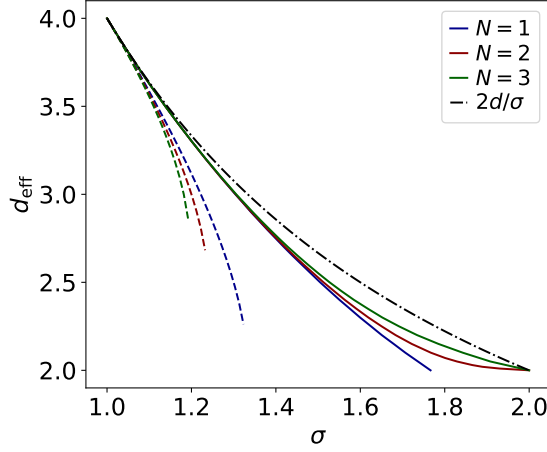


Figure 2.1: Effective dimension d_{eff} of the long-range $O(N)$ models with $N = 1$ (blue), $N = 2$ (red) and $N = 3$ (green), plotted as a function of the long-range power law exponent σ . The results are computed using functional RG (solid lines), perturbative RG (dashed lines), and at the mean field level (dot dashed line).

To derive Eq. (1.18), we assume that interactions do not shift the Gaussian estimate of the long-range anomalous dimension $\eta_{LR} = 2 - \sigma$. This assumption appears to be exact as it has been confirmed by perturbative arguments at $\mathcal{O}(\varepsilon^3)$ [43], functional RG studies [114, 115], Monte-Carlo [116, 117] and bootstrap calculations [118]. Combining this result with the relation between η_{LR} and η_{SR} in Eq. (2.10) leads to the dimensional identity in Eq. (1.18). Based on the same argument, one can derive the analytical expression for the threshold value σ_* , which coincides with the traditional result first obtained by perturbative RG [112], i.e., $\sigma_* = 2 - \eta_{SR}$.

2.2 Perturbative RG approach

Leveraging known perturbative Renormalization Group (RG) results, an explicit formula for d_{eff} can be derived, accurate up to corrections of order $\mathcal{O}(\varepsilon^3)$. Specifically, the epsilon expansion result from [119] for the η exponent of the local model in dimension d_{eff} is given by

$$\eta_{\text{SR}}^{d_{\text{eff}}} = \frac{N+2}{2(N+8)}(4-d_{\text{eff}})^2 + \mathcal{O}((4-d_{\text{eff}})^3). \quad (2.11)$$

By substituting this expression into Eq. (1.18), we can solve for the effective dimension d_{eff} , yielding two potential solutions. Then, to identify the physical solution for d_{eff} , we impose the correct mean-field threshold $\sigma = d/2$ at the upper critical dimension, i.e.,

$d_{\text{eff}}(\sigma = d/2) = 4$. This condition leads to the explicit expression

$$d_{\text{eff}} \approx 4 - \frac{1}{d} \frac{N+8}{N+2} \left[\sigma - \sqrt{\sigma^2 + \frac{(4d^2 - 8d\sigma)(N+2)}{(N+8)}} \right], \quad (2.12)$$

valid for N and σ values within the range

$$d/2 \leq \sigma \ll \frac{2d(4 + 2N - \sqrt{3N(N+2)})}{N+8}. \quad (2.13)$$

For larger σ values, the perturbative expression becomes invalid as Eq. (2.12) becomes complex, indicating the necessity to consider higher orders in the ε -expansion.

By calculating the critical exponents of the local model in the ε -expansion up to $\mathcal{O}(\varepsilon^3)$ and employing the relations with the long-range exponents in Eq. (2.10) and the expression for the effective dimension in Eq. (2.12), we can directly determine the long-range exponents as functions of σ and d , at the same level of approximation.

We observe that the ε -expansion results provide a good approximation only near $\sigma = d/2 = 1$, which is expected since in this region $d_{\text{eff}} \approx 4$. This is illustrated by the dashed lines Fig. 2.1. This also corresponds to the validity region of the $\mathcal{O}(\varepsilon^3)$ approximation determined by Eq. (2.13). Consequently, for these values of σ , the effective dimension approach provides a straightforward method to generalize ε -expansion results for the SR model to the long-range case.

Additionally, we note that for continuous theories with $N > 1$, the mean field results $d_{\text{eff}} = 2d/\sigma$ and $\nu_{LR} = d - \sigma$, which become exact in the $N \rightarrow \infty$ limit, perfectly interpolate between the known exact results in $d = 2$ and $d = 4$, see the red and green solid lines in Fig. 2.1. On the other hand, the Ising case $N = 1$ (blue solid line in Fig. 2.1) exhibits a peculiar behavior, reaching $d_{\text{eff}} = 2$ for $\sigma = \sigma^* = 7/4$. This distinct behavior is due to the discrete symmetry of the Ising model, which results in a finite anomalous dimension even in $d = 2$.

2.3 Functional RG approach

The Functional Renormalization Group (FRG) is a modern RG framework that allows for the derivation of an *in principle* exact equation for the flow of the effective action, Γ_k of the model under study. This framework, pioneered by the seminal works of Wilson [120] and Polchinski [121], is more conveniently expressed in terms of the Wetterich equation [122]

$$\partial_t \Gamma_k = \frac{1}{2} \text{Tr} \left[\frac{\partial_t R_k}{\Gamma^{(2)} + R_k} \right]. \quad (2.14)$$

where $t = \ln(k/k_0)$, $\Gamma^{(2)}$ is the second derivative of the effective action with respect to the order parameters, and $R_k(q)$ is a momentum space regulator function that cuts off

the infrared divergences caused by slow modes $q \ll k$, while leaving the high-momentum modes $q \gg k$ almost untouched.

To handle Eq. (2.14), one must project it onto a restricted functional space, parameterized by a finite number of functional operators. In this perspective, a convenient ansatz for the effective action of the long-range interacting $O(N)$ model is given by [114]

$$\Gamma_k[\varphi] = \int d^d x [Z_k \partial_\mu^{\frac{\sigma}{2}} \varphi_i \partial_\mu^{\frac{\sigma}{2}} \varphi_i + U(\rho)] \quad (2.15)$$

where φ_i is the i th component of φ , $\rho = \varphi_i \varphi_i / 2$ and the summation over repeated indexes is assumed. The notation $\partial_\mu^{\frac{\sigma}{2}}$ indicates that the inverse propagator of the effective action in Fourier space depends on q^σ . Then, introducing the dimensionless variables

$$\bar{U}_k(\bar{\rho}) = k^{-d} U_k(\rho), \quad \bar{\rho} = Z_k k^{d-\sigma} \rho, \quad \bar{q} = k^{-1} q, \quad (2.16)$$

and defining the generalized Litim cutoff [123] suitable for long-range interactions [114, 124, 33]

$$R_k(q) = Z_k (k^\sigma - q^\sigma) \theta(k^\sigma - q^\sigma), \quad (2.17)$$

we obtain the following flow equation for the effective potential

$$\begin{aligned} \partial_t \bar{U}_k &= -d \bar{U}_k(\bar{\rho}) + (d - \sigma + \delta\eta) \bar{\rho} \bar{U}'_k(\bar{\rho}) \\ &+ \frac{\sigma}{2} c_d (N - 1) \frac{d + \sigma - \delta\eta}{(d + \sigma)(1 + \bar{U}'_k(\bar{\rho}))} \\ &+ \frac{\sigma}{2} c_d (N - 1) \frac{d + \sigma - \delta\eta}{(d + \sigma)(1 + \bar{U}'_k(\bar{\rho} + 2\bar{\rho} \bar{U}''_k(\bar{\rho})))}, \end{aligned} \quad (2.18)$$

where $c_d^{-1} = (4\pi)^{d/2} \Gamma(d/2 + 1)$ and $\delta\eta = -\partial_t \ln Z_k$. Allowing the wavefunction renormalization Z_k to be a running but field-independent coupling, we find its flow equation to be

$$\partial_t Z_k = \lim_{p \rightarrow 0} \frac{d}{dp^\sigma} \partial_t \Gamma_k^{(2)}(p, -p). \quad (2.19)$$

However, since the flow equation generates no non-analytic terms in p , from its definition we find that $\delta\eta = 0$, in agreement with the previously presented Sak's picture [112]. Consequently, in Eq. (2.18), the $\delta\eta$ terms can be omitted.

Also in the functional RG framework, one can establish a mapping, between the long-range critical exponents in d dimensions and the equivalent local ones at the effective dimension d_{eff} . For the correlation length critical exponent ν , this correspondence is obtained by formulating an eigenvalue equation for the stability of perturbations around $\bar{U}_k = \bar{U}_k^*(\bar{\rho})$, the fixed point solution of Eq. (2.18). Then by making the substitution

$$\bar{U}_k(\bar{\rho}) = \bar{U}_k^*(\bar{\rho}) + k^y \bar{u}_k(\bar{\rho}), \quad (2.20)$$

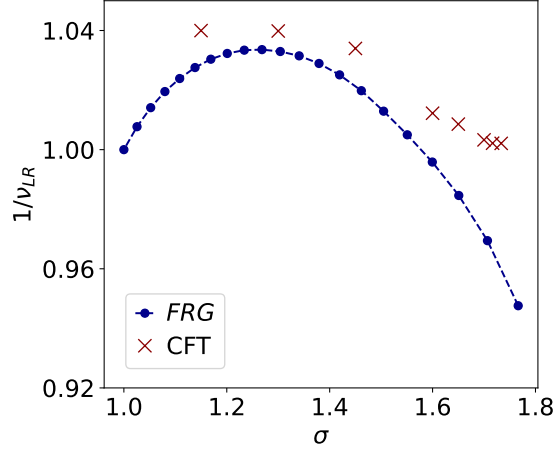


Figure 2.2: The correlation length exponent ν_{LR} of the long-range Ising model obtained via the functional RG approach within the LPA framework, see Eq. (2.18) is compared with accurate conformal bootstrap (CFT) result. The accuracy of functional RG in reproducing the CFT data lies within 92%.

one derives a functional equation for the stability matrix exponents y s of the RG flow, which are related to the correlation length critical exponent by the relation $\nu^{-1} = \min\{y\}$.

Next, comparing Eq. (2.18), and its stability matrix extension with their local counterparts in d_{eff} dimensions [125], and reabsorbing the constant c_d into the definition of the field [126], one reestablishes the dimensional equivalence as given in Eq. (1.18) [114]. This shows that the dimensional correspondence described by the relations in Eq. (2.10) can be derived outside the heuristic scaling theory framework of Sec. 2.1, suggesting it is a highly accurate approximation for the actual critical exponents of the long-range model.

The approximate nature of the effective dimension correspondence becomes evident when going beyond the ansatz in Eq. (2.15) and including a local kinetic term

$$\Gamma_k[\varphi] = \int d^d x [\partial_\mu^{\frac{\sigma}{2}} \varphi_i \partial_\mu^{\frac{\sigma}{2}} \varphi_i + Z_k \partial_\mu \varphi_i \partial_\mu \varphi_i + U(\rho)] \quad (2.21)$$

where the running wave-function renormalization for the non-analytic kinetic term is omitted as it has been shown to be irrelevant. The study of the ansatz (2.21), performed in Ref. [114], demonstrated that the resulting flow equations are not consistent with the effective dimension relations, unlike the simpler case of Eq. (2.18). However, the discrepancy between the numerical values obtained using the two ansatz in Eq. (2.15) and Eq. (2.21) is quite small, remaining well below 5% for all values of σ , reinforcing the expectation of the high accuracy of the effective dimension relation [114].

A first confirmation of this expectation comes from comparing the numerical estimate for ν_{LR} obtained through the study of Eq. (2.18) with the (possibly) exact results recently

obtained via conformal bootstrap [127], as shown in Fig. 2.2. The figure illustrates that despite the rather crude approximation defined by Eq. (2.15), the functional RG results (full blue circles) effectively capture the trend of the CFT data, with numerical error remaining within 7%. However, as will be argued in the next section, the effective dimension correspondence actually surpasses the functional RG accuracy when applied to exact numerical estimates.

2.4 Comparison with exact numerics

On the numerical side, the validation of the Sak's scenario and the effective dimension correspondence has sparked a long-standing debate. Early Monte Carlo (MC) studies, using algorithms specifically designed for long-range interactions [128], supported $\sigma_* = 2 - \eta_{\text{SR}}$ [116]. However, more recent MC results have challenged Sak's scenario [129], reporting $\sigma_* = 2$. Furthermore, MC studies of a percolation model with long-range probabilities [130] mirrored the findings of Ref. [129] and did not reproduce Sak's result, although they did not explicitly discuss it. Additionally, MC results for the Ising model with long-range interactions in $d = 2$ presented in Ref. [46] showed the presence of logarithmic corrections in the correlation function when σ is very close to the $\sigma_* = 2 - \eta_{\text{SR}}$ boundary. This implies numerical difficulty in extracting reliable results for the critical exponents with small error bars around $\sigma_* = 2 - \eta_{\text{SR}}$. While theoretical investigations now almost unanimously support Sak's picture [114, 118], a precise estimate of the accuracy of the effective dimension correspondence remains an open question.

Here, we assess this accuracy by comparing numerically exact estimates for the correlation length exponent of the Ising model. These comparisons are only possible for the Ising $N = 1$ case, where conformal bootstrap techniques have recently provided highly accurate estimates of the scaling dimensions in the long-range case [127]. While the study of the nearest-neighbour Ising model in generic fractional dimension has been already available for almost a decade [131].

These data are compared in Fig. 2.3, where the exponent $1/\nu_{\text{SR}}^{d_{\text{eff}}}$ (blue dots) is plotted as a function of d_{eff} and compared with the corresponding long-range exponent in two dimensions $1/\nu_{\text{LR}}^d$ (red crosses) appropriately rescaled according to Eq. (2.10). While the match between the curves is not perfect, confirming the approximate nature of the effective dimension paradigm, the accuracy of the effective dimension approach clearly surpasses the predictions from previous one-loop arguments. Indeed, as shown in the inset of Fig. 2.3, the ratio $d\nu_{\text{LR}}^d/d_{\text{eff}}\nu_{\text{SR}}^{d_{\text{eff}}}$ is always greater than approximately 0.97, indicating a 97% accuracy in the estimates for the long-range exponents obtained using the effective dimension correspondence, well beyond the accuracy of the functional RG argument used to derive the effective dimension relation in Sec. 2.3.

It is worth noting that the Ising model ($N = 1$) is expected to represent the worst-case scenario for the effective dimension prediction among the $O(N)$ models. Indeed, the cor-

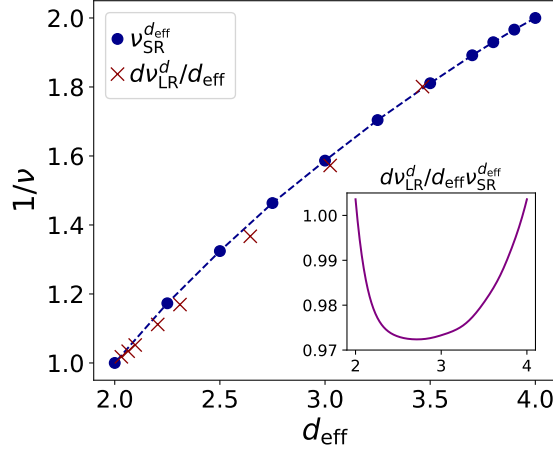


Figure 2.3: Comparison between the correlation length exponent of the local Ising model in d_{eff} dimension ($\nu_{\text{SR}}^{d_{\text{eff}}}$, blue dots) and that of the long-range Ising model in $d = 2$ dimensions, scaled by a factor d/d_{eff} ($d\nu_{\text{LR}}^d/d_{\text{eff}}$, red crosses), plotted as a function of the effective dimension $d_{\text{eff}}(\sigma)$. The numerical data have been obtained through conformal bootstrap methods as reported in Refs. [131] and [127], respectively. The inset shows the accuracy of the effective dimension prediction, estimated as the ratio $d\nu_{\text{LR}}^d/d_{\text{eff}}\nu_{\text{SR}}^{d_{\text{eff}}}$, plotted as a function of d_{eff} .

rections to the effective dimension relation arise due to high-order momentum corrections to the vertexes of $O(N)$ field theories, which are not parametrized by the ansatz (2.15). These same vertex corrections cause the emergence of a finite anomalous dimension in local theories. Thus, the larger the anomalous dimension of a local theory, the lower we estimate the accuracy of the effective dimension correspondence with its long-range counterpart. As the Ising model displays the largest anomalous dimension within $O(N)$ field theories, we expect the effective dimension correspondence to be more accurate as N increases.

2.5 Closing remarks

In summary, the study presented in this Chapter has thoroughly examined the critical behavior of long-range interacting systems using a combination of perturbative and functional renormalization group (RG) approaches. Our primary objective was to establish and validate the effective dimension framework, which correlates the critical properties of long-range models with those of local models in a suitably defined effective dimension d_{eff} .

We began by revisiting Sak's seminal results with perturbative RG techniques, confirming that the effective dimension approach holds at leading order in perturbation theory. This approach provides a robust approximation for the critical exponents of long-range

models, particularly accurate near the mean-field threshold $\sigma = d/2$, and remains valid up to $\mathcal{O}(\varepsilon^3)$ corrections. Our analysis demonstrated that the effective dimension d_{eff} and the corresponding critical exponents can be explicitly computed, offering an efficient method for estimating the critical properties of long-range systems.

Subsequently, we extended our investigation to functional RG methods, enabling a more comprehensive treatment beyond the limitations of perturbative expansions. By deriving flow equations for the effective potential and wavefunction renormalization, we showed that the effective dimension approach is consistent with functional RG results. This consistency underscores the reliability of the effective dimension as a predictive tool for long-range critical phenomena, even when interactions and fluctuations are considered more rigorously.

Finally, we compared the predictions of the effective dimension approach with exact numerical data obtained from conformal bootstrap methods for the two-dimensional Ising model with long-range interactions. The comparison indicated excellent agreement, with an accuracy greater than 97%.

In conclusion, our study provides strong evidence that the effective dimension approach, while approximate, offers an accurate and practical framework for estimating critical exponents in long-range interacting models. It effectively bridges the gap between perturbative RG predictions and exact numerical results, delivering a comprehensive understanding of the universal features of critical phenomena in systems with long-range interactions.

Chapter 3

Quantum Thermodynamics of long-range systems

3.1 Quantum thermodynamics

Thermodynamics originated in the nineteenth century from practical concerns, specifically the need to understand and optimize the operation of thermal machines such as heat engines and refrigerators. Since then, the performance of these devices has seen significant advancements to meet the demands of modern technology. These advancements span a wide range of applications, from fuel-based vehicles and household air conditioners to the most advanced dilution refrigerators used today [132]. The pursuit of fault-tolerant quantum computing represents the latest technological frontier, garnering considerable research attention in recent years [133]. In particular the route towards fault tolerance of available quantum processors is dictated by the quantum threshold theorem [134, 135, 136], which states that error correction is feasible even with noisy gates, provided the noise level remains below a critical threshold.

Cooling quantum hardware to sufficiently low temperatures theoretically enables achieving this threshold. However, the integration of large classical apparatuses, such as thermal baths, may introduce additional sources of decoherence. Therefore, the development of microscopic and coherent thermodynamic machines has emerged as a pressing technological challenge [137]. This challenge has driven research into quantum thermal engines, i.e., heat engines and refrigerators operating directly within the quantum domain [138]. Extensive theoretical [139, 140, 141, 142, 143, 144, 145, 146] and experimental [147, 148, 149, 150, 151, 152, 153, 154] studies have been conducted, recently demonstrating their potential applicability to existing quantum processors [12, 11, 155].

However, these devices are subject to a well-known trade-off between power and efficiency [146]. This trade-off arises from two main factors: the first being the fundamental constraints imposed by the second law of thermodynamics on irreversible processes, which

implies that the thermodynamic efficiency of a heat engine must be lower than that of a Carnot engine [156]. Additionally, any practical cycle operates over a finite time, introducing further losses due to dynamic excitations that dissipate energy, thereby degrading the device performance. As a result, increasing power typically leads to greater dissipation, adversely affecting efficiency. Various strategies have been proposed to mitigate non-adiabatic transitions, known as shortcuts to adiabaticity, to address this issue [157, 158, 159, 160]. However, these techniques often involve activating additional driving fields, which incurs an energetic cost that reduces the actual output of the device [161, 162].

In this section, we explore a novel approach to minimize these adverse effects by employing a long-range interacting quantum system as the working substance of the engine, determining the conditions under which the presence of long-range interactions reduces the energy losses due to defect generation during non-adiabatic evolution.

3.2 Quantum work statistics

A fundamental object in the study of thermodynamic efficiency is the statistics of work exchanged by a quantum system with an external driving during a non-adiabatic evolution.

The study of quantum work statistics delves into the dynamics of a quantum system governed by a Hamiltonian $H(h)$, which depends on an external work parameter h . The system starts in the initial state ρ_i and a driving protocol modifies the work parameter from h_i to h_f . Consequently, the initial and final Hamiltonians are

$$H_i = H(h_i) = \sum_n \epsilon_n^i |\epsilon_n^i\rangle\langle\epsilon_n^i|, \quad H_f = H(h_f) = \sum_m \epsilon_m^f |\epsilon_m^f\rangle\langle\epsilon_m^f|, \quad (3.1)$$

respectively. Under the influence of external driving, the system evolves unitarily, resulting in the final state $\rho_f = U\rho_i U^\dagger$ with

$$U = \text{T exp} \left[-i \int_0^\tau dt H(h_t) \right], \quad (3.2)$$

the unitary evolution operator, where T exp denotes the time-ordered exponential. Throughout this process, the system exchanges energy with the external drive, manifested as work W , which is a stochastic variable with a probability density given by [163, 164]

$$P(W) = \sum_{n,m} p_{n,m} \delta \left(W - (\epsilon_m^f - \epsilon_n^i) \right), \quad (3.3)$$

where $p_{n,m}$ represents the probabilities associated with all the possible energy differences between the energy levels of the initial and final Hamiltonians. For an initial state that is incoherent with respect to H_i , i.e., $[\rho_i, H_i] = 0$ [7], we have $p_{n,m} = p_n^i p_{n|m}$, where $p_n^i = \text{Tr}[\rho_i |\epsilon_n^i\rangle\langle\epsilon_n^i|]$ is the initial population of the n th energy level, and $p_{n|m} = |\langle\epsilon_n^i|U|\epsilon_m^f\rangle|^2$

denotes the transition probability between the n th and m th energy levels during the unitary evolution [164].

To analyze the probability $P(W)$ we may use its moment generating function

$$G(s) = \int dW e^{-sW} P(W) = \text{Tr} \left[U^\dagger e^{-sH_f} U e^{sH_i} \rho_i \right]. \quad (3.4)$$

From which all the moments of the distribution can be obtained by deriving with respect to the s variable.

Considering, for example, a linear driving protocol, $h(t) = h_i - vt$, over a time interval $t \in [0, \tau]$ and with a quench rate $v = (h_i - h_f)/\tau$. We can investigate the system's response to different quench velocities v . At this scope we focus on the statistics of irreversible work $W_{\text{irr}} = W - \Delta\epsilon_0$, where $\Delta\epsilon_0 = \epsilon_0^f - \epsilon_0^i$ represents the adiabatic work contribution, i.e., the difference between final and initial ground state energies. W_{irr} accounts for the energy irreversibly dissipated during the evolution due to the dynamic generation of defects in finite-time dynamics.

In the following we explore two opposite limits: the sudden quench scenario where $v \rightarrow \infty$ ($\tau \rightarrow 0$) and the slow quench case where $v \rightarrow 0$ ($\tau \rightarrow \infty$).

3.3 Universal quantum work statistics in long-range systems

In this section, we provide a comprehensive characterization of the universal properties of quantum work statistics in long-range interacting quantum systems subjected to various external drivings, ranging from a sudden quench to infinitely slow linear driving. We aim to determine the conditions under which long-range interactions reduce energy losses due to defect generation during non-adiabatic evolution. To achieve this in a general setup, we utilize the effective dimension approach, detailed and justified in Chapter 2, to analyze the universal behavior of systems with long-range interactions. Finally, we apply our findings to two concrete examples: the long-range quantum Ising chain and the long-range Kitaev chain.

3.3.1 The sudden quench case

In the sudden quench scenario, and assuming that the system is initially in the ground state, Eq. (3.4) simplifies to

$$G(s) = \langle \epsilon_0^i | e^{sH_i} e^{-sH_f} | \epsilon_0^i \rangle = e^{-\Delta\epsilon_0 s} Z(s) \quad (3.5)$$

where $Z(s) = \langle \epsilon_0^i | e^{-(H_f - \epsilon_0^f)} | \epsilon_0^i \rangle$. This expression can be interpreted as the partition function of a $d + 1$ -dimensional classical system on a film of thickness s , with two boundary states $|\epsilon_0^i\rangle$ and a transverse area L^d [165, 166]. This mapping is schematically illustrated in panels (a) and (b) of Fig. 3.1 Within this interpretation, the cumulant generating function $\mathcal{F} =$

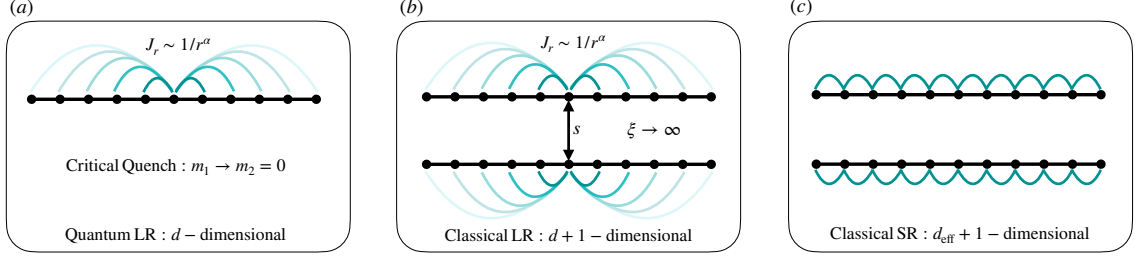


Figure 3.1: Schematic representation of the quantum-to-classical mapping for the quantum work statistics problem in long-range interacting systems. (a) The original quantum model in d dimensions with power-law decaying couplings, subjected to a sudden quench to the critical point—transitioning from a massive $m_1 > 0$ initial Hamiltonian to a massless final Hamiltonian $m_2 = 0$, where m_i denotes the mass of the lightest quasiparticle describing the system’s excitations. (b) The corresponding equilibrium long-range interacting classical system in $d + 1$ dimensions, obtained through the quantum-to-classical mapping. (c) The local classical system in equilibrium in $d_{\text{eff}} + 1$ dimensions, derived in the final step of our mapping using the effective dimension approach.

$-\ln G(s)$ represents the free energy per unit temperature of the corresponding classical system [165].

Then, as s , increases, the free energy density per unit area $f = \mathcal{F}/L^d$ decomposes into

$$f = s f_b + 2 f_s + f_c(s), \quad (3.6)$$

where $f_b = \Delta\epsilon_0/L^d$ and $f_s = -(\ln |\langle \epsilon_0^f | \epsilon_0^i \rangle|)/L^d$ can be interpreted as bulk and surface free energy densities in the corresponding classical system in a film geometry [165, 166]. The term $f_c(s)$ is a subleading contribution in the large s limit but is significant in critical quenches $h_f = h_c$ as it embodies the critical Casimir effect and exhibits the universal scaling form [167, 168, 169]:

$$f_c(s) \approx s^{-d} \Theta(s/\xi) \quad \text{for } s \gg a, \quad (3.7)$$

where $\xi \gg a$ denotes the correlation length and a represents a microscopic length scale. The scaling function $\Theta(x)$ is universal, depending solely on the universality class of the bulk classical critical point and the surface universality class [170].

Once the scaling behavior of the characteristic function is established, it reveals universal properties of the work distribution. In particular, we examine the intensive irreversible work $w = (W - \Delta\epsilon_0)/L^d$. Our focus lies on the probabilities of large deviation events, where w is significantly smaller than its mean value $\langle w \rangle$, indicating proximity to the adiabatic limit where $w = 0$. The probability of such large deviations is expected to decrease

exponentially with system size L^d , i.e.,

$$P(w) \propto e^{-I(w)L^d}, \quad (3.8)$$

where $I(w)$ is the non-negative rate function, vanishing at $w = \langle w \rangle$. The quadratic approximation of $I(w)$ around $w = \langle w \rangle$ reproduces typical Gaussian fluctuations $w - \langle w \rangle \sim 1/\sqrt{N}$ predicted by the central limit theorem [171, 172, 173].

Additionally, we observe that $P(w < 0) = 0$, implying $I(w < 0) = +\infty$, and assuming a bounded spectrum, $P(w > w_M) = 0$, where w_M represents the maximum work that can be introduced into the system, corresponding to a fully filled spectrum. As $L \rightarrow \infty$, the rate function is obtained through the Legendre-Fenchel transform [171]:

$$I(w) = - \inf_{s \in \mathbb{R}} \{sw - 2f_s - f_c(s)\}. \quad (3.9)$$

In particular, for a critical quench with $\xi \rightarrow \infty$, we obtain

$$I(w) \approx 2f_s - \frac{d+1}{d} \Theta(0) \left(\frac{w}{\Theta(0)} \right)^{d/(d+1)}. \quad (3.10)$$

Long-range interactions crucially influence the scaling above. Specifically, as detailed in Chapter 2, if we consider a quantum system in d dimensions whose Hamiltonian contains a power-law decaying coupling of the form $J(r) \propto 1/r^\alpha$, the universal properties of the system at criticality are well captured by considering the short-range version of the model in a fractal dimension d_{eff} , related to α and d by equation (1.18).

This mapping, schematically shown in Fig. 3.1, illustrates how the out-of-equilibrium work statistics problem in a quantum long-range system in d dimensions (panel (a)) can be mapped to a classical local problem at equilibrium in a film geometry in dimension $d_{\text{eff}} + 1$ (panel (c)).

Thus, the rate function for a long-range system is obtained by simply replacing d_{eff} in Eq.(3.10). Typically, $d_{\text{eff}} \geq d$ for any $d < \alpha < \alpha^*$, indicating that in the large deviation region, $I_{\text{SR}}(w) < I_{\text{LR}}$, meaning that the probability of having $w \ll \langle w \rangle$ is larger in the long-range case. This is a first indication that long-range interaction decrease the irreversible work performed by the system.

3.3.2 The slow quench case

In the slow quench scenario $v \rightarrow 0$, it is useful to express the logarithm of the characteristic function as a series expansion

$$\ln G(s) = \sum_{n=1}^{\infty} \frac{s^n}{n!} \kappa_n, \quad (3.11)$$

where κ_n is the n th cumulant of the work distribution. By analyzing how these cumulants scale with the small but finite driving velocity v , we can deduce the universal properties of the work distribution in this regime.

In particular, we consider a time-dependent Hamiltonian of the form $H(\lambda(t))$ which is slowly driven across a quantum critical point at $\lambda = 0$. Adopting the standard assumptions of adiabatic perturbation theory [174, 111], we consider the condition that at the critical point, the energy gap vanishes due to the dispersion relation of low-energy (small k) modes scaling as $\omega_k = c|k|^z$, where c is a non-zero constant. Additionally, we apply the approximation of a low density of quasiparticles excited after the quench in each mode, i.e., $n_k \lesssim 1$ for all k , where n_k denotes the occupation number of the k th mode at the end of the process. Under these conditions, the work performed during the process is given by

$$W = \Delta\epsilon_0 + \sum_k \omega_k n_k. \quad (3.12)$$

The probability of having n_k excitations in the k th mode is

$$p_{n_k=0} = 1 - p_k, \quad p_{n_k=1} \approx p_k, \quad p_{n_k>2} \approx 0. \quad (3.13)$$

Thus, the logarithm of the characteristic function reads [175, 176, 177]

$$\ln G(s) = s\Delta\epsilon_0 + \sum_k \ln[1 + p_k(e^{-s\omega_k} - 1)]. \quad (3.14)$$

Then, expanding $\ln G(s)$ in powers of s , the cumulants of work are

$$\kappa_n \approx \delta_{n,1}\Delta\epsilon_0 + \sum_k \omega_k^n p_k. \quad (3.15)$$

For small driving velocity $v \rightarrow 0$, the scaling of the work cumulants is determined by the low-energy modes. More precisely, within adiabatic perturbation theory, the excitation probability of the k th-mode quasiparticle p_k is dominated by (assuming that there is no additional Berry phase) [174, 111, 105]

$$p_k \approx \left| \int_{h_i}^{h_f} dh \langle 1_k(h) | \partial_h | 0_k(h) \rangle e^{\frac{i}{v} \int_{h_i}^h dh' \omega_k(h')} \right|^2 \quad (3.16)$$

where $|n_k(h)\rangle$ denotes the instantaneous energy eigenstate of mode k of $H(h)$ with occupation number n_k . In order to remove the quantity $1/v$ in the exponential function in the integral of p_k (Eq. (3.16)), we introduce two rescaled quantities, x and y , defined by

$$h = xv^{1/(1+\nu z)}, \quad k = yv^{\nu/(1+\nu z)}. \quad (3.17)$$

Also following Ref. [111, 105], we introduce the general scaling argument

$$\omega_k(h) = |h|^{\nu z} F(k/|h|^\nu), \quad (3.18)$$

$$\langle 1_k(h) | \partial_h | 0_k(h) \rangle = h^{-1} G(k/|h|^\nu), \quad (3.19)$$

where F and G are two model-dependent scaling functions satisfying $F(x) \propto x^z$ and $G(x) \propto x^{-1/\nu}$ for $|x| \gg 1$. This is motivated by dimensional considerations and the requirement that the spectrum of the high energy modes should be insensitive to h . Thus, assuming a critical quench with $\omega_k(h_f) \approx c|k|^z$, the work cumulants reads

$$\kappa_n \approx \Delta\epsilon_0 \delta_{n,1} + c^n v^{\theta_n} \int \frac{d^d y}{2\pi} |y|^{nz} f(y), \quad (3.20)$$

where

$$\theta_n = \frac{(d + nz)\nu}{1 + \nu z}, \quad (3.21)$$

and we have introduced the function

$$f(y) = \left| \int_{x_i}^{x_f} \frac{dx}{x} G(y/|x|^\nu) e^{i \int_{x_i}^x dx' |x'|^{\nu z} F(y/|x'|^\nu)} \right|^2. \quad (3.22)$$

Consequently, as long as $\theta_n < 2$, the scaling of the work cumulants is dominated by the low energy modes, $f(y)$ is convergent as $v \rightarrow 0$, and $\kappa_n - \Delta\epsilon_0 \delta_{n,1} \approx a_n v^{\theta_n}$. On the other hand, when $\theta_n > 2$ the integral is not dominated by the low energy modes and the leading term comes from the high-energy contribution, which can be approximated by the regular analytic adiabatic perturbation theory [174, 178, 111], resulting in the quadratic scaling $\kappa_n - \Delta\epsilon_0 \delta_{n,1} \approx a_n v^2$. Finally, when $\theta_n = 2$, logarithmic corrections are expected leading to the scaling $\kappa_n - \Delta\epsilon_0 \delta_{n,1} \approx a_n v^2 \ln v$. Summarizing we have that

$$\kappa_n - \Delta\epsilon_0 \delta_{n,1} \approx \begin{cases} a_n v^{\theta_n} & \theta_n < 2 \\ a_n v^2 \ln v & \theta_n = 2 \\ a_n v^2 & \theta_n > 2 \end{cases}. \quad (3.23)$$

Also in this case the universal scalings for a long-range interacting system are derived using the effective dimension approach. The scaling exponent becomes

$$\theta_{n,\alpha} = \frac{(d + n z_{\text{LR}}^d) \nu_{\text{LR}}^d}{1 + \nu_{\text{LR}}^d z_{\text{LR}}^d} \approx \frac{(d_{\text{eff}} + n z_{\text{SR}}^{d_{\text{eff}}}) \nu_{\text{SR}}^{d_{\text{eff}}}}{1 + \nu_{\text{SR}}^{d_{\text{eff}}} z_{\text{SR}}^{d_{\text{eff}}}}. \quad (3.24)$$

The approximate sign accounts for minor corrections due to the anomalous dimension in the frequency dependence of the low-energy propagator of the quantum long-range theory [1].

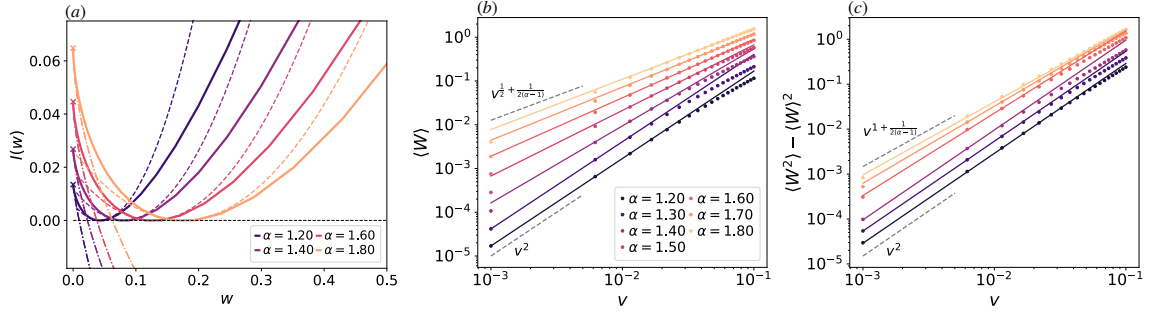


Figure 3.2: (a) Rate function as a function of the intensive irreversible work w for different values of α following a sudden critical quench of the long-range Kitaev chain with $h_i = 21$ and $h_f = 1$. Bold lines depict exact numerical results, dashed lines show the quadratic approximation near the average $w \approx \langle w \rangle$, and dot-dashed lines illustrate the universal scaling in the large deviation limit $w \ll \langle w \rangle$. (b)-(c) First and second moments of the irreversible work distribution as a function of the driving velocity v , for different values of α during slow linear critical driving of a long-range Kitaev chain with $h_i = 5$ and $h_f = 1$. Dots represent exact numerical results, while solid lines indicate power law fits of the numerical data. The system size is $N = 1024$.

The result in Eq.(3.24) readily provides a means to estimate long-range advantage. Indeed, if there is a value α_{adv} such that

$$\theta_{n,\alpha} > \frac{(d + nz_{\text{SR}}^d)\nu_{\text{SR}}^d}{1 + \nu_{\text{SR}}^d}, \quad (3.25)$$

then, the addition of long-range couplings improves the performance of the slow quench work protocol by reducing the irreversible work dissipated during the evolution.

3.3.3 Explicit examples of long-range advantage

We now provide few concrete examples where the applicability of the advantage principle in Eq.(3.25) can be verified explicitly. Firstly, we consider an analytically solvable model, i.e., the long-range Kitaev chain introduced in Section 1.5 and described by the fermionic Hamiltonian in Eq.(1.43).

Thanks to the quadratic nature of the model, the cumulant generating function of the work statistics, as defined in Eq.(3.4), can be computed analytically and reads:

$$\ln G(s) = -s\Delta\epsilon_0 t + \sum_{k>0} \ln \left[\frac{1 + \tan^2 \delta\phi_k e^{-2s\omega_{k,2}}}{1 + \tan^2 \delta\phi_k} \right] \quad (3.26)$$

where $\delta\phi_k = \phi_k^f - \phi_k^i$ represents the difference between the Bogoliubov angles diagonalizing the final and initial Hamiltonians, respectively. The bulk free energy density can be

expressed as

$$f_b = \frac{s\Delta\epsilon_0}{L} = \frac{s}{2L} \sum_{k>0} (\omega_{k,1} - \omega_{k,2}), \quad (3.27)$$

the surface free energy density as

$$f_s = \frac{1}{L} \sum_{k>0} \ln [1 + \tan^2 \delta\phi_k], \quad (3.28)$$

and the critical free energy density as

$$f_c(s) = -\frac{1}{L} \sum_{k>0} \ln [1 + \tan^2 \delta\phi_k e^{-2s\omega_{k,2}}]. \quad (3.29)$$

As shown in Section 1.5, in the weak long-range regime ($1 < \alpha < 2$), the quasiparticle spectrum is continuous in the thermodynamic limit. Accordingly, in the $L \rightarrow \infty$ limit, the sums over Fourier modes k can be approximated by integrals. The critical free energy density can then be written as

$$f_c(s) = -\int_0^\pi \frac{dk}{2\pi} \ln [1 + \tan^2 \delta\phi_k e^{-2s\omega_{k,2}}]. \quad (3.30)$$

To explore the large deviation region of the work distribution where $w \ll \langle w \rangle$, we consider the limit $s \rightarrow \infty$. In this limit, the integral in Eq. (3.29) is dominated by the low-energy modes near $k \approx 0$. Then, expanding the spectrum around $k \approx 0$, for $1 < \alpha < 2$, we obtain

$$f_c(s) \approx -\int_0^\pi \frac{dk}{2\pi} \ln \left[1 + \tan^2 \left(\frac{\pi(\alpha-1)}{4} \right) e^{-2sC_\alpha k^{\alpha-1}} \right], \quad (3.31)$$

where $C_\alpha = 2|\Gamma(1-\alpha)/\zeta(\alpha)|$. By changing variables to $y = 2sC_\alpha k^{\alpha-1}$ we get

$$f_c(s) \approx -\frac{1}{s^{1/(\alpha-1)}} \frac{1}{2\pi(2C_\alpha)^{1/(\alpha-1)}} \int_0^{2C_\alpha \pi^{\alpha-1} s} dy y^{\frac{1}{\alpha-1}-1} \ln \left[1 + \tan^2 \left(\frac{\pi(\alpha-1)}{4} \right) e^{-y} \right] \quad (3.32)$$

This integral converges and in the limit $s \rightarrow \infty$ can be carried out explicitly, yielding

$$f_c(s) \approx \frac{\Gamma\left(\frac{1}{\alpha-1}\right) \text{Li}_{1+\frac{1}{\alpha-1}}\left(-\tan^2\left(\frac{\pi(\alpha-1)}{4}\right)\right)}{2\pi(2C_\alpha)^{1/(\alpha-1)}} s^{-\frac{1}{\alpha-1}}, \quad (3.33)$$

where $\text{Li}_x(z) = \sum_{n=1}^\infty z^n/n^x$ is the polylogarithm function. Comparing this with the effective dimension prediction $f_c(s) \approx \Theta(0)s^{-d_{\text{eff}}}$, we identify

$$\Theta(0) = -\frac{\Gamma\left(\frac{1}{\alpha-1}\right) \text{Li}_{1+\frac{1}{\alpha-1}}\left(-\tan^2\left(\frac{\pi(\alpha-1)}{4}\right)\right)}{2\pi(2C_\alpha)^{1/(\alpha-1)}}, \quad d_{\text{eff}} = \frac{1}{\alpha-1}, \quad (3.34)$$

which matches the effective dimension predicted by Eq. (1.18).

Then, performing the Legendre transform explicitly, we derive the rate function

$$I(w) = 2f_{s,\alpha} - \alpha K_\alpha \left(\frac{w}{K_\alpha} \right)^{\frac{1}{\alpha}} = 2f_{s,\alpha} - \frac{d_{\text{eff}} + 1}{d_{\text{eff}}} K_\alpha \left(\frac{w}{K_\alpha} \right)^{\frac{d_{\text{eff}}}{d_{\text{eff}} + 1}}, \quad (3.35)$$

where we have introduced the α dependent factor

$$K_\alpha = d_{\text{eff}} \Theta(0) = -\frac{\Gamma\left(\frac{1}{\alpha-1}\right) \text{Li}_{1+\frac{1}{\alpha-1}}\left(-\tan^2\left(\frac{\pi(\alpha-1)}{4}\right)\right)}{2\pi(\alpha-1)(2C_\alpha)^{1/(\alpha-1)}}. \quad (3.36)$$

Next, we consider the regime of an infinitely slow linear quench with $h(t) = h_i - vt$, $t \in [0, (h_i - h_f)/v]$ and $v \rightarrow 0$. Here, it is useful to express the cumulant generating function $G(s)$ in terms of the excitation probabilities p_k of each Fourier mode during the dynamics, leading to

$$\ln G(s) = -s\Delta\epsilon_0 + L \int_0^\pi \frac{dk}{2\pi} \ln [1 + p_k(e^{-2s\omega_{k,2}} - 1)] \quad (3.37)$$

Expanding the logarithm in powers of $p_k(e^{-2s\omega_{k,2}} - 1)$, we get

$$\ln G(s) = -s\Delta\epsilon_0 + L \sum_{n=1}^{\infty} \frac{(-1)^{n+1}}{n} \int_0^\pi \frac{dk}{2\pi} p_k^n (e^{-2s\omega_{k,2}} - 1)^n, \quad (3.38)$$

where the series converges as long as $|p_k(e^{-2s\omega_k^f} - 1)| < 1$.

As shown in Section 1.5 in the limit of a slow driving protocol $v \rightarrow 0$, the first non-trivial correction to p_k takes the form of Eq. (1.71). Then, inserting this expression into the integral in Eq. (3.38), we obtain

$$f(s) = -\frac{1}{L}(\ln G(s) + s\Delta\epsilon_0) \approx -\sum_{n=1}^{\infty} \frac{(-1)^{n+1}}{n} \int_0^\pi \frac{dk}{2\pi} e^{-\frac{n\pi\Delta_k^2}{v}} (e^{-2s\omega_{k,2}} - 1)^n. \quad (3.39)$$

Due to the exponential decay of p_k , only low-energy modes can get excited. Therefore, the integral is dominated by the contributions at small Fourier modes k and we can replace the expressions for Δ_k and $\omega_{k,2}$ with their expansions around $k = 0$. Consequently, for a critical quench with $h_2 = 1$ and $1 < \alpha < 2$ we obtain

$$f(s) \approx -\sum_{n=1}^{\infty} \frac{(-1)^{n+1}}{n} \int_0^\pi \frac{dk}{2\pi} e^{-\frac{n\pi B_\alpha^2}{v} k^{2\alpha-2}} \left(e^{-2sC_\alpha k^{\alpha-1}} - 1 \right)^n, \quad (3.40)$$

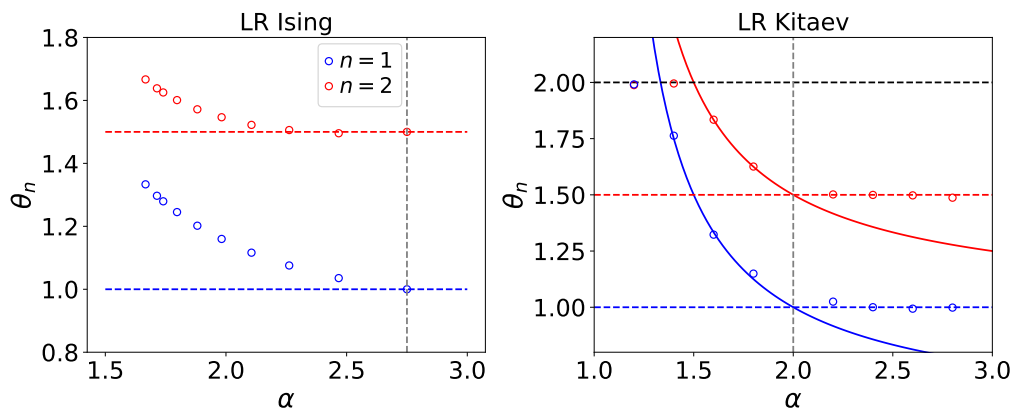


Figure 3.3: Scaling exponents for the first two cumulants, κ_1 (blue) and κ_2 (red), of the irreversible work statistics with respect to the driving velocity v , plotted as a function of α . The left panel shows results for a slow quench of the long-range Ising model, while the right panel displays results for the long-range Kitaev chain. In the long-range Ising case, dots represent numerical data obtained by combining the effective dimension prediction with precise numerical estimates of the short-range Ising critical exponents in the effective fractal dimension d_{eff} . For the long-range Kitaev chain, dots indicate the exponents obtained by fitting the exact numerical data for the work cumulants as a function of v with a power law function. Horizontal dashed lines represent the short-range values of the scaling exponents, and the gray vertical dashed line marks the value of $\alpha = \alpha^*$, above which the short-range results apply.

where $B_\alpha = \cos(\alpha\pi/2)\Gamma(1-\alpha)/\zeta(\alpha)$. Then, performing the change of variable $y^2 = k^{2\alpha-2}n\pi B_\alpha^2/v$, we have

$$f(s) \approx -\frac{1}{2\pi(\alpha-1)} \left(\frac{v}{\pi B_\alpha}\right)^{\frac{1}{2(\alpha-1)}} \times \sum_{n=1}^{\infty} \frac{(-1)^{n+1}}{n} \int_0^{\pi^{\alpha-1}|B_\alpha|\sqrt{\frac{\pi}{v}}} dy y^{\frac{1}{\alpha-1}-1} e^{-y^2 n} \left(e^{-2s\frac{C_\alpha}{B_\alpha}\sqrt{\frac{v}{\pi}}y} - 1\right)^n. \quad (3.41)$$

Finally, keeping only the leading order contributions as $v \rightarrow 0$ we find

$$f(s) \approx \frac{1}{2\pi(\alpha-1)} \left(\frac{v}{\pi B_\alpha}\right)^{\frac{1}{2(\alpha-1)}} \sum_{n=1}^{\infty} \frac{1}{n} \int_0^{\infty} dy y^{n+\frac{1}{\alpha-1}-1} e^{-y^2 n} \left(2s\frac{C_\alpha}{B_\alpha}\right)^n \left(\frac{v}{\pi}\right)^{\frac{n}{2}} \quad (3.42)$$

$$= \sum_{n=1}^{\infty} f_{n,\alpha}(s) v^{\frac{1}{2(\alpha-1)} + \frac{n}{2}}. \quad (3.43)$$

This gives us the scaling of the n th cumulant

$$\kappa_n \propto v^{\frac{1}{2(\alpha-1)} + \frac{n}{2}}. \quad (3.44)$$

As expected, also this scaling is in agreement with the effective dimension prediction with $d_{\text{eff}} = 1/(\alpha-1)$.

Finally, as a second example, we consider the long-range quantum Ising chain which, as shown in Section 1.4 is an interacting and experimentally relevant model. In this case, the scaling exponents for the work cumulants θ_n in the slow quench scenario can be approximated by inserting precise numerical estimates for the critical exponents of the short-range Ising model in d_{eff} dimension [131] into the effective dimension prediction of Eq. (3.24). The resulting θ_n for the first two cumulants $n = 1, 2$ are plotted as a function of α in Fig. 3.3(b) and compared with their corresponding short-range values (horizontal dashed lines). Notably, in this interacting example, the first two cumulants of the work statistics satisfy the long-range advantage condition (3.25) as long as $\alpha < \alpha^*$, with $\alpha^* \approx 3 - \eta_{\text{SR}}(d_{\text{eff}} = 1) = 2.75$.

3.4 Application to quantum heat-engines

With the results from Section 3.3 in our hands, we are now equipped to design a quantum thermal cycle that leverages the presence of long-range interactions in its working substance. Specifically, we focus on the paradigmatic example of the long-range Kitaev chain undergoing a quantum Otto cycle. We identify several advantages arising from the presence of long-range interactions:

1. **Enhanced adiabatic optimal performance:** In the limit of an infinitely slow cycle, we observe enhanced optimal performances of the device in its most useful operation modes: the heat-engine mode and the refrigerator mode.

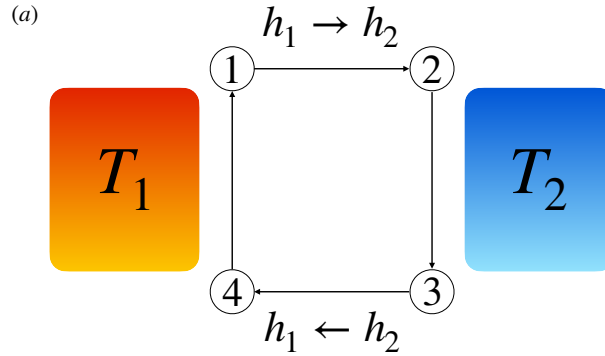


Figure 3.4: Schematic representation of the quantum Otto cycle.

2. **Reduction in Nonadiabatic Losses:** In a finite-time cycle involving the crossing of a quantum critical point, selecting a long-range interacting working substance leads to a significant reduction in nonadiabatic energy losses compared to its short-range counterpart. This aligns with the general results presented in Section 3.3.

3.4.1 The quantum Otto cycle

The quantum Otto cycle,[145, 146, 13] consists of the following four strokes (see Fig. 3.4):

- **First stroke: unitary decrease of h ($1 \rightarrow 2$).** Initially, the system is in thermal equilibrium with a hot reservoir at temperature $T_1 = 1/\beta_1$ and $h = h_1$. The system is decoupled from the bath and undergoes a unitary evolution where the driving parameter h changes from h_1 to h_2 .
- **Second stroke: thermalization at fixed h ($2 \rightarrow 3$).** The driving parameter is kept fixed at $h = h_2$, and the system is coupled to a thermal bath at temperature $T_2 = 1/\beta_2$, allowing it to reach thermal equilibrium.
- **Third stroke: unitary increase of h ($3 \rightarrow 4$).** The system undergoes another unitary evolution that brings the chemical potential back to its initial value $h_2 \rightarrow h_1$.
- **Fourth stroke: thermalization at fixed h ($4 \rightarrow 1$).** the system at fixed $h = h_1$ is coupled again to the hot bath, reaching equilibrium at temperature T_1 and completing the cycle.

At each stage, the system's state and corresponding average energy are given by

$$\rho_1 = e^{-\beta_1 H_1} / Z_1, \quad E_1 = \text{Tr} \rho_1 H_1, \quad (3.45a)$$

$$\rho_2 = U \rho_1 U^\dagger, \quad E_2 = \text{Tr} \rho_2 H_2, \quad (3.45b)$$

$$\rho_3 = e^{-\beta_2 H_2} / Z_2, \quad E_3 = \text{Tr} \rho_3 H_2, \quad (3.45c)$$

$$\rho_4 = \tilde{U} \rho_3 \tilde{U}^\dagger, \quad E_4 = \text{Tr} \rho_4 H_1, \quad (3.45d)$$

where $H_i = H(h_i)$, $Z_i = \text{Tr} e^{-\beta_i H_i}$ $i = 1, 2$, U and \tilde{U} are the unitary evolution operators associated to the first and the third stroke respectively. As in the previous Section also here we assume, for simplicity, a linear time dependence of the driving parameter during the unitary strokes. Then the driving protocol corresponding to the first step $1 \rightarrow 2$ can be written as

$$h(t) = h_1 - vt \quad \text{for } t \in [0, \tau], \quad (3.46)$$

where $v = (h_1 - h_2)/\tau$ is the sweep rate. The driving protocol during the third step of the cycle $3 \rightarrow 4$ is given by $\tilde{h}(t) = h(\tau - t)$, for $t \in [0, \tau]$. The corresponding unitary evolutions are then

$$U = \text{T exp} \left[-i \int_0^\tau dt H[h(t)] \right], \quad (3.47)$$

$$\tilde{U} = \text{T exp} \left[-i \int_0^\tau dt H[\tilde{h}(t)] \right], \quad (3.48)$$

where T exp denotes the time-ordered exponential. During the second and fourth strokes, the system interacts only with the baths, reaching thermal equilibrium. While long-range interacting systems are known to evade thermalization allowing for quasistationary states [90, 103], it can be shown that thermal equilibrium is safely reachable when $\alpha_1, \alpha_2 > 1$ [179]. Then, all the thermodynamic quantities can be computed using the equilibrium populations for the Fourier modes. For the example of the long-range Kitaev chain these are simply given by the Fermi-Dirac distribution, of the Bogoliubov fermions diagonalizing the chain, at an inverse temperature β_i and with the dispersion relation $\omega_{k,i} = \omega_k(h_i)$ of Eq. (1.50), for $i = 1, 2$, reading

$$\langle \gamma_k^\dagger \gamma_k \rangle = f(\omega_{k,i}) = \frac{1}{1 + e^{\beta_i \omega_{k,i}}}. \quad (3.49)$$

Then, in this case, the internal energy is given by

$$\mathcal{E}_i = \sum_k \omega_{k,i} \left(\langle \gamma_k^\dagger \gamma_k \rangle - 1/2 \right) = - \sum_{k>0} \omega_{k,i} \tanh \left(\frac{\beta \omega_{k,i}}{2} \right).$$

Since during the second and the fourth strokes the external driving is switched off and the system interacts only with the baths, then energy is exchanged with them only in the form of heat

$$Q_1 = E_3 - E_2 \quad (3.50)$$

$$Q_2 = E_1 - E_4. \quad (3.51)$$

Then, according to the first law of thermodynamics, the work done over the cycle is

$$W = Q_1 + Q_2. \quad (3.52)$$

The average energy exchanges Q_1, Q_2 and W fully characterize the cycle's operation. Depending on the signs of Q_1, Q_2 and W , our engine may operate in any of the following four modes

$$[E] : Q_1 \geq 0, Q_2 \leq 0, W \geq 0; \quad (3.53a)$$

$$[R] : Q_1 \leq 0, Q_2 \geq 0, W \leq 0; \quad (3.53b)$$

$$[A] : Q_1 \geq 0, Q_2 \leq 0, W \leq 0; \quad (3.53c)$$

$$[H] : Q_1 \leq 0, Q_2 \leq 0, W \leq 0; \quad (3.53d)$$

where $[E]$ denotes energy extraction (heat engine), $[R]$ denotes refrigerator, $[A]$ denotes thermal accelerator, and $[H]$ denotes heater [15, 13].

In the case of the long-range Kitaev chain the energy exchanges take the form

$$Q_1 = - \sum_{k>0} \omega_{1,k} (f_{2,k} + f_{1,k}(2p_k - 1)), \quad (3.54a)$$

$$Q_2 = - \sum_{k>0} \omega_{2,k} (f_{1,k} + f_{2,k}(2p_k - 1)), \quad (3.54b)$$

$$W = Q_1 + Q_2, \quad (3.54c)$$

where p_k , are the nonadiabatic transition probabilities during the unitary stroke of the cycle, and we have introduced the shortcut notation $f_{i,k} = \tanh(\beta_i \omega_{i,k})$, for $i = 1, 2$.

3.4.2 Adiabatic cycle

Let us now analyze the case of an infinitely slow cycle, i.e., the limit $v \rightarrow 0$. This regime is usually referred to as adiabatic, since the unitary evolution is sufficiently slow for the adiabatic theorem to hold, preventing transitions between the instantaneous eigenstates of the Hamiltonian, and leading to $p_k \approx 0$. The adiabatic approximation breaks down as the energy gap closes. Strictly speaking, however, this happens only in the thermodynamic limit $N \rightarrow \infty$. Accordingly, for any finite N , one can choose the driving time scale such

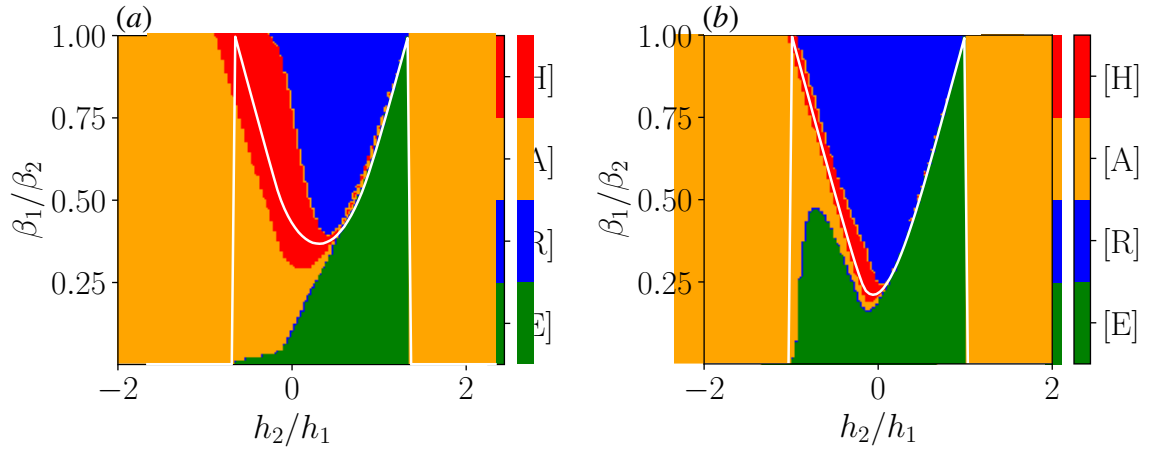


Figure 3.5: Operation mode diagram illustrating regions in the parameter space of β_1/β_2 and h_2/h_1 , corresponding to different operation modes. Distinct colors represent different operation modes: blue for the refrigerator [R], green for the heat engine [E], yellow for the thermal accelerator [A], and red for the heater [H]. White lines denote the boundaries of the operation mode regions for a working substance composed of identical and independent qubits (3.57). Panel (a) depicts the nearest neighbor case with $\alpha \rightarrow \infty$, while panel (b) shows the long-range case with $\alpha = 1.5$. The system size is fixed at $N = 200$, with initial temperature $T_1 = 100$, and initial value of the driving parameter $h_1 = 2$.

that the adiabatic approximation is justified, allowing us to set $p_k \approx 0$ in Eqs. (3.54) obtaining

$$Q_1 = \sum_{k>0} \omega_{1,k} (f_{2,k} - f_{1,k}), \quad (3.55a)$$

$$Q_2 = - \sum_{k>0} \omega_{2,k} (f_{2,k} - f_{1,k}), \quad (3.55b)$$

$$W = \sum_{k>0} (\omega_{1,k} - \omega_{2,k}) (f_{2,k} - f_{1,k}). \quad (3.55c)$$

Figure 3.5 illustrates the regions of parameters β_2 and h_2 , for fixed values of β_1 and h_1 , corresponding to the different operation modes defined in Eq. (3.53). Panel (a) shows the nearest neighbor case corresponding to the $\alpha \rightarrow \infty$ limit, while panel (b) shows the long-range case with $\alpha = 1.5$.

To highlight the effects of long-range couplings, these plots are compared with the regions obtained when the long-range Kitaev chain is replaced by N identical and independent single qubits. Each qubit has a frequency given by the average spectrum of the corresponding fermionic chain over all Fourier modes:

$$\bar{\omega} = \frac{1}{N} \sum_k \omega_k. \quad (3.56)$$

The boundaries of the regions for the independent qubits case are depicted as white lines in Fig. 3.5 and offer a rough estimation for the engine operation mode. In this scenario, where only one level-spacing is present, the region boundaries can be derived using the results from Ref. [13] for the operation modes of a single qubit:

$$[E] : \frac{\beta_1}{\beta_2} \leq \frac{\bar{\omega}_2}{\bar{\omega}_1} \leq 1, \quad (3.57a)$$

$$[R] : \frac{\bar{\omega}_2}{\bar{\omega}_1} \leq \frac{\beta_1}{\beta_2}, \quad (3.57b)$$

$$[A] : \frac{\bar{\omega}_2}{\bar{\omega}_1} \geq 1, \quad (3.57c)$$

where $\bar{\omega}_{1,2}$ corresponds to Eq. (3.56) for $h = h_{1,2}$ respectively, and we have assumed, without loss of generality, $\beta_1 \leq \beta_2$.

Note that conditions (3.57) rule out the possibility of a single qubit acting as a heater ($[H]$). Therefore, this regime cannot be well described within the mean-spacing approximation in the adiabatic limit. On the other hand, in the region $h_2/h_1 > 0$, where the heater phase is absent, the operation mode phase diagram is well reproduced by the mean-spacing approximation, see Eq. (3.57), regardless of the value of α .

By comparing the two diagrams in Fig. 3.5, we observe that the heater region in the long-range case (panel (b)) is significantly reduced compared to the nearest neighbor case

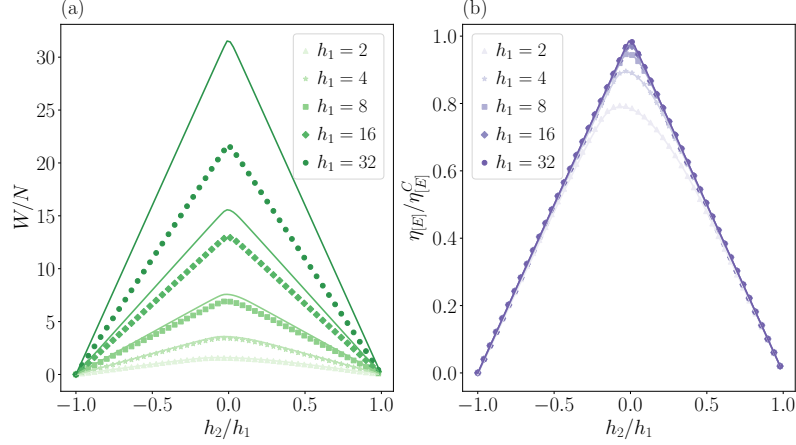


Figure 3.6: Work output (panel a) and engine efficiency (panel b), plotted as a function of h_2/h_1 , for different values of h_1 corresponding to different colors. Exact values (3.55c) are represented as scatter plots with different markers (one for each value of h_1), while bold lines refer to the approximated result of Eq. (3.59). The system size is $N = 200$, the temperatures of the baths are fixed to $T_1 = 100$, $T_2 = 0.01$.

(panel (a)). Additionally, operation mode regions shapes are closer to the identical and independent qubits even in the $h_2/h_1 < 0$ region. Moreover, the $[R]$ (refrigeration) and $[E]$ (engine) regimes, which are the most relevant to technological applications, are enhanced and become prevalent across the entire parameter region $|h_2/h_1| < 1$. In the following, we focus on optimizing these two regimes within the parameter space, identifying the advantages that arise from the presence of long-range couplings compared to the corresponding local systems.

3.4.3 Heat Engine operation mode

The purpose of a heat engine is to harness the energy flow from a hot reservoir to a cold one, extracting useful energy in the form of work. Thus, optimizing the performance of a device operating in the $[E]$ mode involves maximizing the work output. Another estimator of the engine performance is the heat engine efficiency, defined as the ratio between the energy gained as work and the heat extracted from the hot reservoir:

$$\eta_{[E]} = \frac{W}{Q_1} = 1 + \frac{Q_2}{Q_1}. \quad (3.58)$$

According to the second law of thermodynamics, this efficiency is always less than the Carnot efficiency $\eta_{[E]}^C = 1 - T_2/T_1$ [156]. The functioning of a heat engine is naturally boosted when the temperature difference between the reservoirs is large, favoring energy

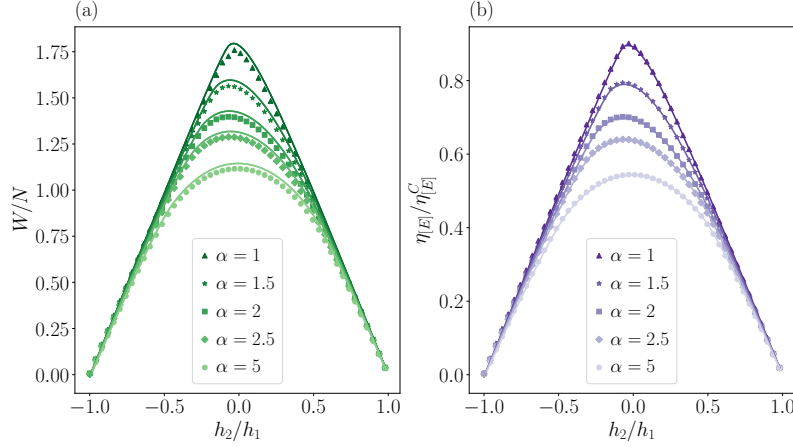


Figure 3.7: Work output (panel a) and engine efficiency (panel b), plotted as a function of h_2/h_1 , for different values of $\alpha_1 = \alpha_2 = \alpha$ corresponding to different colors. Exact values (3.55c) are represented as scatter plots with different markers (one for each value of α), while bold lines correspond to the approximate result of Eq. (3.59). The system size is $N = 200$, the temperatures of the baths are fixed to $T_1 = 100$, $T_2 = 0.01$ and the initial chemical potential value is $h_1 = 2$.

flow and consequently the work extraction. Indeed, in this regime, the Carnot efficiency gets close to unity. This basic physical intuition leads us to focus on the region of parameters where $T_2 \ll T_1$ as the most interesting for the $[E]$ operation. Specifically, we consider $T_2 \ll \bar{\omega}(h) \ll T_1$, with $\bar{\omega}(h)$ playing the role of a typical energy scale of the system. Thus, the working substance is near the ground state when in equilibrium with the cold bath and near the maximally mixed state when in equilibrium with the hot bath. This leads to the following expression for the work extracted

$$W \simeq W_0 \equiv N(\bar{\omega}_1 - \bar{\omega}_2)/2, \quad (3.59)$$

which is fully determined by the average level spacing $\bar{\omega}_i$, $i = 1, 2$ for $h = h_{1,2}$. It follows that the optimal work output is reached for the values of h_1, h_2 that respectively maximise and minimise the function $\bar{\omega}(h)$ in Eq. 3.56, namely

$$W_{\max} \simeq W_{0,\max} = \frac{N}{2}(\max_h[\bar{\omega}] - \min_h[\bar{\omega}]), \quad (3.60)$$

where the optimization has to be performed over the values of h compatible with the approximation (3.59), i.e., such that $T_2 \ll \bar{\omega}(h) \ll T_1$. Within the same approximation, the heat engine efficiency reads

$$\eta_{[E]} \simeq \eta_{[E]}^0 \equiv 1 - \frac{\bar{\omega}_2}{\bar{\omega}_1} \leq 1 - \frac{\min_h[\bar{\omega}]}{\max_h[\bar{\omega}]} \quad (3.61)$$

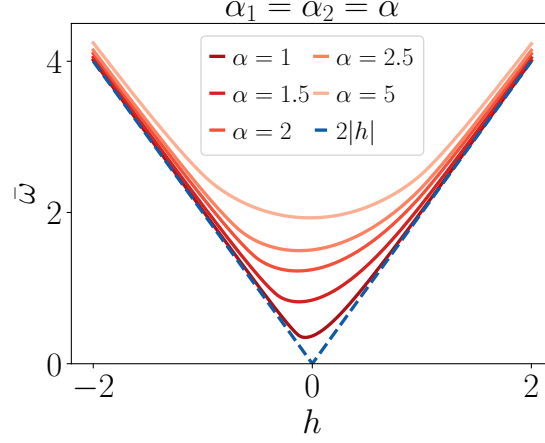


Figure 3.8: Average level spacing (3.56), as a function of the chemical potential h . Different colors correspond to different values of α . The system size is $N = 500$.

Remarkably, this choice of h_1 and h_2 allows to maximize both the work output and the cycle efficiency. In Fig. 3.6(a) and (b) the exact work output W , and the exact engine efficiency $\eta_{[E]}$ respectively (scatter plots) are compared with W_0 and $\eta_{[E]}^0$ (solid lines) for different values of h_1, h_2 and with $T_1 = 100, T_2 = 0.01$ and $\alpha = 1.5$. We notice that the approximation $W \simeq W_0$ breaks down for large values of h_1 , when $\bar{\omega}(h_1)$ becomes of the same order of T_1 , while $\eta_{[E]}^0$ remains a good estimate of $\eta_{[E]}$ even in this regime. Finally, let us notice that, regardless of the validity of the approximation, the maxima of $\eta_{[E]}$ and W are actually close.

In Fig. 3.7 we plot W and $\eta_{[E]}$ against h_2/h_1 , for different values of α , showing that they grow as the range of the interaction increases (α decreases), signaling a clear advantage of the long-range regime. This advantage can be traced back to the properties of the spectrum of the system, encoded in the average level spacing $\bar{\omega}$. In fact, the minimum of $\bar{\omega}(h_2)$, which corresponds to the maximum of both W_0 and $\eta_{[E]}^0$, is affected by the presence of long-range interactions as shown in Fig. 3.8.

3.4.4 Refrigerator operation mode

In the typical situation in which a quantum refrigerator operates we may expect the two temperatures to be pretty similar $T_2 \lesssim T_1$, since we can imagine that also the baths are embedded in the same quantum hardware of the working substance. Additionally, to ensure the system operates deeply within the quantum regime, the temperatures involved in the cycle should be much smaller than the system's energy scale, specifically $T_2 \lesssim T_1 \ll \bar{\omega}$. Under these assumptions, the heat extracted from the cold reservoir can be expressed as

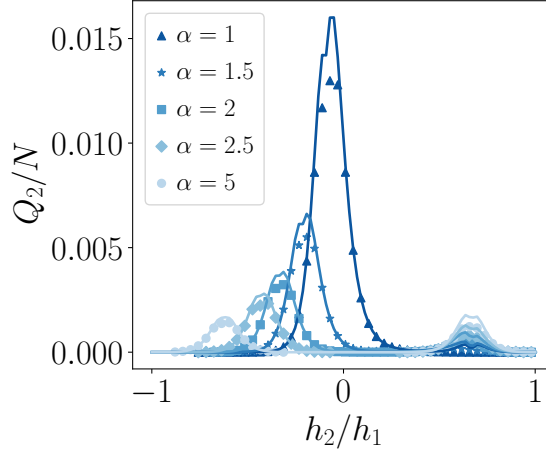


Figure 3.9: Heat extracted from the cold reservoir Q_2 , as a function of h_2/h_1 . Scatter plots indicate the exact values (3.55b), bold lines indicate the approximated result (3.62). Different colors correspond to different values of $\alpha_1 = \alpha_2 = \alpha$. The baths temperatures are fixed to $T_1 = 0.1$, $T_2 \simeq 0.099$.

follows

$$Q_2 \simeq \sum_{k>0} \omega_{2,k} e^{-\beta_2 \omega_{2,k}} \left[1 - \tanh \left(\frac{\beta_2 \omega_{2,k} - \beta_1 \omega_{1,k}}{2} \right) \right]. \quad (3.62)$$

Since the above expression is positive definite, we can conclude that within the considered approximation the Otto cycle always operates as a refrigerator. However, far from the quantum critical points, the heat extracted from the cold reservoir can be approximated as

$$Q_2 \simeq N \min_k [\omega_{2,k}] e^{-\beta_2 \min_k [\omega_{2,k}]}. \quad (3.63)$$

indicating that Q_2 exhibits an exponentially decaying behavior as $T_2 \rightarrow 0$. On the other hand, as h_2 becomes close to $h_c(\alpha)$ the spectrum is no longer gapped, so the above considerations do not apply. Instead in this regime, the main contribution to Q_2 comes from the soft modes, resulting in a power law decay in T_2

$$Q_2 \simeq NK(\alpha) T_2^{1+1/z}, \quad (3.64)$$

where $K(\alpha)$ is an α dependent prefactor, and z is the dynamical critical exponent which, in general, depends on α . Specifically, as detailed in Section 1.5, at the $h_2 = 1$ critical point of the long-range Kitaev chain we have

$$z = \begin{cases} \alpha - 1 & \text{for } \alpha < 2 \\ 2 & \text{for } \alpha > 2, \end{cases} \quad (3.65)$$

while for the $h_2 = -1 + 2^{\alpha-1}$ critical point $z = 1$.

Since close to the $h_2 = 1$ critical point $1/z$ grows indefinitely as $\alpha \rightarrow 1$, the presence of long-range interactions does not result in any advantage at low temperatures. However, near the $h_2 = -1 + 2^{\alpha-1}$ critical point, z does not depend on α . In this scenario, the factor $K(\alpha)$ can indeed provide an advantage. This is confirmed by the data shown in Fig. 3.9, where Q_2/N is plotted as a function of h_2 for different values of α and temperatures $T_1 = 0.1$ and $T_2 = 0.099$. The figure clearly demonstrates an advantage as the range of the interaction increases.

The distinct low-temperature scalings in Eq. (3.64) result in peaks in Q_2 at $h_2/h_1 = h_c(\alpha)/h_1$, indicating enhanced cooling capability at quantum criticality, as illustrated in Fig. 3.9. This effect is amplified by the presence of long-range interactions, leading to progressively larger peaks as $\alpha \rightarrow 1$, thereby showing a long-range advantage in the most significant regime, i.e., refrigerator operation. It is noteworthy that while the heat engine configuration is optimized by a long-range interacting machine operating close to the $h_2 = 1$ critical point, the refrigerator operates optimally in the vicinity of the $h_2 = -1 + 2^{1-\alpha}$ critical point.

3.4.5 Finite time cycle

Finally, we consider the finite-time performance of the device. Specifically, we examine a linear driving protocol for the unitary step of the cycle, characterized by the driving velocity v (see Eq. (3.46)), which we choose to be small but finite. In this case, the general results of Section 3.3.2 apply, allowing us to identify the origin of the long-range advantage in the reduction of nonadiabatic energy losses generated during the finite-time dynamics.

Before delving into the role of long-range couplings in finite-time performances, let us first consider a single mode and the corresponding two-level system formed by $|0_k, 0_{-k}\rangle$ and $|1_k, 1_{-k}\rangle$. It is known [13] that when $p_k > 0$, a region in parameter space corresponding to the heater $[H]$ appears and becomes the only possible regime when $p_k \geq 1/2$, as in this case the energy exchanges become negative definite. This behavior occurs for the long-range Kitaev chain as well if the driving is so fast that $p_k > 1/2$ for all values of k .

Moreover, for any finite-time driving, the presence of finite transition probabilities p_k hinders engine performance by enhancing the irreversible character of the cycle. This can be demonstrated by explicitly computing the entropy production of the cycle, defined as $\Sigma = \beta_1 Q_1 + \beta_2 Q_2$ in the finite-time case. The second law of thermodynamics, in the form of the Clausius inequality, constrains this quantity to be non-positive ($\Sigma \leq 0$), with equality holding only if the cycle is perfectly reversible. Therefore, we can view Σ as an indicator of the cycle's irreversibility, reflecting how close the device performance is to the optimal Carnot bound. Interestingly, in our case, the entropy production can be written as the

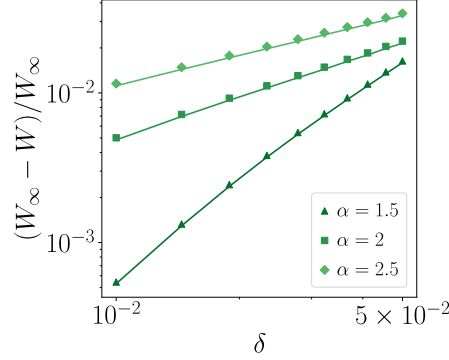


Figure 3.10: Nonadiabatic work loss ratio as a function of the driving velocity δ , for different values of $\alpha_1 = \alpha_2 = \alpha$, corresponding to different colors and markers. Scatter plots indicate the exact numerical values while bold lines indicate the approximated result (3.69). The cycle parameters $h = 2$, $h_2 = 0$, $T_1 = 100$, $T_2 = 0.01$. The system size is $N = 500$.

sum of two contributions: $\Sigma = \Sigma_0 + \Sigma_v$. The first term, given by

$$\Sigma_0 = \sum_{k>0} (\beta_1 \omega_{1,k} - \beta_2 \omega_{2,k}) [f_{2,k} - f_{1,k}], \quad (3.66)$$

is present even in the infinitely slow cycle and is unavoidable, as it is due to the intrinsic irreversibility of the two thermalization strokes of the cycle. Thus, $\Sigma_0 = 0$ only at the Carnot point, where all energy exchanges are null ($Q_1 = Q_2 = W = 0$). On the other hand, the second contribution, given by

$$\Sigma_v = \sum_{k>0} [\beta_1 \omega_{1,k} f_{2,k} - \beta_2 \omega_{2,k} f_{1,k}] (1 - P_k), \quad (3.67)$$

is present only when the unitary strokes are performed at a finite velocity. Notably, each term in the sum of Eq. (3.67) is proportional to the nonadiabatic transition probability $1 - P_k$, explicitly showing that these provide an additional source of irreversibility, resulting in poorer efficiency in finite-time cycles.

With these concepts in mind, we are now ready to consider the finite-time performance of two relevant operation modes: the heat engine ($[E]$) and the refrigerator ($[R]$).

For the $[E]$ operation mode, we examine the nonadiabatic work losses, i.e., the difference between the adiabatic work W_0 extracted in an infinitely slow cycle and the work W extracted in a more realistic finite-time scenario. This difference can be expressed as [180]

$$W_0 - W = \sum_{k>0} [2\omega_{1,k} f_{2,k} + 2\omega_{2,k} f_{1,k}] p_k \quad (3.68)$$

In the optimal regime for the heat engine ($T_2 \ll \bar{\omega} \ll T_1$), this becomes

$$W_0 - W \simeq 2 \sum_{k>0} \omega_{1,k} p_k. \quad (3.69)$$

This expression matches the one obtained in Eq. (3.15) for the irreversible work in slow quench dynamics, derived through completely general arguments. Since $\omega_{1,k}$ remains finite as $k \rightarrow 0$, the above expression leads to the scaling with $v \rightarrow 0$,

$$W_0 - W \propto v^\theta, \quad (3.70)$$

where

$$\theta = \begin{cases} (2\alpha - 2)^{-1} & \text{for } \alpha \leq 2, \\ 1/2 & \text{for } \alpha > 2. \end{cases} \quad (3.71)$$

Thus, if the system is sufficiently long-range ($\alpha < 2$), then $\theta_{LR} = 1/(2\alpha - 2) > \theta_{SR} = 1/2$. This observation indicates that in the limit of a slow cycle ($v \rightarrow 0$), dynamical excitations are suppressed in the presence of long-range interactions. This long-range advantage mitigates one of the main limitations of quantum thermal devices: the trade-off between power and efficiency. Figure 3.10 shows the nonadiabatic work loss ratio $1 - W/W_0$ as a function of v , for different values of α . We notice that, excellent agreement is found between the exact numerical data (scatter plots) and the approximated result (3.69) we used to extract the universal scaling in Eq. (3.70). Moreover, as predicted, work losses are significantly reduced when $\alpha < 2$.

Finally, a similar reasoning applies to the refrigerator [R] in its most realistic temperature setting $T_2 \lesssim T_1 \ll \bar{\omega}$. As discussed in Sec. 3.4.4, in this case, the relevant quantity to be optimized is the heat extracted from the cold reservoir Q_2 . As discussed in Sec. 3.4.4, the relevant quantity to be optimized is the heat extracted from the cold reservoir, Q_2 . Considering the difference between the adiabatic cooling capability $Q_{2,0}$ and the heat extracted in a finite-time cycle, for the temperature range $T_2 \lesssim T_1 \ll \bar{\omega}$, we have

$$Q_{2,0} - Q_2 \simeq 2 \sum_{k>0} \omega_{2,k} p_k. \quad (3.72)$$

To determine the scaling of this quantity for a slow cycle ($v \rightarrow 0$), we must distinguish whether h_2 is critical or not. In the non-critical case, we find the same result as in Eq. (3.70). Instead, for $h_2 = 1$ the dynamical scaling is affected by the presence of soft modes in $\omega_{2,k}$ as well, and we obtain the scaling of Eq. (3.44). We find then the two different scaling behaviors

$$Q_{2,0} - Q_2 \propto \begin{cases} \delta^\theta & h_2 \neq 1 \\ \delta^{\theta+1/2} & h_2 = 1 \end{cases}, \quad (3.73)$$

In any case, we conclude that the presence of long-range couplings leads to an advantage for cooling capability in finite-time cycles as well.

3.5 Closing remarks

In this Chapter, we have explored the robustness of long-range interacting quantum systems against dynamic excitation generation during non-adiabatic dynamics, compared to short-range systems. By examining the universal behavior of quantum work statistics, we identified conditions under which long-range interactions reduce energy losses during non-adiabatic evolution, which is crucial for improving the efficiency and power output of quantum engines, especially in finite-time quantum thermal cycles.

Specifically, in the sudden quench scenario, we demonstrated that the work statistics in a quantum system can be mapped to a classical problem on a slab geometry in a higher effective dimension $d_{\text{eff}} + 1$. This mapping reveals a higher probability of observing reduced irreversible work in long-range systems compared to systems with short-range interactions, confirming that long-range interactions effectively decrease non-adiabatic energy losses during rapid quenches.

Moreover, for slow driving protocols, we derived the scaling behavior of the cumulants of the work distribution. The effective dimension approach accurately predicts these scalings, showing that long-range systems exhibit a distinct advantage in reducing non-adiabatic excitations over a broad range of interaction exponents α . We identified a critical range of α values where the scaling exponents θ_n exceed those of short range systems, highlighting the long-range advantage.

Our general findings were substantiated through two prototypical examples: the long-range Kitaev chain and the long-range quantum Ising chain. In the Kitaev chain, we analytically computed the work statistics, demonstrating excellent agreement with our effective dimension predictions. For the Ising chain, numerical estimates of critical exponents validated the long-range advantage condition across the significant range of values $\alpha \in [d/2, \alpha^*]$, where long-range interactions actually play a role in affecting the system's universal properties.

We further investigated the performance of a quantum thermal machine consisting of a chain of fermions with power-law decaying interactions undergoing a quantum Otto cycle. By exactly computing the energy exchanged during the cycle, we provided a detailed characterization of the device, identifying the most useful operation modes for quantum technological applications, namely the heat-engine and refrigerator modes. Focusing on these two modes, we examined the role of long-range interactions in optimizing device performance, detecting several sources of long-range advantage compared to the nearest-neighbor case. Remarkably, these results demonstrate high thermodynamic efficiency even when operating at finite power.

Overall, our comprehensive characterization of the quantum thermodynamics of long-range systems provides a robust framework for understanding their enhanced performance in quantum thermodynamic cycles. These insights pave the way for developing more efficient quantum thermal engines leveraging the unique properties of long-range interactions.

Chapter 4

Floquet Physics in long-range systems

4.1 Discrete Floquet time crystals

The efficacy of technological application of quantum mechanics, such as reliable quantum communication [181], high-precision quantum metrology [182], and fault-tolerant quantum computation [133], depends on the capability of preserving systems out-of-equilibrium, evading the detrimental effects of thermalization, which naturally leads to the loss of locally stored quantum information. Accordingly, much theoretical and experimental effort has been devoted to the study of out-of-equilibrium phenomena [178, 183, 184, 185] including, among the others, thermalization of isolated quantum many-body systems [186, 187, 188, 189], dynamical phase transitions [190, 191, 192, 193, 194] and, finally, the celebrated Discrete Floquet Time Crystals (DFTC).

The concept of spontaneous breaking of continuous time-translational symmetry in quantum many-body systems was first brought to broad attention in Ref. [195]. Shortly thereafter, it was established that such non-equilibrium phases are impossible in equilibrium settings [196, 197]. However, discrete time-translational symmetry, achievable in periodically (Floquet) driven systems, can indeed be spontaneously broken [198, 199, 200]. This phenomenon is referred to as DFTC, where the discrete time-translation symmetry inherent in the periodically driven Hamiltonian $H(t) = H(t + T)$ is spontaneously broken. Consequently, expectation values of relevant observables exhibit oscillations with a period that is an integer multiple of T . Several experimental observations of DFTCs have been reported in the past decade [201, 202, 203, 204].

Following Ref. [205] we say that a DFTC phase exists if, for a class of states $|\psi\rangle$ with short-ranged connected correlations [199], there always exists an observable \hat{O} , such that

the time-evolved expectation value in the thermodynamic limit $N \rightarrow \infty$,

$$O(t) = \lim_{N \rightarrow \infty} \langle \Psi(t) | \hat{O} | \Psi(t) \rangle, \quad (4.1)$$

satisfies the following conditions [205]:

1. **Time-translation symmetry breaking:** $O(t + T) \neq O(t)$, although $H(t) = H(t + T)$. This is equivalent to have long-range correlated Floquet eigenstates of the propagator $U_F = U(t + T, t)$ [199].
2. **Rigidity:** $O(t)$ must display periodic oscillations, with some period τ , in a finite and connected region of the Hamiltonian parameters space.
3. **Persistence:** in the large system size limit $N \rightarrow \infty$, the oscillations of $O(t)$ must persist for infinitely long time.

These criteria cannot be met by a generic local many-body quantum system due to the external driving, which typically induces relaxation towards an infinite-temperature state, thereby hindering long-lived oscillations. To protect ordering against relaxation, a mechanism is required to control the impact of dynamically generated excitations.

Prethermal stability can be maintained through long-range interactions, which are known to produce metastable states with lifetimes that increase as the system size approaches the thermodynamic limit [206, 95, 103]. Then, it is natural that the investigation of DFTCs in clean systems has been primarily focused on long-range interacting models where the robustness of collective oscillations in presence of periodic drive is guaranteed. More precisely, stable DFTC phases can only be found for $\alpha < d$ [205, 207, 208, 209], while for $\alpha > d$, the lifetime of oscillations is expected to be finite in the $N \rightarrow \infty$ limit [210, 211, 212].

4.2 The long-range kicked quantum Ising chain

The kicked Ising spin chain is a prototypical model for studying Floquet-driven quantum systems and has been extensively analyzed from a theoretical perspective [205, 213, 212, 210, 4]. Specifically, we consider a time-dependent version of the long-range quantum Ising Hamiltonian introduced in Eq. (1.19), where the time dependence arises from a periodically driven transverse magnetic field $h(t)$ with period T . The driving field is expressed as

$$h(t) = \psi \sum_{n=1}^{\infty} \delta(t - nT). \quad (4.2)$$

Additionally, for later purposes, we also consider a generalized version of the model where the spins interact with their first R neighbors. Initially, we will focus on the truly long-range case with $R = N$ (see Section 4.3), while the finite R case will be considered for

quantum simulation applications (see Section 4.4). The system Hamiltonian is then given by

$$H(t) = - \sum_{j=1}^N \sum_{r=1}^R J_r \hat{\sigma}_j^x \hat{\sigma}_{j+r}^x + h(t) \sum_{j=0}^{N-1} \hat{\sigma}_j^z, \quad (4.3)$$

The effect of the impulsive magnetic field applied at integer multiples of the driving period $t = nT$ is to impose a global rotation of each spin by an angle 2ψ along the z -axis. Accordingly, the Floquet dynamics is obtained by periodically intertwining the evolution generated by the Ising Hamiltonian at zero transverse field

$$V = \prod_{j=1}^N \prod_{r=1}^R e^{iT J_r \hat{\sigma}_j^x \hat{\sigma}_{j+r}^x}, \quad (4.4)$$

with the instantaneous kick operator,

$$K_\psi = \prod_{j=1}^N e^{-i\psi \hat{\sigma}_j^z}. \quad (4.5)$$

The resulting evolution operator for a single step of the Floquet protocol is

$$U_F = K_\psi V. \quad (4.6)$$

The system is initialized at $t = 0$ in the fully polarized state with positive magnetization along the \hat{z} direction: $|\psi(0)\rangle = |\dots \uparrow\uparrow\uparrow \dots\rangle$, where $|\uparrow\rangle$ and $|\downarrow\rangle$ denote the eigenstates of the σ^x Pauli matrix with eigenvalues $+1$ and -1 , respectively. In the quantum simulation context, these eigenstates will correspond to the computational basis of the quantum processor, with the convention $|\uparrow\rangle = |0\rangle$ and $|\downarrow\rangle = |1\rangle$.

The simplest realization of time-crystalline spatiotemporal order is achieved by setting the kick operator K_ψ to rotate each spin by an angle π around the z -axis. In this scenario, the kick operator reads =

$$K_{\pi/2} = \prod_{j=1}^N e^{-i\frac{\pi}{2} \hat{\sigma}_j^z} = \prod_{j=1}^N \hat{\sigma}_j^z. \quad (4.7)$$

Consequently, the time-evolved state after n kicks, $|\psi(n)\rangle = U_F^n |\psi(0)\rangle$, shows a sequence of perfect transitions between the $|\dots \uparrow\uparrow\uparrow \dots\rangle$ and $|\dots \downarrow\downarrow\downarrow \dots\rangle$ states, resulting in a persistent non-vanishing order parameter in both space and time. The order parameter is given by

$$m_x(n) = \langle \psi(n) | \hat{\sigma}_j^x | \psi(n) \rangle = (-1)^n, \quad (4.8)$$

This represents the simplest example of a subharmonic response, where the period of the order parameter evolution is twice the period of the Floquet driving. However, this behavior relies on the finely tuned choice of the kick angle $2\psi = \pi$. To observe a proper discrete time-crystalline phase, the spatiotemporal order must remain stable under sufficiently weak perturbations of the Hamiltonian parameters, $\psi = \pi/2 + \epsilon$, in the thermodynamic limit $N \rightarrow \infty$.

4.3 The strong long-range regime

In this section, we focus on the truly long-range case where the system exhibits all-to-all connectivity, i.e., $R = N$. Our attention will be directed towards the strong long-range regime characterized by $0 < \alpha < d$, where stable DFTC phases can exist in the thermodynamic limit.

4.3.1 Mean-field DFTC

First, we consider the mean-field limit with $\alpha = 0$ and $N \rightarrow \infty$, focusing on the evolution of the components of the system's magnetization $m_\mu = \sum_j \langle \hat{\sigma}_j^\mu \rangle / N$, with $\mu = x, y, z$. Given the impulsive nature of the magnetic field $h(t)$ in Eq. (4.2), the Floquet propagator can be expressed as the product of two distinct operators:

$$U_F = e^{-2i\psi \hat{S}_z} e^{iJT \hat{S}_x^2 / N} , \quad (4.9)$$

where we utilize the global spin operators defined in Eq. (1.20). The kick term $e^{-2i\psi \hat{S}_z}$ in Eq. (4.9) acts on the observable $\mathbf{m} = (m_x, m_y, m_z)$ as a rotation around the z -axis. The other term describes the evolution over one period T of \mathbf{m} induced by the mean-field Ising Hamiltonian. The Heisenberg equations of motion corresponding to this evolution for the operators \hat{S}_a are:

$$\begin{cases} \frac{d}{dt} \hat{S}_x = 0 , \\ \frac{d}{dt} \hat{S}_y = \frac{J}{N} (\hat{S}_x \hat{S}_z + \hat{S}_z \hat{S}_x) , \\ \frac{d}{dt} \hat{S}_z = -\frac{J}{N} (\hat{S}_x \hat{S}_y + \hat{S}_y \hat{S}_x) . \end{cases} \quad (4.10)$$

Due to the mean-field nature of the problem, spin-spin correlations can be neglected in the thermodynamic limit $N \rightarrow \infty$ [214], meaning that $\langle \hat{S}_a \hat{S}_b \rangle \simeq \langle \hat{S}_a \rangle \langle \hat{S}_b \rangle$. Then, by averaging both sides of Eqs. (4.10), we derive a closed set of equations for the magnetization:

$$\begin{cases} \dot{m}_x = 0 , \\ \dot{m}_y = J m_x m_z , \\ \dot{m}_z = -J m_x m_y . \end{cases} \quad (4.11)$$

Consequently, after a time interval T , the vector \mathbf{m} undergoes a clockwise rotation around the x -axis by an angle of $JTm_x(t)$. The \mathbb{Z}_2 symmetry of the model is represented in the dynamical symmetry $\psi \rightarrow \psi + \pi/2$, $\mathbf{m}_n \rightarrow R_z(\pi n)\mathbf{m}_n$ in Eq. (4.11), where $R_\mu(\xi)$ denotes the rotation matrix for an angle ξ around the axis $\mu = x, y, z$. Therefore, with $J = 1$, the overall effect of the unitary Floquet evolution operator in (4.9) on the observable \mathbf{m} is described by the mean-field map [214]

$$\mathbf{m}_{n+1} = f(\mathbf{m}_n) \equiv R_z(2\psi)R_x(-m_{x,n}T)\mathbf{m}_n, \quad (4.12)$$

with $\mathbf{m}_0 = (1, 0, 0)$.

Given the periodic nature of the drive, the map in Eq. (4.12) exhibits a Hamiltonian structure, preserving the area of the region on the sphere $\mathbf{m}^2 = 1$ traced by the dynamics. Using polar coordinates along the z -axis $\mathbf{m} = (\sin \theta \cos \phi, \sin \theta \sin \phi, \cos \theta)$, the area element is expressed as $dS = d(\cos \theta)d\phi$. Consequently, the coordinates ϕ and $I = \cos \theta$ are natural canonical conjugate variables for the system. Following Ref. [214], the action I can be interpreted as the z -component of the angular momentum and ϕ as the rotation angle around the same axis.

Then, in the small period limit $T \rightarrow 0$ the map can be rewritten as

$$\begin{aligned} I_{n+1} &= I_n, \\ \phi_{n+1} &= \phi_n + 2\psi, \end{aligned} \quad (4.13)$$

with $I_0 = 0$, $\psi_0 = \pi/2$. This corresponds to the Poincaré map obtained by taking a stroboscopic section of the integrable dynamics. Essentially, the motion of the order parameter \mathbf{m}_n at vanishing drive periods is quasi-periodic with a period π/ψ . When the kicking period T is slightly increased, the map in Eq. (4.13) is perturbed, and the system's behavior follows the Kolmogorov–Arnold–Moser (KAM) theorem [215, 216, 217]. According to the theorem, small perturbations of the form in Eq. (4.2) only slightly deform the torus $I = \text{const}$, as long as the drive frequency is not resonant. Hence, the motion remains quasi-periodic for drive strengths ψ sufficiently far from rational multiples of π . However, when a resonance is approached and $\psi \approx \psi_r = r\pi$, where $r = q/p$ and p and q are coprime integers, pairs of elliptic and unstable fixed points emerge in the dynamics due to the Poincaré–Birkhoff theorem [218].

Then, distinct regions in the phase space (I, ϕ) can be identified based on the action of the p -iterated map $f^p(\mathbf{m})$, which also correspond to different evolutions of \mathbf{m}_n . Quasi-periodic behavior persists for initial conditions (I_0, ϕ_0) sufficiently distant from the fixed points, where rotation dynamics occur with ϕ periodically spanning the interval $[0, 2\pi]$. Conversely, when the initial conditions (I_0, ϕ_0) are near the fixed points, a libration dynamics arises, with ϕ oscillating around a finite value. As a result, successive map iterations do not significantly alter the magnetization value, with $\mathbf{m}_{n+p} \approx \mathbf{m}_n$, indicating a DFTC phase. Finally, the boundary between the DFTC and quasi-periodic regimes is occupied by chaotic regions, which expand and eventually dominate the regular regions at large T .

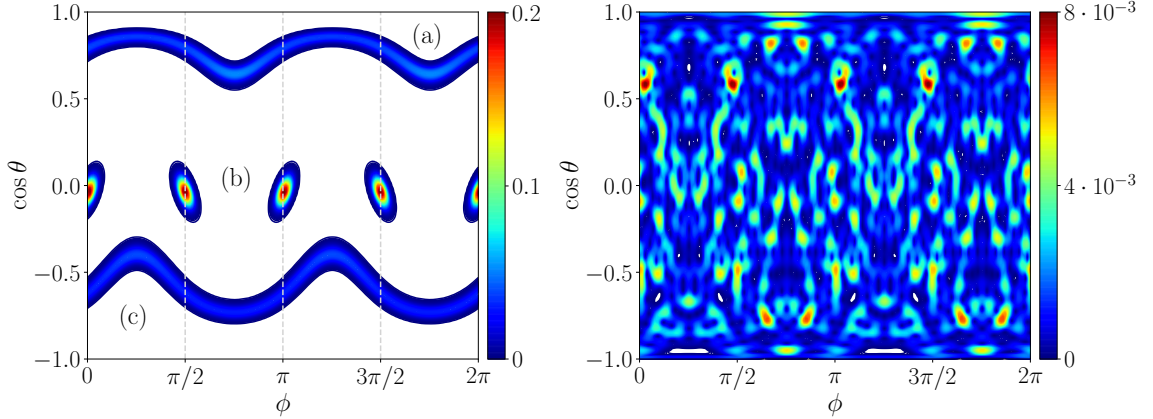


Figure 4.1: Color plot of the overlap $|\langle \Omega_{\theta,\psi} | \eta_m \rangle|^2$ between the spin coherent state $|\Omega_{\theta,\phi}\rangle$ and different Floquet eigenstates $|\eta_m\rangle$, corresponding to different phases, for $N = 800$, $\psi = \pi/2 + 0.01$, $T = 1$ (left) and $T = 10$ (right). While in the chaotic phase (right panel) the eigenstate has no structure, the eigenstate (b) (left panel), which correspond to the DFTC phase with $p = 4$, clearly exhibits the structure of a Bloch wave-function localized around the \mathbb{Z}_4 symmetric wells. The eigenstate (b) (left panel) has maximum overlap with the spin coherent state corresponding to the initial conditions $\cos \theta = 0$, $\psi = \pi/2$. Initial conditions localized around the eigenstates (a) and (c) (left panel) instead correspond to a quasi-periodic phase.

4.3.2 Finite-size and finite-range effects

The semiclassical analysis discussed above becomes exact in the thermodynamic limit, but it is also important to examine finite-size effects to validate the large- N picture. For finite N , the modulus of the total spin \hat{S} of the system is conserved, restricting the dynamics to the subspace of constant $\hat{S}^2 = S(S + 1)$, where $S = N/2$. This allows for relatively straightforward exact diagonalization up to large sizes ($N = 800$) [219, 205]. To visualize the eigenstates in this subspace, we introduce the spin coherent states [220]:

$$|\Omega(\theta, \phi)\rangle = e^{-i\mathbf{n}\cdot\mathbf{S}} |\uparrow\rangle, \quad (4.14)$$

where $|\uparrow\rangle$ is the eigenstate corresponding to the maximum projection of the spin along the z direction and $\mathbf{n} = (\sin \theta \cos \phi, \sin \theta \sin \phi, \cos \theta)$. The overlap between different coherent states at finite N is

$$|\langle \Omega(\theta, \phi) | \Omega(\theta + \Delta\theta, \phi + \Delta\phi) \rangle| = \left(\sin \frac{\Delta\theta}{2} e^{-i\Delta\phi} \right)^{2S}, \quad (4.15)$$

which vanishes in the $N \rightarrow \infty$ limit due to the exponent S . However, for any finite N , the states in Eq. (4.14) form an overcomplete basis for the Hilbert space. The dynamics

can then be characterized by estimating the projection $|\langle \Omega(\theta, \phi) | \eta_m \rangle|^2$ for various Floquet eigenstates $|\eta_m\rangle$, i.e., eigenstates of the unitary Floquet operator (4.9).

Examples of overlaps $|\langle \Omega(\theta, \phi) | \eta_m \rangle|^2$ for different eigenstates $|\eta_m\rangle$ are plotted in Fig. 4.1 as a function of ϕ and $\cos\theta$. In the $p = 4$ DFTC phase, the Floquet eigenstates are clearly localized around four \mathbb{Z}_4 symmetric points (Fig. 4.1, left panel, curve (b)), whereas this localization is absent in the quasi-periodic phase (left panel, curves (a) and (c) in Fig. 4.1). In the chaotic phase, no recognizable pattern emerges (right panel of Fig. 4.1). This behavior can be explained semi-classically: near a resonance, the Floquet evolution resembles hopping between p adjacent wells in the classical phase space, causing the Floquet eigenstates to form a superposition of tight-binding Bloch wavefunctions:

$$\langle \Omega(\theta, \phi) | \eta_m \rangle = \sum_{k=0}^{p-1} e^{2i\pi k/p} W_m(I, \phi - k\psi_r), \quad (4.16)$$

where $W_m(I, \phi - k\psi_r)$ are wavefunctions connected by the Floquet propagator:

$$U_F W_m(I, \phi - k\psi_r) = e^{i\beta_m} W_m(I, \phi - (k+1)\psi_r). \quad (4.17)$$

Notably, given the initial conditions chosen in this study, in the $N \rightarrow \infty$ limit, the only eigenstate contributing to the dynamics will be the one with a non-zero overlap with the point $\theta = 0, \phi = 0$, which can correspond to each of the three phases.

The inclusion of quantum fluctuations due to a finite value of α or additional local couplings does not significantly alter the overall picture. Indeed, The structure of the low- T DFTC region with $p = 2$ generally remains robust against quantum fluctuations. On the other hand, sufficiently high values of α enhance the chaotic phase, leading to the disruption of the DFTC phases with $p > 2$ for large enough values of the drive period T , see Fig. 4.2(b).

4.3.3 The order parameter

The dynamical phase diagram of various high-order DFTC phases reveals intricate self-similar and fractal structures, where regular phases are intertwined with chaotic and quasi-periodic regions. To capture these properties and achieve a comprehensive characterization of DFTC phases, irrespective of their order, we introduce a novel order parameter ζ . The key is to consider different values of the kick amplitude, $\psi, \psi + \delta\psi$, corresponding to two nearby initial conditions in the phase space. Then, the order parameter is defined as

$$\zeta^2 = \frac{1}{n_{\max}} \sum_{n=0}^{n_{\max}} (m_{x,n}(\psi + \delta\psi) - m_{x,n}(\psi))^2 \quad (4.18)$$

In both the DFTC and quasi-periodic phases, the evolution is not chaotic, causing the two trajectories to diverge polynomially over time. As a consequence expanding Eq. (4.18)

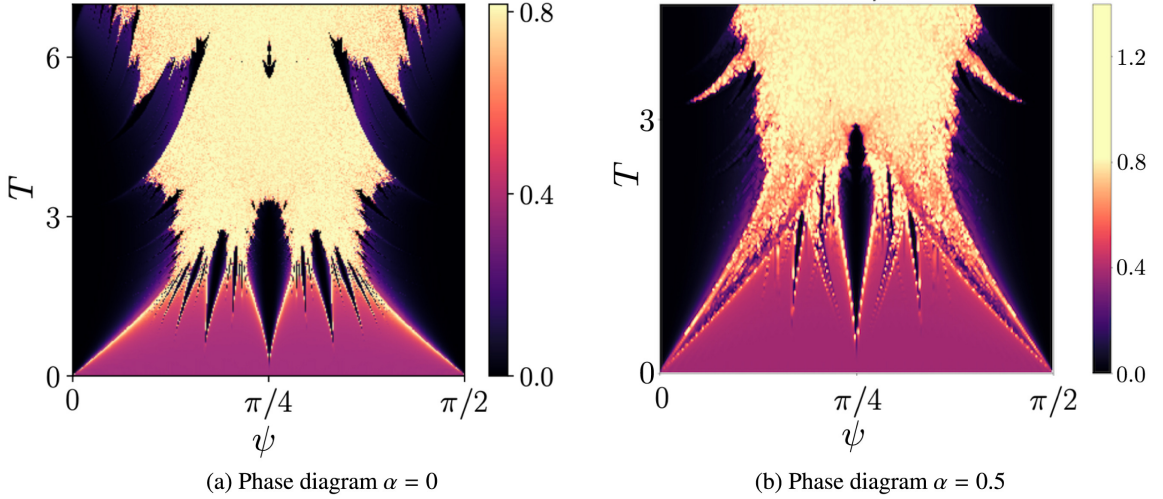


Figure 4.2: Panel (a): Color plot of the order parameter ζ as a function of the kick amplitude ψ and the period of the drive T , saturated at the value $\zeta = \sqrt{2/3}$, with $n_{\max} = 300$ and $\delta\psi = 1.6 \cdot 10^{-3}$, for the mean field case with $\alpha = 0$ and $N \rightarrow \infty$. Panel (b): same as (a) but for $\alpha = 0.5$.

for small deviations $\delta\psi$ yields

$$\zeta^2 \sim \frac{\ell}{n_{\max}} \sum_{n=0}^{n_{\max}} \delta\psi^2 n^2 \sim \ell(\delta\psi n_{\max})^2, \quad (4.19)$$

where ℓ depends on the the average distance between two randomly chosen points of the two nearby trajectories. The value ζ in these phases is not universal as it depends on the value of $(n_{\max}\delta\psi)$. Accordingly, the value of n_{\max} must be sufficiently large so that the rightmost term in Eq. (4.19) remains $\mathcal{O}(1)$, i.e., $n_{\max} \rightarrow \infty$ as $\delta\psi \rightarrow 0$. However, the value of ℓ undergoes a discontinuous jump between the libration regime (corresponding to a DFTC phase) and the rotation one (corresponding to a quasi-periodic phase). Indeed, close to the fixed point of the iterated map the micro-motion becomes negligible and $\zeta \rightarrow 0$, signaling the emergence of the pure time-crystalline regime. This discontinuity in ℓ leads to a discontinuity in ζ , which may be observed in the numerical distribution of ζ as shown in the occurrence histogram in Fig. 4.3. Indeed, in the DFTC phase, the order parameter distribution peaks sharply around $\zeta = 0$, but becomes negligible for $\zeta \gtrsim 0.2$. The quasi-periodic phase is indicated by a peak at $\zeta \sim 0.36$, disconnected from the DFTC peak at $\zeta = 0$.

On the other hand, in the chaotic phase, trajectories diverge exponentially, losing the memory of the initial condition after a time-scale $n_{\max} \sim -\log(\delta\psi)$. In this scenario, $m_{x,n}(\psi)$ and $m_{x,n}(\psi + \delta\psi)$ can be assumed to be drawn from a set of equally distributed

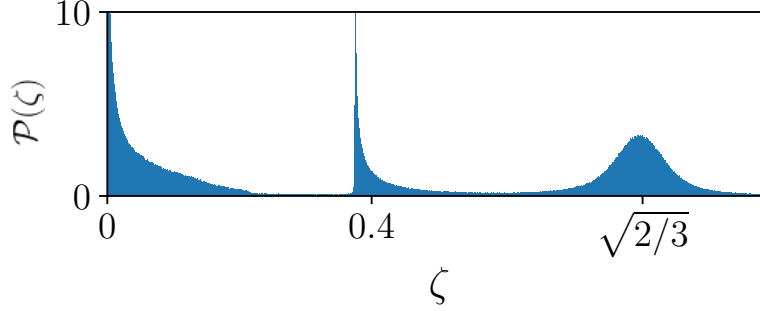


Figure 4.3: Histogram of the occurrence $\mathcal{P}(\zeta)$ of the values of ζ within the parameter region of Fig. 4.2, normalized to one. The gap between the DFTC phase, $\zeta \lesssim 0.2$ (and peaked around $\zeta = 0$), and the quasi-periodic one, $\zeta \gtrsim 0.36$, is apparent. On the right, the profile of the Gaussian distribution around $\zeta = \sqrt{2/3}$, characteristic of the chaotic phase.

random variables with zero mean. Consequently, according to the central limit theorem, ζ^2 is distributed as a Gaussian around the mean value

$$\langle \zeta^2 \rangle = 2 \langle m_x^2 \rangle \quad (4.20)$$

with a variance $\mathcal{O}(n_{\max}^{-1})$. For an isotropic system one can easily derive the peak value for the distribution, since $|\mathbf{m}|^2 = 1$, we have

$$\langle m_x^2 \rangle = \frac{1}{3} \langle |\mathbf{m}^2| \rangle = \frac{1}{3}, \quad (4.21)$$

so that $\langle \zeta^2 \rangle = 2/3$. The corresponding Gaussian peak centered around $\zeta = \sqrt{2/3}$ is evident in the histogram in Fig.(4.3).

Thus, the order parameter ζ can be used to detect higher-order DFTC phases in clean long-range systems, leveraging the connection between DFTCs and the Poincaré–Birkhoff theorem [218], which holds rigorously in the mean-field limit. The phase diagram obtained through numerical characterization of the order parameter (see Fig. 4.2) reproduces and expands upon the known properties of the DFTC phases in the thermodynamic limit [205, 212].

The symmetry of the phase diagram around the $\psi = \pi/4$ axis arises from the dynamical \mathbb{Z}_2 symmetry, a notable feature that would remain undetectable with a p -dependent order parameter. At low values of T , the quasi-periodic phase dominates (pink area $\zeta \approx 0.4$), while small islands of the DFTC phases emerge around specific values of ψ , corresponding to rational multiples of π (black areas $\zeta \approx 0$). Initially, the size of these islands increases with increasing T and, as they approach each other, chaos emerges along their boundaries (yellow area $\zeta \approx \sqrt{2/3}$). Ultimately, all islands associated with DFTC of order $p > 2$ are engulfed by the chaotic phase, with the largest (central) one corresponding to $p = 4$

surviving the longest. Interestingly, at certain values of the driving period, we observe a revival of the higher-order DFTC phases, particularly pronounced for $p = 4$ (small, arrow shaped, black area at high T for in Fig. 4.2(a)).

The boundary between the chaotic and DFTC phases is not smooth; instead, it exhibits self-similar patterns that repeat at increasingly smaller scales. The emergence of this fractal scaling in the boundaries of time-crystalline phases draws a direct analogy with similar phenomena in traditional critical systems, such as percolation, self-avoiding random walks, and the Potts model [221, 222], where a rigorous connection between conformal invariance and stochastic evolution has been established [223, 224]. Moreover, as noted in Ref. [209], the formation of DFTC islands can be understood within the framework of area-preserving maps [225], specifically linked to the existence of Arnold tongues [226, 227].

4.4 Quantum simulation with tunable interaction range

Thanks to the flexibility of modern quantum processors, the number of quantum simulations implemented on noisy superconducting devices has steadily risen in recent years. The remote accessibility of these machines has facilitated the benchmarking of numerous phenomena that were previously unconfirmed or scarcely experimentally corroborated [228, 229, 230, 231, 232, 233, 12, 11, 8]. On the other hand, the performance of superconducting NISQ devices is limited by the presence of various sources of noise and decoherence. The impact of these factors grows with the depth and complexity of the quantum circuit realized, which restricts the investigation of non-local effects and complex geometries. One primary limitation of superconducting NISQ devices is their extremely limited connectivity. Superconducting qubits are typically arranged in a one- or two-dimensional grid with nearest-neighbor connectivity, making it challenging to implement quantum algorithms that require long-range interactions [133].

In this section, we investigate the possibility of reproducing the dynamics of systems with couplings beyond nearest neighbors on superconducting quantum hardware. To achieve this, we utilize the universality of the quantum processor native gates to implement couplings among physically unconnected qubits. While the depth of the resulting quantum circuit increases with the effective range of the interaction, we show that careful consideration of gate noise, measurement errors, and statistical errors enables the removal of their effects from the raw results. Therefore our quantum simulation addresses one of the significant limitations of superconducting quantum processors, namely, device connectivity. It reveals that non-trivial physics involving couplings beyond nearest neighbors can be extracted after the impact of noise is properly taken into account in the theoretical model and consequently mitigated from the experimental data.

4.4.1 Stabilization of the DFTC response by increasing the interaction range

Due to the limited connectivity of IBM superconducting devices, it is not feasible to implement the dynamics of a truly fully connected system as described in Section 4.3. Therefore, we are not able to observe the DFTC phase stabilized by strong long-range interactions. Nonetheless, we can perform the quantum simulation of the kicked quantum Ising chain in Eq. (4.3), with a finite and, in principle, tunable interaction range R . The quantum circuit structure utilized by IBM quantum computers is well-suited for implementing discrete Floquet driving protocols [234], making it a natural choice for such applications [229].

Our focus is on the stabilization of discrete DFTC response as the interaction range increases. Indeed, for any finite R and in the absence of disorder, the system magnetization exhibits an exponential decay with the number of Floquet steps n :

$$m_x(n) \propto (-1)^n e^{-n\gamma_{\epsilon,R}}. \quad (4.22)$$

However, since for kick amplitude $\psi = \pi/2$ the magnetization has a trivial period doubling, then the decay rate $\gamma_{\epsilon,R}$ approaches zero as the perfect kick case is approached, i.e., for $\epsilon \rightarrow 0$. Moreover, as shown in Ref. [210], $\gamma_{\epsilon,R}$ is deeply affected by the interaction range. In the small ϵ limit, we have that

$$\gamma_{\epsilon,R} \approx \epsilon^{2R+1}. \quad (4.23)$$

Therefore, increasing the interaction range exponentially enhances the order parameter lifetime. This difference in decay rate should already be apparent when comparing the nearest-neighbor $R = 1$ and the next-to-nearest neighbor $R = 2$ cases.

The scope of our quantum simulation is to validate this phenomenon, which heavily depends on the interaction range, using a nearest-neighbor connected superconducting quantum processor.

4.4.2 Quantum circuit implementation of the Floquet dynamics

Specifically, in our quantum simulation we utilize the *ibmq-mumbai* 27-qubit processor, whose topology is depicted in Fig. 4.4(a). Our quantum circuit is optimized using the available connectivity and native gates of the device, including the controlled-NOT gate (CNOT), the identity gate ID, rotations along the z axis R_Z , the NOT gate X , and the $\text{SX} = \sqrt{X}$ gate.

The Floquet unitary evolution operator at stroboscopic times $t = nT$ can be obtained by applying the unitary operator corresponding to each Floquet step U_F , n times, i.e., $U(nT) = (U_F)^n$. Importantly, no Trotter approximation is required, which is a significant advantage of discrete Floquet drivings [234]. The kicked Floquet protocol of interest can be further decomposed into the successive application of the kick operator K_ψ and the Ising evolution operator V (see Eq. (4.6)). The former can be expressed in terms of single-qubit

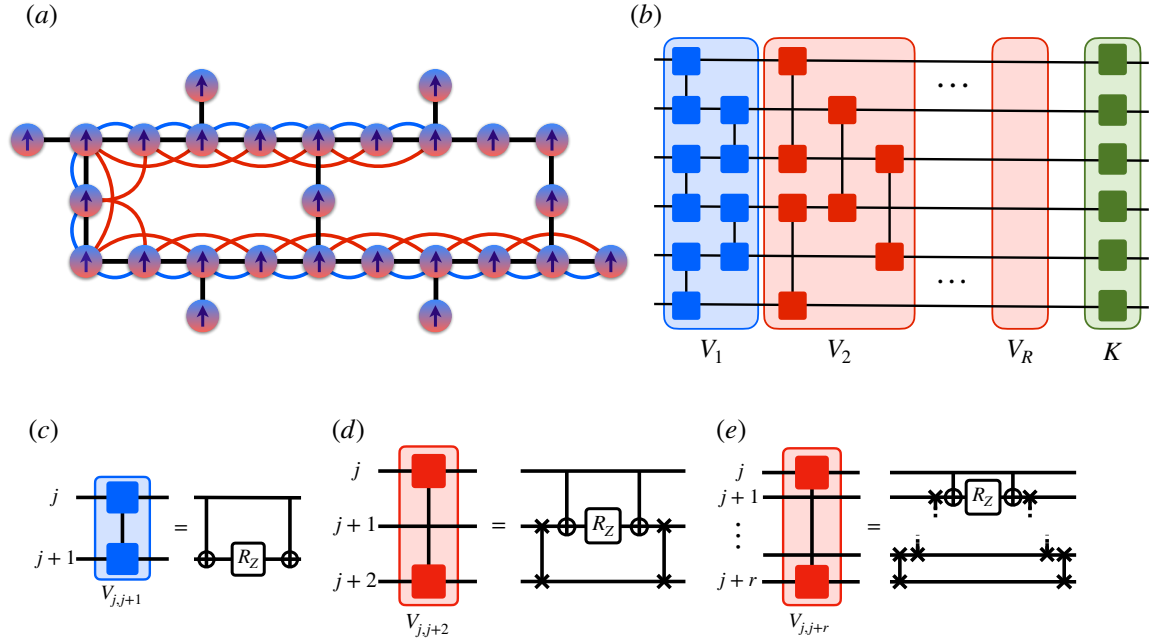


Figure 4.4: Quantum circuit implementation of Floquet dynamics with varying interaction range. (a) Topology of the *ibmq_mumbai* quantum processor. Black links represents the physical connections among the qubits on the quantum hardware, blue and red links represent the nearest neighbors $R = 1$ and next-to-nearest neighbor $R = 2$ Ising interactions we effectively implemented among physically unconnected qubits during our quantum simulation. (b) Quantum circuit implementing a single Floquet step for a kicked Ising model with R range interactions. (c) Quantum gate implementation of nearest-neighbor Ising interaction among qubit j and $j + 1$. (d) Quantum gate implementation of next-to-nearest neighbor Ising interaction among qubit j and $j + 2$. (e) Quantum gate implementation of r -neighbor Ising interaction among qubit j and $j + r$.

gates, corresponding to local rotations along the x -axis, and the latter can be written as a product of mutually commuting unitaries that connect pairs of qubits at progressively larger distances as the interaction range is increased, i.e., $K_\psi = \prod_{i=1}^N R_{X,i}(2\psi)$ and $V = \prod_{r=1}^R V_r$, respectively.

The quantum circuit corresponding to a single Floquet step is shown in Fig. 4.4(b), where blue gates represent nearest-neighbor Ising interactions $V_{j,j+1}$, red gates represent Ising interactions beyond nearest neighbors $V_{j,j+r}$, and green gates represent the final kick rotation K_ψ applied equally to each qubit. As shown in Fig. 4.4(c), the unitary operator associated with nearest-neighbor Ising interactions can be decomposed in terms of the elementary gates as

$$\begin{aligned} V_{j,j+1} &= e^{iTJ_1Z_jZ_{j+1}} \\ &= \text{CNOT}_{j,j+1}R_Z(2J_1T)\text{CNOT}_{j,j+1}. \end{aligned} \quad (4.24)$$

On the other hand, the limited processor connectivity does not allow for a simple decomposition of r -range Ising interactions. The idea to overcome this limitation is to exchange the qubit states by applying a sequence of SWAP gates among the couples of physically connected qubits that lie between j and $j+r$. By doing so, the initial state of qubit q_{j+r} is effectively encoded in qubit q_{j+1} . Specifically, we achieve this by applying the gate sequence

$$S_r = \prod_{l=1}^{r-1} \text{SWAP}_{j+l,j+l+1}. \quad (4.25)$$

Next, we apply $V_{j,j+1}$ on the two connected qubits q_{j+1} and q_j . Finally, we need to bring back the state encoded in qubit q_{j+1} to the r -neighbor qubit q_{j+r} . This is achieved by applying the inverse sequence of SWAP gates S_r^\dagger . Summarizing, we obtain the quantum circuit identity shown in Fig. 4.4(e), reading

$$\begin{aligned} V_{j,j+r} &= S_r^\dagger V_{j,j+1} S_r \\ &= S_r^\dagger \text{CNOT}_{j,j+1} R_Z(2J_1T) \text{CNOT}_{j,j+1} S_r. \end{aligned} \quad (4.26)$$

This allows us to realize the desired tunable-range interactions among physically unconnected qubits. However, there is a trade-off: implementing these interactions requires inserting $2(r-1)$ additional SWAP gates into the quantum circuit. Since each two-qubit gate typically introduces noise, it is crucial to optimize our quantum circuit for each Floquet step of the dynamics (as depicted in Fig. 4.4(b)).

Moreover, we need to mitigate the effects of noise as the interaction range increases. These issues are addressed in the following sections.

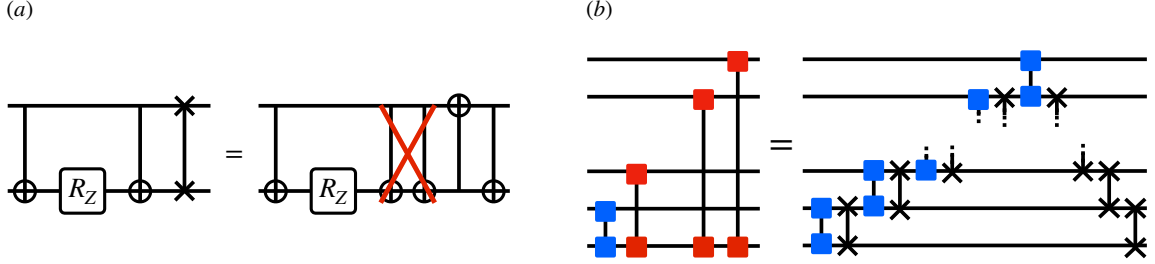


Figure 4.5: Quantum circuit optimization techniques using circuit identities. (a) Cancellation of CNOT gates in adjacent $V_{j,j+1}$ and SWAP gates. (b) Rearrangement of the quantum circuit to implement Ising interactions with $r = 1, \dots, R$ ranges while maximizing the number of adjacent $V_{j,j+1}$ and SWAP gates.

4.4.3 Quantum circuit optimization

Optimizing the number of operations in the quantum circuit for implementing Floquet dynamics is crucial, as each additional quantum gate increases noise, leading to rapid magnetization decay. Since two-qubit gates are particularly error-prone, we focus on reducing their number in our circuits.

First, we estimate the number of operations needed to implement the quantum circuit shown in Fig. 4.4(b) using the native gates of the *ibmq_mumbai* processor, without any optimization.

Regarding single-qubit gates, only the rotations around the X axis, corresponding to the Floquet driving kicks, need to be decomposed into native gates. This can be done efficiently as follows

$$R_X(\psi) = R_Z(\pi/2)\sqrt{X}R_Z(\psi)\sqrt{X}R_Z(5\pi/2). \quad (4.27)$$

Thus, each kick requires five additional single-qubit gates, resulting in a total of $Q_{1q,R} = 2R + 5$ gates. The only native two-qubit gate available is the CNOT gate. To estimate $Q_{2q,R}$, we count the number of CNOT gates involved in the hardware implementation of each Floquet step. As shown in Fig. 4.4(c), each nearest-neighbor Ising interaction is implemented using two CNOT gates. Additionally, each SWAP gate is realized using three CNOT gates, as it can be decomposed as

$$\text{SWAP}_{j,j+1} = \text{CNOT}_{j,j+1}\text{CNOT}_{j+1,j}\text{CNOT}_{j,j+1}. \quad (4.28)$$

Moreover, each r -range interaction is implemented by adding $2(r-1)$ SWAP gates to the nearest-neighbor interaction. Therefore, each r -range interaction gate requires $2 + 6(r-1)$ CNOT gates for implementation. For interactions with ranges $r = 1, \dots, R$, the longest path, determining the circuit depth, contains r non-parallelizable copies of each r -range

operation for $r > 1$ and two copies for $r = 1$. Summing up all the contributions, we obtain

$$Q_{2q,R} = \sum_{r>1}^R (2 + 6r(r-1)) + 4 = 2R^3 + 2. \quad (4.29)$$

Notably, as shown in Fig. 4.5(a), each time we have a sequence $V_{j,j+1}\text{SWAP}_{j,j+l}$, we can use the fact that $\text{CNOT}^2 = \mathbb{I}$ to eliminate two adjacent CNOT gates. To systematically exploit this, we rearrange our quantum circuit using the circuit identity in Fig. 4.5(b). Here, we utilize the properties $[V_{j,j+l}, V_{j,j+r}] = 0$ for all l, r , and $[V_{j,j+1}, \text{SWAP}_{j,j+l}] = 0$ to maximize the number of adjacent $V_{j,j+1}\text{SWAP}_{j,j+l}$, thereby increasing the number of cancelable CNOT gates.

For a circuit implementing a sequence of Ising interactions of ranges $r = 1, \dots, R$, we can cancel up to $2(R-1)$ CNOT gates. The depth of each subcircuit of this form is then given by

$$2R + 6(R-1) - 2(R-1) = 6R - 4. \quad (4.30)$$

To realize a kicked Ising model with interaction range up to R in a chain of N qubits, we divide the N qubits into subsets of size $2R$ that can be processed in parallel. To compute the circuit depth, which refers to the number of operations in the longest path, we focus on one subset at a time. Each subset contains R subcircuits with interaction ranges $r = 1, \dots, R$, following the form shown in Fig. 4.5(b). The depth of each of these subcircuits is $6R-4$. The remaining R subcircuits include interactions of range $r = 1, \dots, l$, where l varies from $l = 1$ to $l = R-1$, corresponding to a depth of $6l-4$ for each circuit. By summing up all the contributions, we obtain the optimized number of CNOT gates as

$$\begin{aligned} Q_{2q,R} &= R(6R-4) + \sum_{l=1}^{R-1} (6l-4) \\ &= 9R^2 - 11R + 4. \end{aligned} \quad (4.31)$$

Finally, we observe that the last sequence of SWAP gates in the circuit shown in Fig. 4.5(b) is only necessary if we need to apply different gates on different qubits afterward. If this is not the case, we can simply substitute the SWAP gates with a relabeling of the qubit numbers, which must be taken into account when reading the final measurement outcomes. This allows us to eliminate $(R-1)$ SWAP gates and $3(R-1)$ CNOT gates in the last subcircuit of this form. Therefore, we obtain

$$Q_{2q,R} = 9R^2 - 14R + 7. \quad (4.32)$$

As a final remark, for large values of maximum range R and hence large circuit complexity, additional simplifications may be possible by using optimized relabelings of the

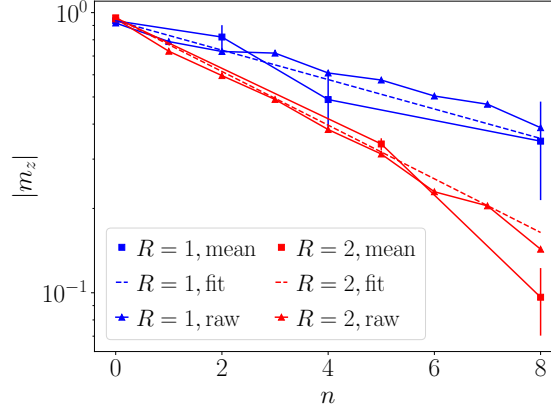


Figure 4.6: Modulus of the magnetization $|m_z|$ as a function of the stroboscopic times n for nearest neighbor $R = 1$ (blue points) and next-to-nearest neighbor $R = 2$ (red points) Ising interactions. Triangles represent the raw experimental data measured on our quantum simulation of the *ibmq_mumbai* quantum processor, which involves $N = 18$ qubits undergoing a kicked Ising dynamics with kick angle $\psi = \pi/2 + \epsilon$ with $\epsilon = 0.2$. Square points and the corresponding error bars represent the estimators for the average magnetization and its statistical error $\mathbb{E}(m_z) \pm 2\sigma(m_z)$, obtained through statistical bootstrapping. Dashed lines represent the best fit of the data with an exponential decay.

qubit numbers during the evolution, which can increase the number of parallelizable operations. However, such optimization is circuit and range dependent and can only be carried out numerically or in an approximate manner. For the case of $R = 2$ considered in our quantum simulation, we can claim that our circuit is optimal with respect to the number of CNOT gates involved.

4.4.4 The role of noise and statistical errors

The analysis of the raw experimental data clearly shows that the decay of magnetization is primarily driven by noise, as illustrated in Fig. 4.6. This figure presents the absolute value of the average magnetization $|m_z|$ over stroboscopic time n for nearest-neighbor ($R = 1$, in blue) and next-to-nearest-neighbor ($R = 2$, in red) interactions. The raw experimental data (triangles in Fig. 4.6) were obtained by running multiple repetitions of the quantum circuit corresponding to a single Floquet step U_F , as shown in Fig. 4.4(b), on the *ibmq_mumbai* quantum processor using $N = 18$ qubits.

At the end of each quantum evolution, a projective measurement of each qubit in the Z basis was performed. To collect sufficient statistics, the experiments for each value of n and R were repeated with a sample size $\mathcal{N} = 2^{13}$, allowing us to compute the sample average $\langle Z_i \rangle$ over the measurement outcomes. The spatial average of the magnetization

over different sites of the processor was then computed as

$$m_z = \frac{1}{N} \sum_{i=1}^N \langle Z_i \rangle, \quad (4.33)$$

where $N = 18$ in our case.

In an ideal scenario, we would estimate the statistical error by repeating the quantum experiments multiple times to obtain a comprehensive understanding of the "true" magnetization distribution to evaluate the sample mean $\mathbb{E}(m_z)$ and standard deviation $\sigma(m_z)$. However, this approach is impractical due to the significant time required for each magnetization estimate. Instead, we conduct the experiment only once and generate re-sampled measurement data from the empirical distribution using bootstrapping, a widely used statistical technique. This method makes the statistical analysis very convenient, and it is then becoming a common practice to estimate the statistical errors in digital quantum simulations [235].

Let us assume we perform an \mathcal{N} -shot quantum experiment and obtain a collection of \mathcal{N} outcomes. Each measurement outcome is represented as a string of 0s and 1s, denoted as $Z_{1,a} \dots Z_{N,a}$, where $Z_i = 0, 1$, N is the number of measured qubits, and the index a labels the different outcomes ($a = 1, \dots, \mathcal{N}$). The magnetization associated with each string can be computed by averaging over the qubits as follows:

$$m_{z,a} = \frac{1}{N} \sum_{i=1}^N Z_{i,a}. \quad (4.34)$$

This gives us the set of magnetization values $m_{z,a}$ with $a = 1, \dots, \mathcal{N}$. We define the empirical magnetization distribution $P_1(m_{z,a})$ as the histogram of the $m_{z,a}$ set. The average over this empirical distribution, denoted as m_z , corresponds to the experimentally obtained quantum expectation value on the final state of the system and can be expressed as

$$m_z = \frac{1}{N} \sum_{i=1}^N \langle Z_i \rangle = \sum_{a=1}^{\mathcal{N}} P_1(m_{z,a}) m_{z,a}. \quad (4.35)$$

The bootstrapping approach involves resampling from the empirical measurement distribution $P_1(m_{z,a})$. We sample elements from the set $m_{z,a}$ (or, equivalently, from the set of strings $\{Z_{1,a} \dots Z_{N,a}\}$) \mathcal{N} times to create a new set of measurement outcomes, and from this, a new empirical distribution $P_2(m_{z,a})$. We repeat this process as many times as possible given the available computational resources, say M repetitions, to obtain a set of distributions P_1, P_2, \dots, P_M . From each of these distributions, we can compute the average m_z^b with $b = 1, \dots, M$, and from the histogram of the set of averages, we obtain their distribution $\Pi(m_z^b)$. Since each resampling is independent, the distribution of averages should tend to a Gaussian in the large M limit, according to the central limit theorem.

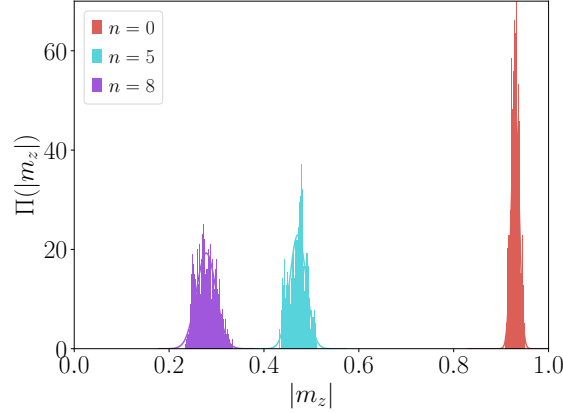


Figure 4.7: Bootstrap distribution of averages obtained by resampling $M = 1000$ times the measured data of three quantum simulations with range $R = 1$, noise scale $s = 1.4$, and different numbers of Floquet steps $n = 0, 5, 8$. The number of bins considered in each histogram is 100.

Accordingly, we can define our estimator for m_z and its statistical error as the average of the $\Pi(m_z^b)$ distribution,

$$\mathbb{E}(m_z) = \sum_{b=1}^M \Pi(m_z^b) m_z^b, \quad (4.36)$$

and its standard deviation,

$$\sigma(m_z) = \sqrt{\sum_{b=1}^M \Pi(m_z^b) (m_z^b - \mathbb{E}(m_z))^2}. \quad (4.37)$$

This method enables us to obtain error bars in Figs. 4.6 and 4.8 as $\mathbb{E}(m_z) \pm 2\sigma(m_z)$. Figure 4.7 shows, as an example, the distributions $\Pi(m_z^b)$ obtained through $M = 1000$ resamples of the measured data of three quantum simulations with range $R = 1$, noise scale $s = 1.4$, and number of Floquet steps $n = 0, 5, 8$, respectively. These are compared with Gaussian distributions with the same mean and standard deviation, finding good agreement. We notice that, as expected, the mean $\mathbb{E}(m_z)$ is smaller for a larger number of Floquet steps n , signaling the magnetization exponential decay. Moreover, distributions at later stroboscopic times become broader, signaling the growth of the statistical error due to the fact that we are trying to sample a quantity which is exponentially decaying with n .

The results for the statistical averages $\mathbb{E}(m_z(n))$ are represented by squares in Fig. 4.6, while two standard deviations, $2\sigma(m_z(n))$, serve as statistical errors and are depicted as error bars in the plots. Notably, we observe that the statistical error increases with

the number of Floquet steps involved in the dynamics n . This can be explained by a simple statistical argument: we are sampling a quantity, the modulus of the magnetization $|m_z|$, which exponentially decreases with n . Consequently, the resolution with which we can estimate this quantity deteriorates as m_z approaches the value $m_z \sim e^{-\gamma n} \sim 1/\sqrt{\mathcal{N}}$, i.e., the statistical uncertainty due to the finite sample size increases as we approach the stroboscopic time $n \sim (1/2\gamma) \ln \mathcal{N}$.

The decay of magnetization with stroboscopic time n can be described by an exponential fit $|\mathbb{E}(m_z(n))| = ae^{-bn}$, obtained using a weighted least squares regression method. This method accounts for points with high statistical uncertainty by penalizing them in the extrapolation. The resulting exponential decay is depicted as a dashed line in Fig. 4.6, showing a rapid decline with increasing n . Notably, the decay rate is more pronounced for next-to-nearest neighbor interactions ($R = 2$) compared to nearest neighbor interactions ($R = 1$). This discrepancy can be attributed to the fact that the quantum circuit implementing next-to-nearest neighbor interactions involves more gates, leading to larger noise effects.

4.4.5 Noise mitigation and final results

In order to effectively simulate the desired physical phenomena, it is therefore crucial to account for and mitigate the detrimental effects of noise. Real-world quantum hardware is susceptible to various sources of errors, such as noisy gates, environmental decoherence, and spurious time dependence of circuit parameters. To explicitly model these errors, a common approach is to consider one- and two-qubit depolarizing channels that act on the system's state ρ . Specifically, after each single-qubit gate acting on qubit i , the single-qubit channel Φ_i^{1q} is applied, while after each two-qubit gate on bond (i, j) , the two-qubit channel $\Phi_{i,j}^{2q}$ is applied. These channels are defined as [236, 234]

$$\Phi_i^{1q}(\rho) = (1 - p_1)\rho + \frac{p_1}{3}(X_i\rho X_i + Y_i\rho Y_i + Z_i\rho Z_i) \quad (4.38)$$

$$\Phi_{i,j}^{2q}(\rho) = (1 - p_2)\rho + \frac{p_2}{15} \sum_{\alpha,\beta=1}^3 (\sigma_{\alpha,i}\sigma_{\beta,j}\rho\sigma_{\alpha,i}\sigma_{\beta,j}), \quad (4.39)$$

where $\sigma_{1,i} = X_i$, $\sigma_{2,i} = Y_i$, and $\sigma_{3,i} = Z_i$ are the Pauli matrices for qubit i , and $\sigma_{\alpha,i}$ and $\sigma_{\beta,j}$ are the corresponding matrices for qubits i and j , respectively. By studying the dynamics of the Z_i operators under these depolarizing channels, we can estimate the magnetization decay rate induced by the noisy gates.

To isolate the effect of noise, we consider the case of perfect kick dynamics with $\epsilon = 0$. Under this condition, Z_i is invariant under the two-qubit Ising interaction gates and simply acquires a minus sign under the π rotation around the x -axis. However, after each two-qubit gate, Z_i decays under $\Phi_{i,j}^{2q}$ as

$$\Phi_{i,j}^{2q}(Z_i) = (1 - 16p_2/15)Z_i, \quad (4.40)$$

and after each single-qubit gate as

$$\Phi_i^{1q}(Z_i) = (1 - 4p_1/3)Z_i. \quad (4.41)$$

Overall, Z_i decays to $-e^{-\gamma_{\text{dep}}}Z_i$, over one noisy Floquet step with perfect kicks, with γ_{dep} given by

$$\gamma_{\text{dep},R} = -\ln[(1 - 16p_2/15)^{\mathcal{Q}_{2q,R}}(1 - 4p_1/3)^{\mathcal{Q}_{1q,R}}], \quad (4.42)$$

where $\mathcal{Q}_{2q,R}$ and $\mathcal{Q}_{1q,R}$ are the number of two-qubit and single-qubit gates involved in a Floquet step quantum circuit with R -neighbor interactions. As shown in Sec. 4.4.3, for the specific case of the kicked Ising model considered in our quantum simulations, the quantum circuits corresponding to $R = 1, 2$ Floquet steps can be optimized, reducing the number of two-qubit native gates, involved in the quantum circuit longest path, to $\mathcal{Q}_{2q,R} = 9R^2 - 14R + 7$. In particular for $R = 1, 2$ we have

$$\mathcal{Q}_{2q,R} = \begin{cases} 4 & R = 1 \\ 15 & R = 2 \end{cases}, \quad \mathcal{Q}_{1q,R} = \begin{cases} 7 & R = 1 \\ 9 & R = 2 \end{cases}. \quad (4.43)$$

Another source of noise arises from the finite decoherence time T_1 of the qubits, which introduces an additional time scale contributing to the magnetization decay. Taking into account all the contributions, we can estimate the decay rate of magnetization for a Floquet step with imperfect kicks of an angle $\psi = \pi/2 + \epsilon$ to be approximately given by

$$\Gamma_{1,R} \approx \gamma_{\text{dep},R} + \tau_R/T_1 + \gamma_{\epsilon,R}, \quad (4.44)$$

where τ_R represents the time required to practically implement the Floquet step on the quantum hardware. This can be estimated as

$$\tau_R = \mathcal{Q}_{1q,R}\tau_{1q} + \mathcal{Q}_{2q,R}\tau_{2q} + \tau_m, \quad (4.45)$$

where τ_{1q} and τ_{2q} denote the time needed to execute each single-qubit and two-qubit gate, respectively, while τ_m represents the readout time required for measurements.

A third source of errors arises from readout errors, which can be modeled as a stochastic process where the outcome of a qubit-state measurement (in the Z computational basis) is randomly flipped with a probability of p_m away from its correct value [234]. Specifically, if we define the probability that qubit i points up (down) at time n as $\Pi_{\pm} = \langle (1 \pm Z_i(n))/2 \rangle$, then the result of the noisy measurement process is $Z_i = \pm 1$, with a probability of $\tilde{\Pi}_{\pm}^{(n)} = \Pi_{\pm}(1 - p_m) + \Pi_{\mp}p_m$. Accordingly, the estimate for the expectation value of Z_i becomes

$$\begin{aligned} \tilde{\Pi}_+ - \tilde{\Pi}_- &= (1 - 2p_m)(\Pi_+ - \Pi_-) \\ &= (1 - 2p_m)\langle Z_i(n) \rangle. \end{aligned} \quad (4.46)$$

Hence, averaging over positions yields $\tilde{m}_z = (1 - 2p_m)m_z$, i.e., a damping by a time-independent and range-independent overall prefactor $C_m = (1 - 2p_m)$.

The inclusion of noise in our model provides a compelling explanation for the rapid exponential decay of magnetization, as observed in Fig. 4.6. Moreover, by inserting the estimated values of the parameters p_1 , p_2 , τ , and T_1 , which were extracted from the calibration data provided by IBM, we find that the calculated decay rate is in good agreement with that obtained from fitting the experimental data with a stroboscopic time dependence of the form predicted by our theoretical model,

$$|m_z(n)| = C_m e^{-n\Gamma_{1,R}}. \quad (4.47)$$

This understanding of the noise effect justifies our exploration of the possibility of mitigating it through a technique called zero noise extrapolation (ZNE).

ZNE is a well-studied error mitigation method in the literature [77, 237, 238, 235]. It is a powerful technique that allows for the estimation of noiseless expectation values of observables from a series of measurements obtained at different levels of noise. The ZNE process involves two steps: intentional scaling of noise and extrapolation to the noiseless limit. In the first step, the target circuit is executed at varying error rates denoted by s , with expectation values estimated for the original circuit ($s = 1$) as well as circuits at increased error rates ($s > 1$). Then, in the second step, a function, motivated by physical arguments, is fitted to these expectation values and used to extrapolate to error rate $s = 0$, providing an error-mitigated estimate.

There are various methods to increase the error rate s . Examples in the literature include pulse stretching [77] or, at a gate level, unitary folding [237, 239]. In our implementation of ZNE, we increase s using a local unitary folding technique. This technique involves increasing the number of operations by applying a mapping $U \rightarrow UU^\dagger U$ to individual gates of the circuit. Specifically, the unitary gates to be folded are randomly chosen from the set of gates composing the circuit in such a way that the circuit depth is approximately increased by the desired factor s . This random selection helps to ensure that the circuit is exposed to a variety of gate sequences and interactions, allowing for a more comprehensive study of the circuit's behavior under different noise conditions. In our case, for each noise scale s , we extract the magnetization decay rate from the measured data. Our noise model then allows us to theoretically estimate the decay rate at noise scale s as

$$\Gamma_{s,R} \approx s(\gamma_{\text{dep},R} + \tau_R/T_1) + \gamma_{\epsilon,R}. \quad (4.48)$$

Accordingly, a linear fit of the measured decay rates with respect to the parameter s enables us to separate the contribution coming from the noise, $\gamma_{\text{noise}} = \gamma_{\text{dep},R} + \tau_R/T_1$, from $\gamma_{\epsilon,R}$, which represents the decay rate due to the internal system thermalization that destroys the time crystalline order at finite ϵ , and should be stabilized by the presence of longer-range interactions. More precisely, $\gamma_{\epsilon,R}$ is obtained as the zero noise extrapolation of the decay rate in (4.48), $\gamma_{\epsilon,R} \approx \Gamma_{s=0,R}$. The results of this procedure are shown in Fig. 4.8,

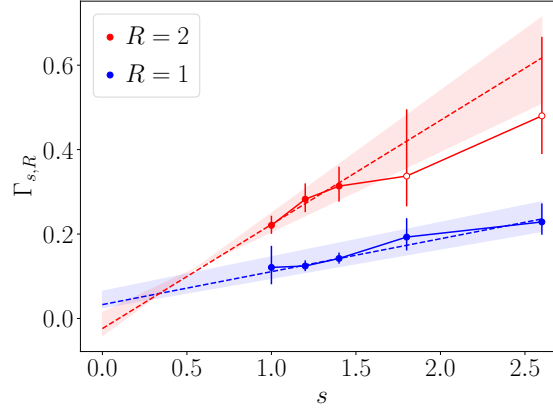


Figure 4.8: Decay rate of magnetization as a function of noise scale s for $R = 1$ (blue points) and $R = 2$ (red points). Error bars represent two standard deviations $\sigma(m_z)$ estimated through statistical bootstrapping. Dashed lines indicate the best linear fit obtained using weighted least squares regression. Empty points are excluded from the fitting data.

where the measured decay rate is plotted as a function of the noise scale s . To estimate $\Gamma_{s,R}$ and its uncertainty $\delta\Gamma_{s,R}$, we first estimate the magnetization as a function of the stroboscopic time n at different values of s and R from the measured data, along with the corresponding statistical uncertainty from the standard deviation obtained through the statistical bootstrap method, $\mathbb{E}(m_z) \pm 2\sigma(m_z)$. Then, the decay rate and its uncertainty are obtained through the exponential fit

$$|\mathbb{E}(m_z) \pm 2\sigma(m_z)| = (C_m \pm \delta C_m) e^{-n(\Gamma_{s,R} \pm \delta\Gamma_{s,R})}. \quad (4.49)$$

In particular, the exponential fit is performed using weighted least squares regression, and the last two points with $R = 2$ and $s > 1.5$ are excluded from the fitting data (empty points in Fig. 4.8). This exclusion is justified by the fact that the decay rate for these points falls within the range of $0.2 < \Gamma_{s>1.5} < 0.8$, and thus, the magnetization can be reliably estimated only for stroboscopic times $n < n^* \approx (1/2\gamma) \ln \mathcal{N}$, where $6 < n^* < 22$. Therefore, not all the time steps $1 < n < 16$ considered in the exponential fit of $m_z(n)$ from which we extracted this decay rate are within the reach of our statistical resolution. The difficulty of establishing a reliable bootstrap-estimated value confirms this phenomenon, as shown in Fig. 4.8, where the statistical error bars for these points are significantly larger than those for the other points, indicating the challenge of obtaining a trustworthy value for the magnetization in this regime. Despite the failure of the bootstrap procedure, we include these data as empty points in the plot for completeness, noting that the corresponding error bars are sufficiently large that the resulting fit is still compatible with these unreliable values within $\pm 2\sigma(m_z)$.

Remarkably, upon extrapolation to the zero noise limit, the decay rate of the $R = 2$ case is found to be smaller than that in the nearest neighbors case $R = 1$. Specifically, we obtain

$$\Gamma_{0,2} \pm \delta\Gamma_{0,2} < \Gamma_{0,1} \pm \delta\Gamma_{0,1}. \quad (4.50)$$

Most significantly, we find that the decay rate analytically predicted from the theoretical model, $\gamma_{\epsilon,R} \approx \epsilon^{2R+1}$, is compatible with the extrapolated values within the estimated uncertainty, i.e.,

$$\gamma_{\epsilon,R} \in [\Gamma_{0,R} - \delta\Gamma_{0,R}, \Gamma_{0,R} + \delta\Gamma_{0,R}], \quad (4.51)$$

indicating that the extrapolated decay rate is consistent with the theoretical expectations within the statistical uncertainty $\delta\Gamma_{0,R}$, which has been estimated by extrapolating $\delta\Gamma_{s,R}$ to $s = 0$.

4.5 Closing remarks

In the first part of this chapter, we introduced a novel order parameter ζ capable of unambiguously detecting higher-order Discrete Floquet Time-Crystals (DFTCs) in clean long-range systems. Using the kicked long-range Ising model as a paradigmatic example, we derived a new phase diagram featuring self-similar structures with non-integer, fractal dimensions. We quantitatively explained this phenomenon through an effective Hamiltonian map with renormalized couplings. While our theoretical picture becomes exact at $\alpha = 0$ and $N = \infty$, we verified its robustness for finite size and finite α .

In the second part of the chapter, we demonstrated the potential of superconducting quantum hardware for advancing digital quantum simulation by implementing quantum dynamics in systems with couplings beyond nearest neighbors. Leveraging the universality of native gates in quantum processors, we successfully implemented couplings among physically disconnected qubits and mitigated the effects of gate noise, measurement errors, and statistical errors from the raw results. Our focus was on stabilizing the discrete Floquet time-crystalline response as the interaction range is increased, which we implemented on IBM quantum superconducting processors.

Our quantum simulation has demonstrated the potential of IBM superconducting platforms for simulating quantum systems with couplings beyond nearest neighbors and has provided valuable insights into the fundamental physics of long-range systems. Our error mitigation approach effectively removed the effects of noise and measurement errors, and the mitigated data aligned well with theoretical expectations. This work opens new avenues for studying quantum systems with long-range interactions and paves the way for further advancements in digital quantum simulation on superconducting quantum hardware.

Chapter 5

Entanglement in long-range systems

5.1 Entanglement in many-body quantum systems

One of the most important features a system should have to be a good candidate for quantum technologies is the capability of hosting highly entangled states in its spectrum. Indeed, this crucial property is essential for performing tasks that are classically impossible or very inefficient [240]. More precisely, entanglement is the key factor that allows quantum computation to surpass classical computation, providing the computational speed-up in quantum algorithms compared to those based on classical physics processes [236]. Moreover, entanglement is crucial for many quantum technological applications such as quantum teleportation [241], quantum cryptography [181], and quantum metrology [182].

A set of key quantities for characterizing entanglement is provided by the entanglement Rényi entropies. To define these, one divides a given system into two subsystems A and B (the complement of A), determines the reduced density matrix of a subsystem (say, of A) ρ_A by tracing out the degrees of freedom of B , and then computes its Rényi entropies: $S_\nu = -\ln \text{Tr}[\rho_A^\nu]/(1 - \nu)$ [242]. One of the most fundamental properties of entanglement Rényi entropies is their behavior with the size of the subsystem considered. The celebrated area law [243, 244] states that entanglement typically grows with the boundary of the subsystem considered. For a system in d dimensions and a subsystem of size L having volume $\sim L^d$ and area $\sim L^{d-1}$, the entanglement entropy of the subsystem scales as $\sim L^{d-1}$. In particular, the area law has been proven to hold in the ground state of one-dimensional systems with a mass gap and short-range couplings when the subsystem size is much larger than the correlation length [245]. At a quantum critical point, where the correlation length diverges, the area law is violated by a logarithmic term proportional to the central charge of the conformal field theory (CFT) that describes the low-energy spectrum of the model [246, 247, 248, 249, 250, 251]. These observations originally motivated the study of

entanglement due to its similarity to black hole entropy [252, 243], eventually revealing its important role in high-energy physics [253, 254, 255, 256] as well as in the investigation of condensed matter systems [257, 258, 259].

The previous discussion becomes more complex for systems with long-range couplings [260, 261]. Indeed the prominent collective character of such non-local systems promotes entanglement spreading and leads to novel forms of equilibrium and dynamical scaling, which are not observed in traditional systems with local interactions [262, 263, 264, 265, 266]. In particular, the anomalous scaling of entanglement in the presence of long-range couplings has recently attracted great interest in the context of the so-called measurement-induced transitions [267, 268, 269, 270, 271, 272, 273]. In these scenarios, the dynamical generation of entanglement is weakened by the presence of local measurements applied randomly during the system evolution. Specifically, if the measurement rate is high enough, the steady-state entanglement saturates to an area law value independent of the subsystem size, provided only nearest neighbor interactions are present [274]. On the other hand, in the presence of long-range couplings, subvolume law scalings [274, 275, 276, 277, 278], also referred to as fractal entanglement phases [279, 280], appear.

These intriguing dynamical phenomena lack a clear equilibrium counterpart, indicating that their origin is directly tied to the presence of long-range interactions. The entanglement properties of the ground state of a fermionic chain with long-range pairing couplings and nearest-neighbor hopping amplitudes have been comprehensively characterized in Refs. [281, 97, 282, 283, 284]. These studies reported standard logarithmic violations of the area law in the weak long-range regime. Moreover, an anomalous logarithmic growth was observed even when the mass gap is non-zero, associated with the divergence of unnormalized couplings in the strong long-range regime characterized by a power law decay exponent smaller than the system dimension.

On the other hand, Refs. [285, 286] investigated a model of fermions with strong long-range hopping amplitudes and no pairing, discovering a volume law entanglement scaling. Additionally, the entanglement properties of the Sachdev-Ye-Kitaev (SYK) model [287, 288], a fully connected fermionic model with random interactions, have been extensively studied [289]. Also in this case, the eigenstates of the SYK Hamiltonian display a volume law entanglement scaling, with the coefficient computed numerically using exact diagonalization techniques [290, 291] and analytically via the eigenstate thermalization hypothesis [292] or a path-integral approach exact in the large- N limit [293, 294]. Finally, also in long-range bosonic systems [295, 296] and in fully connected spin systems [297, 298, 299, 300, 301] only logarithmic violations of the area law were reported.

Despite the extensive amount of literature on the topic summarized above, none of the considered long-range models display a fractal entanglement scaling at equilibrium unless additional ingredients, such as modifications of the couplings which violate time translational symmetry or the presence of a fractal Fermi surface [285], are introduced.

In this Chapter, we demonstrate that a subvolume law, similar to the one observed in measurement-induced transitions with long-range interactions [274], can also appear at

equilibrium under certain conditions.

To substantiate our claim, we examine the ground state entanglement scaling in the prototypical long-range Kitaev chain model introduced in Section 1.5. This model, while simple enough for analytic calculations, hosts an extremely rich phenomenology. Using the well-known Fisher-Hartwig expansion approach [302, 303], we analytically determine the leading order dependence of the ground state entanglement on the subsystem size L in the scaling limit of an infinite chain $N \rightarrow \infty$ and infinite subsystem $L \rightarrow \infty$ with fixed $l = L/N$, for different values of the available parameters.

In particular, in the weak long-range regime, the system exhibits standard logarithmic deviations from the entanglement area law at quantum critical points. However, in the case of equal long-range hopping and pairing ($\alpha = \alpha_1 = \alpha_2$), the coefficients of these logarithmic divergences show a nontrivial dependence on the power law decay exponent α which is incompatible with the standard scaling predicted, for short-range systems, by critical conformal field theory [247, 246].

In the strong long-range regime, the system becomes genuinely non-additive, displaying logarithmic deviations from the area law even away from criticality. Most notably, when the system's chemical potential is zero, the Hamiltonian lacks local terms, resulting in a highly degenerate ground state and a subvolume law entanglement scaling $S \sim L^{1-2\alpha}$.

5.2 Entanglement scaling in free fermionic systems

5.2.1 Rényi entropies and the correlation matrix

We begin our analysis by reviewing the techniques used to study the entanglement scaling of generic quadratic fermionic models. Specifically, we consider a bipartition of a generic quadratic fermionic chain into two subsystems, A and B , where A is a continuous interval of chain sites of length L and B is its complementary set, see Fig. 5.1. Given the Hilbert spaces \mathcal{H}_A and \mathcal{H}_B associated to A and B , respectively, the total Hilbert space of the system is $\mathcal{H} = \mathcal{H}_A \otimes \mathcal{H}_B$. If the total system is in a pure state $|\psi\rangle$, then the reduced density matrix, describing the state of subsystem $A(B)$ is obtained by taking the partial trace with respect to $\mathcal{H}_{A(B)}$: $\rho_{A(B)} = \text{Tr}_{A(B)}|\psi\rangle\langle\psi|$.

The amount of entanglement between the two subsystems can be characterized by the Rényi entropies of A , defined as

$$S_{\nu,L}(A) = \frac{1}{1-\nu} \ln \text{Tr}[\rho_A^\nu], \quad (5.1)$$

where $\nu \geq 1$. These entropies provide an accurate measure of the entanglement in a bipartite system in a pure state [242]. In particular, the limit $\nu \rightarrow 1$ corresponds to the well-known Von Neumann or entanglement entropy

$$S_L(A) = S_{1,L}(A) = -\text{Tr}[\rho_A \ln \rho_A]. \quad (5.2)$$

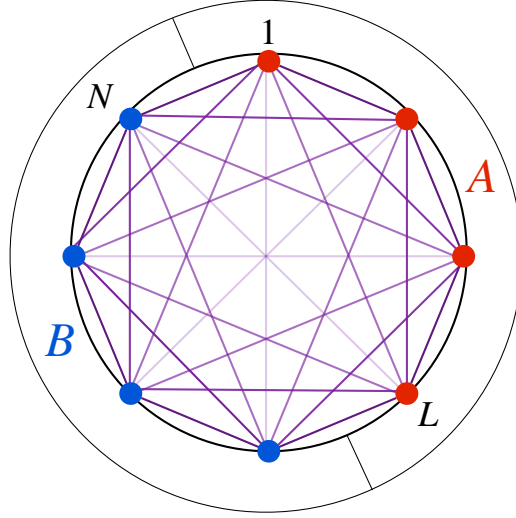


Figure 5.1: Schematic representation of a bipartition of a long-range Kitaev chain with periodic boundary conditions in two subsystems A and B of length L and $N-L$ respectively.

Our main goal is to study the Rényi entanglement entropy for the ground state of the Hamiltonian discussed in Section 1.5. In particular, we aim to determine how $S_{\nu,L}(A)$ depends on the subsystem size L in the scaling limit $N \rightarrow \infty, L \rightarrow \infty$ with fixed $l = L/N$ particularly focusing on the effects of long-range hopping and pairing couplings in the Hamiltonian.

This task is facilitated by the fact that the long-range Kitaev chain Hamiltonian in Eq. (1.43) is quadratic, meaning that all its eigenstates satisfy the Wick decomposition theorem [249, 304]. Consequently, the reduced density matrix can be derived from the two-point correlation functions. To this end, we introduce the $2N \times 2N$ correlation matrix \mathbb{V} , which is a block matrix with each 2×2 block defined as

$$\mathbb{V}_{ij} = \begin{pmatrix} \delta_{ij} - 2\langle c_j^\dagger c_i \rangle & 2\langle c_i c_j \rangle \\ 2\langle c_i^\dagger c_j^\dagger \rangle & 2\langle c_i^\dagger c_j \rangle - \delta_{ij} \end{pmatrix}, \quad (5.3)$$

where i and j range from 1 to N . Then, it can be shown [249, 304] that the Rényi entropies can be expressed in terms of \mathbb{V} as

$$S_{\nu,L}(A) = \frac{1}{2(\nu-1)} \text{Tr} \ln \left[\left(\frac{\mathbb{I} + \mathbb{V}}{2} \right)^\nu + \left(\frac{\mathbb{I} - \mathbb{V}}{2} \right)^\nu \right]. \quad (5.4)$$

It is important to note that from a computational perspective, this formula offers a significant simplification. The problem complexity is reduced from the diagonalization of a reduced density matrix of size $2^L \times 2^L$ to the diagonalization of the correlation matrix (5.3) of size $2L \times 2L$. This reduction enables the analysis of much larger subsystem sizes L .

5.2.2 Matrix symbol of the correlation matrix

From the analytic side, it is useful to write Eq. (5.4) as an integral in the complex plane along a contour \mathcal{C} surrounding the eigenvalues $v_j \in [-1, 1]$ of \mathbb{V} . Applying Cauchy's residue theorem to perform the integral, we obtain [305, 306]

$$S_{\nu,L}(A) = \lim_{\epsilon \rightarrow 0^+} \oint_{\mathcal{C}} s_{\nu}(1 + \epsilon, z) \frac{d \ln D_L(z)}{dz} dz, \quad (5.5)$$

where we have introduced the function

$$s_{\nu}(x, y) = \frac{1}{1 - \nu} \ln \left[\left(\frac{x + y}{2} \right)^{\nu} + \left(\frac{x - y}{2} \right)^{\nu} \right], \quad (5.6)$$

and the determinant

$$D_L(z) = \det(z\mathbb{I} - \mathbb{V}). \quad (5.7)$$

Due to the translational invariance of the Hamiltonian (1.43) and the choice of subsystem A , which consists of contiguous sites, the Fourier transform of the correlation matrix \mathbb{V}_{lj} can be expressed as

$$\mathbb{V}_{lj} = \frac{1}{N} \sum_k G_k e^{ik(l-j)}, \quad (5.8)$$

where we have introduced the two dimensional matrix symbol G_k .

Starting from the definition of the correlation matrix of a stationary state $|\psi\rangle$, and passing to the Fourier basis, we obtain

$$G_k = 2\langle\psi| \begin{pmatrix} \hat{c}_k \\ \hat{c}_{-k}^{\dagger} \end{pmatrix} \begin{pmatrix} \hat{c}_k^{\dagger} & \hat{c}_{-k} \end{pmatrix} |\psi\rangle - I. \quad (5.9)$$

Using the Bogoliubov transformation

$$\begin{pmatrix} \hat{\gamma}_k \\ \hat{\gamma}_{-k}^{\dagger} \end{pmatrix} = U_k \begin{pmatrix} \hat{c}_k \\ \hat{c}_{-k}^{\dagger} \end{pmatrix}, \quad U_k = \begin{pmatrix} \cos \phi_k/2 & i \sin \phi_k/2 \\ -i \sin \phi_k/2 & -\cos \phi_k/2 \end{pmatrix}, \quad (5.10)$$

we can express the symbol in terms of the Bogoliubov fermionic operators as

$$G_k = 2U_k^{\dagger} \langle\psi| \begin{pmatrix} \hat{\gamma}_k \\ \hat{\gamma}_{-k}^{\dagger} \end{pmatrix} \begin{pmatrix} \hat{\gamma}_k^{\dagger} & \hat{\gamma}_{-k} \end{pmatrix} |\psi\rangle U_k - I. \quad (5.11)$$

We now compute the expectation value in a stationary state associated to the fermionic populations of the Bogoliubov modes $f_k = \langle\hat{\gamma}_k^{\dagger} \hat{\gamma}_k\rangle$, which for a generic state satisfy the condition $0 \leq f_k \leq 1$, so that

$$2\langle\psi| \begin{pmatrix} \hat{\gamma}_k \\ \hat{\gamma}_{-k}^{\dagger} \end{pmatrix} \begin{pmatrix} \hat{\gamma}_k^{\dagger} & \hat{\gamma}_{-k} \end{pmatrix} |\psi\rangle - I = \begin{pmatrix} 1 - 2f_k & 0 \\ 0 & 2f_k - 1 \end{pmatrix}. \quad (5.12)$$

Finally, substituting this expectation value into Eq. (5.11) and using the definition of the Bogoliubov angles $\tan \theta_k = \tilde{\Delta}_k / (h - \tilde{t}_k)$ we obtain

$$G_k = (1 - (f_k + f_{-k})) \left[\frac{2(h - \tilde{t}_k)}{\omega_k} \sigma_z - \frac{2\tilde{\Delta}_k}{\omega_k} \sigma_y \right] - (f_k - f_{-k}) I, \quad (5.13)$$

where σ_a , with $a = x, y, z$, are the Pauli sigma matrices, I is the 2×2 identity.

5.2.3 The Fisher-Hartwig expansion

Using the techniques introduced in Refs. [249, 304] we can determine the asymptotic behavior of the Toeplitz determinant $D_L(z)$, as $L \rightarrow \infty$. This is achieved by applying the Szegő-Widom theorem [307, 308] and an extension of the Fisher-Hartwig conjecture [302, 303] to non-scalar symbols [282, 283]. The leading-order contributions to the logarithm of $D_L(z)$ in the $L \rightarrow \infty$ limit are given by

$$\begin{aligned} \ln D_L(z) &= \frac{L}{2\pi} \int_{-\pi}^{\pi} dk \ln \det(z\mathbb{I} - G_k) \\ &\quad + \ln L \sum_p b_p(z) + \mathcal{O}(1), \end{aligned} \quad (5.14)$$

where the coefficients $b_p(z)$ of the logarithmic contribution are associated with the discontinuities of G_k . Specifically, if there is a discontinuity at some $k = p$, this means that

$$G_p^+ = \lim_{k \rightarrow p^+} G_k \neq \lim_{k \rightarrow p^-} G_k = G_p^-, \quad (5.15)$$

then the corresponding coefficient can be computed as [283]

$$b_p(z) = \frac{1}{4\pi^2} \text{Tr}[\ln(z\mathbb{I} - G_p^-)(z\mathbb{I} - G_p^+)^{-1}]^2. \quad (5.16)$$

Inserting Eq. (5.14) into the integral for the Rényi entropy (5.5) one obtains

$$S_{\nu,L} = \frac{1}{1-\nu} \sum_k \ln [(1 - f_k)^\nu + f_k^\nu] + B_\nu \ln L + \mathcal{O}(1), \quad (5.17)$$

where the coefficient of the logarithmic contribution can be computed as

$$B_\nu = \sum_p \lim_{\epsilon \rightarrow 0^+} \oint_C s_\nu(1 + \epsilon, z) \frac{db_p(z)}{dz} dz. \quad (5.18)$$

As shown in Section 1.5, whenever $\alpha_{1,2} > 0$ or $\alpha_1 = \alpha_2 = 0$ and $h \neq 0$, the many-body ground state of the system is the Bogoliubov vacuum with $f_k = 0 \forall k$, therefore we are left with a leading order contribution given by a constant term $\mathcal{O}(1)$ corresponding to

the standard area law in the one-dimensional case, or a logarithmic contribution which is associated to the discontinuity of the correlation matrix symbol G_k . On the other hand in the specific case $\alpha_1 = \alpha_2 = 0$ and $h = 0$ the many-body ground state becomes highly degenerate allowing for a finite fermionic population $f_k \neq 0$ for an extensive number of Bogoliubov modes, i.e., all the even modes. As a consequence, the first term in Eq. (5.17) becomes the leading contribution to the large L entanglement scaling corresponding to a volume law behavior $S_{\nu,L}(\alpha_{1,2} = 0, h = 0) \approx L$.

Summarizing, the machinery introduced in this Section allows us to compute the leading order contribution to the scaling of Rényi entropies with the subsystem size by simply analyzing the continuity properties of the matrix symbol G_k in the different regimes.

5.2.4 Computation of the Fisher-Hartwig expansion coefficients

The general form of the matrix symbol in Eq. (5.11) can be used to compute the different terms in the Fisher-Hartwig expansion of the Rényi entropies for large subsystem size. For this purpose, it is useful to rewrite G_k as

$$G_k = a_k [\cos \phi_k \sigma_z + \sin \phi_k \sigma_y] + b_k I, \quad (5.19)$$

where we have introduced the coefficients $a_k = 1 - (f_k + f_{-k})$ and $b_k = f_{-k} - f_k$ and the angle ϕ_k such that $\cos \phi_k = 2(h - \tilde{t}_k)/\omega_k$ and $\sin \phi_k = -2\tilde{\Delta}_k/\omega_k$.

Let us start from the first term of the expansion in Eq. (5.17) this is obtained by first computing the determinant

$$\det [z\mathbb{I} - G_k] = (z - b_k)^2 - a_k^2, \quad (5.20)$$

Then, the contribution to first term in the entanglement scaling coming from each k -mode is obtained from the integral

$$\begin{aligned} \mathcal{S}_k &= \lim_{\epsilon \rightarrow 0^+} \oint_{\mathcal{C}} \frac{dz}{2\pi i} s_\nu(1 + \epsilon, z) \frac{(z - b_k)}{(z - b_k)^2 - a_k^2} \\ &= \frac{1}{2} [s_\nu(1, b_k + a_k) + s_\nu(1, b_k - a_k)] \\ &= \frac{1}{2(1 - \nu)} [\ln(f_k^\nu + (1 - f_k)^\nu) + \ln(f_{-k}^\nu + (1 - f_{-k})^\nu)], \end{aligned} \quad (5.21)$$

where Cauchy's residue theorem and the expression (5.6) for $s_\nu(x, y)$ have been used. Finally, summing over all the modes and using the $k \rightarrow -k$ symmetry we obtain

$$\sum_k \mathcal{S}_k = \frac{1}{1 - \nu} \sum_k \ln(f_k^\nu + (1 - f_k)^\nu). \quad (5.22)$$

The logarithmic contribution to the entanglement scaling can be computed by considering the discontinuity coefficients. Here, we present their calculation in the general

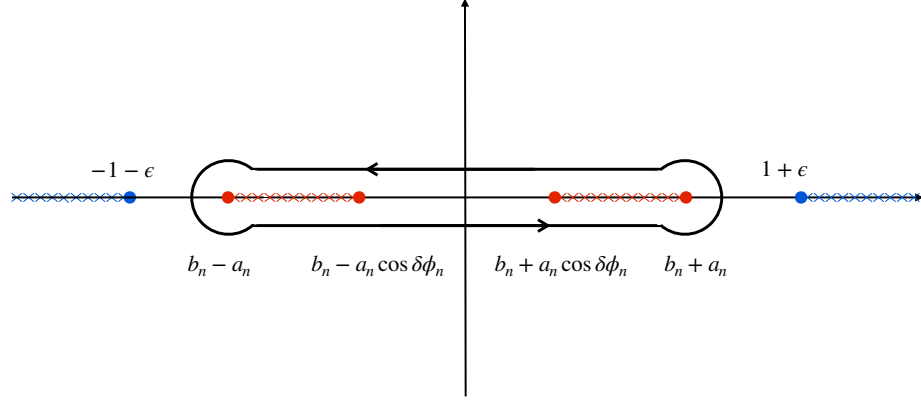


Figure 5.2: Contour of integration and cuts of the integrand in Eq. (5.26). The cuts from $\pm(1 + \epsilon)$ to the infinity correspond to $ds_\nu(1 + \epsilon, z)/dz$ while the cuts inside the contour, $[b_n - a_n, b_n - a_n \cos \delta\phi]$ and $[b_n + a_n \cos \delta\phi, b_n + a_n]$, are due to the other factor of the integrand.

situation in which G_k is discontinuous at a generic mode $k = 2\pi n/N$. We start from the definition (5.16) of the b_k coefficients corresponding to each discontinuity. First of all, we consider the matrix

$$M_k = (z\mathbb{I} - G_k^-)(z\mathbb{I} - G_k^+)^{-1}, \quad (5.23)$$

where $G_k^\pm = \lim_{p \rightarrow k^\pm} G_p$. The eigenvalues $\mu_k^\pm(z)$ of this matrix can be written in the form

$$\mu_k^\pm(z) = \left(\frac{\sqrt{(b_k - z)^2 - a_k^2 \cos^2(\delta\phi_k/2)} \pm a_k \sin(\delta\phi_k/2)}{\sqrt{(b_k - z)^2 - a_k^2}} \right)^2, \quad (5.24)$$

with $\delta\phi_k = \phi_k^+ - \phi_k^-$. Notice also that we have $\mu_k^+(z) = 1/\mu_k^-(z)$, therefore

$$\begin{aligned} b_k(z) &= \frac{1}{2\pi^2} (\ln \mu_k^+(z))^2 \\ &= \frac{2}{\pi^2} \left[\ln \left(\frac{\sqrt{(b_k - z)^2 - a_k^2 \cos^2(\delta\phi_k/2)} + a_k \sin(\delta\phi_k/2)}{\sqrt{(b_k - z)^2 - a_k^2}} \right) \right]^2, \end{aligned} \quad (5.25)$$

From this expression we compute the coefficient $B_\nu^{(k)}$ of the contribution of this discontinuity to the logarithmic term of the Rényi entropy. For this purpose we plug $b_k(z)$ into

the contour integral for $S_{\nu,L}$ then, performing an integration by parts, we obtain

$$\begin{aligned}
 B_\nu^{(k)} &= \lim_{\epsilon \rightarrow 0^+} \oint_{\mathcal{C}} \frac{dz}{2\pi i} s_\nu(1+\epsilon, z) \frac{db_k(z)}{dz} \\
 &= - \lim_{\epsilon \rightarrow 0^+} \oint_{\mathcal{C}} \frac{dz}{2\pi^3 i} \frac{ds_\nu(1+\epsilon, z)}{dz} \left[\ln \left(\frac{\sqrt{(b_k - z)^2 - a_k^2 \cos^2(\delta\phi_k/2)} + a_k \sin(\delta\phi_k/2)}{\sqrt{(b_k - z)^2 - a_k^2}} \right) \right]^2.
 \end{aligned} \tag{5.26}$$

The integral over the contour \mathcal{C} depicted in Fig. 5.2 can be divided into two integrals along curves enclosing respectively the cuts $[b_k - a_k, b_k - a_k \cos \delta\phi_k]$ and $[b_k + a_k, b_k + a_k \cos \delta\phi_k]$, which in turn can be reduced to two real integrals by performing the integration along the cuts taking into account the change in the phase of the logarithm when we go around the branch points $b_k \pm a_k$ and $b_k \pm a_k \cos \delta\phi_k$. On the other hand, we notice that for integer $\nu > 1$, ds_ν/dz is a meromorphic function with poles located at the points of the imaginary axis [282, 283]

$$z_l = i \tan \frac{\pi(2l-1)}{2\nu}, \quad l = 1, \dots, \nu, \quad l \neq \frac{1+\nu}{2}, \tag{5.27}$$

and that the other factor of the integrand is analytic in the whole region outside the contour \mathcal{C} . We can send this contour to infinity and reduce the calculation of B_ν to the computation of the corresponding residues. In this way, we obtain the explicit expression

$$B_\nu^{(k)} = \frac{1}{\nu-1} \sum_{l=1}^{\nu} \left[\ln \left(\frac{\sqrt{(b_k - z_l)^2 - a_k^2 \cos^2(\delta\phi_k/2)} + a_k \sin(\delta\phi_k/2)}{\sqrt{(b_k - z_l)^2 - a_k^2}} \right) \right]^2. \tag{5.28}$$

5.3 Entanglement scaling in the weak long-range regime

In this section, we analyze the entanglement scaling for the ground state of a long-range Kitaev chain in the weak long-range regime, characterized by $1 < \alpha_1, \alpha_2 < 2$. As detailed in Section 1.5, in this regime, the quasiparticle spectrum is continuous in the thermodynamic limit, and the ground state is always the Bogoliubov vacuum with zero fermionic populations ($f_k = 0, \forall k$). Consequently, the first term in the Fisher-Hartwig expansion (5.17) vanishes, and the leading-order contribution to the entanglement scaling arises from the logarithmic term associated with the matrix symbol discontinuity.

Within the weak long-range regime, we can distinguish three scenarios: $\alpha_1 > \alpha_2$, $\alpha_1 < \alpha_2$ and $\alpha_1 = \alpha_2 = \alpha$. To proceed, we must identify the locations of the jumps in G_k and compute the corresponding lateral limits in these different cases. Possible sources of discontinuities for G_k include the discontinuities or zeros of the spectrum $\omega_k(h)$, which occur at the two quantum critical points of the model $h = 1, -1 + 2^{1-\alpha_1}$, where the spectrum becomes gapless at the soft modes $k = 0, \pi$, respectively. Specifically, G_k has no

discontinuities when $h \neq 1, -1 + 2^{1-\alpha_1}$, since in these cases, the lateral limits at the critical modes are

$$G_0^\pm = \lim_{k \rightarrow 0^\pm} G_k = \text{sgn}(h - 1)\sigma_z, \quad (5.29)$$

$$G_\pi^\pm = \lim_{k \rightarrow \pi^\pm} G_k = \text{sgn}(h + 1 - 2^{1-\alpha_1})\sigma_z. \quad (5.30)$$

This results in a constant scaling of the entanglement entropy $S_{\nu,L} = \mathcal{O}(1)$ with the subsystem size when the system is not at quantum criticality, manifesting the standard area law for one-dimensional gapped systems [243, 244]. However, quantum criticality leads to logarithmic deviations from the area law. In particular specializing the general formula in Eq.(5.28) to the discontinuity arising at the two quantum critical points $h = h_c = 1, -1 + 2^{1-\alpha_1}$ in correspondence of the critical modes $k = k_c = 0, \pi$, we obtain the logarithmic scaling with coefficient

$$\begin{aligned} B_\nu^{(k_c)} &= \frac{1}{\nu - 1} \sum_{l=1}^{\nu} \left[\ln \left(\frac{\sqrt{|z_l|^2 + \cos^2(\delta\phi_{k_c}/2)} - i \sin(\delta\phi_{k_c}/2)}{\sqrt{|z_l|^2 - 1}} \right) \right]^2 \\ &= \frac{1}{\nu - 1} \sum_{l=1}^{\nu} \left[\arctan \left(\frac{\sin(\delta\phi_{k_c}/2)}{\sqrt{|z_l|^2 + \cos^2(\delta\phi_{k_c}/2)}} \right) \right]^2, \end{aligned} \quad (5.31)$$

where in the last step we have used the identity $\arctan(x) = i[\ln(i+x) - \ln(i-x)]/2$ in order to make the expression of the coefficient explicitly real. The value of $\delta\phi_{k_c}$ depends on the critical point considered and the relative order of the power law decaying exponents α_1 and α_2 .

Let us start with the critical point at $h = 1$, where the spectrum has an $\alpha_{1,2}$ dependent dispersion relation. In particular, near $k = 0$, we have the following expansions for \tilde{t}_k and $\tilde{\Delta}_k$ [36]

$$\tilde{t}_k = 1 + \sin(\alpha_1) \frac{\Gamma(1 - \alpha_1)}{\zeta(\alpha_1)} |k|^{\alpha_1 - 1} + \mathcal{O}(k^2), \quad (5.32)$$

$$\tilde{\Delta}_k = \cos(\alpha_2) \frac{\Gamma(1 - \alpha_2)}{\zeta(\alpha_2)} \text{sgn}(k) |k|^{\alpha_2 - 1} + \mathcal{O}(k), \quad (5.33)$$

with $\Gamma(x)$ and $\zeta(x)$ the Gamma and the Riemann zeta functions [37], respectively. Consequently, the single-particle spectrum takes the form [11]

$$\omega_k = \begin{cases} |h - 1| + \mathcal{O}(|k|^{\alpha - 1}) & \text{if } h \neq 1 \\ \mathcal{C}(\alpha) |k|^{\alpha - 1} + \mathcal{O}(k^{2\alpha - 2}) & \text{if } h = 1 \end{cases}, \quad (5.34)$$

where $\alpha = \min\{\alpha_1, \alpha_2\}$, and we have introduced the constant prefactor

$$\mathcal{C}(\alpha) = \begin{cases} |\sin(\alpha_1\pi/2)\Gamma(1 - \alpha_1)/\zeta(\alpha_1)| & \text{if } \alpha_1 < \alpha_2 \\ |\Gamma(1 - \alpha)/\zeta(\alpha)| & \text{if } \alpha_1 = \alpha_2 \\ |\cos(\alpha_2\pi/2)\Gamma(1 - \alpha_2)/\zeta(\alpha_2)| & \text{if } \alpha_1 > \alpha_2 \end{cases}. \quad (5.35)$$

This leads to the different lateral limits

$$G_0^\pm = \begin{cases} -\mathcal{A}(\alpha_1)\sigma_z & \text{if } \alpha_1 < \alpha_2 \\ -\sin(\alpha\pi/2)\sigma_z \pm \cos(\alpha\pi/2)\sigma_y & \text{if } \alpha_1 = \alpha_2, \\ \pm\mathcal{B}(\alpha_2)\sigma_y & \text{if } \alpha_1 > \alpha_2 \end{cases} \quad (5.36)$$

where $\mathcal{A}(\alpha) = \sin(\alpha\pi/2)\Gamma(1-\alpha)/\zeta(\alpha)$, and $\mathcal{B}(\alpha) = \cos(\alpha\pi/2)\Gamma(1-\alpha)/\zeta(\alpha)$. Moreover, the jump in the Bogoliubov angle at the critical mode read

$$\delta\phi_0 = \begin{cases} 0 & \text{if } \alpha_1 < \alpha_2 \\ \pi(1-\alpha) & \text{if } \alpha_1 = \alpha_2 = \alpha \\ \pi & \text{if } \alpha_1 > \alpha_2. \end{cases} \quad (5.37)$$

Leading to the logarithmic coefficients

$$B_\nu^0(h=1) = \begin{cases} 0 & \text{if } \alpha_1 < \alpha_2 \\ \frac{1}{\nu-1} \sum_{l=1}^{\nu} \left[\arctan \left(\frac{\cos(\alpha\pi/2)}{\sqrt{|z_l|^2 + \sin^2(\alpha\pi/2)}} \right) \right]^2 & \text{if } \alpha_1 = \alpha_2 = \alpha, \\ \frac{\nu+1}{12\nu} & \text{if } \alpha_1 > \alpha_2 \end{cases} \quad (5.38)$$

with $z_{k,\nu} = i \tan(\pi(2k-1)/2\nu)$.

When the power-law decay of the hopping amplitude is slower than that of the pairing, no discontinuity is present, leading to a constant entanglement entropy.

In the case $\alpha_1 > \alpha_2$, we have a discontinuity in the symbol, with commuting lateral limits. Inserting the expression for G_0^\pm in Eq. (5.16) we obtain the logarithmic scaling

$$S_{\nu,L} = \frac{\nu+1}{12\nu} \ln L + \mathcal{O}(1). \quad (5.39)$$

This logarithmic scaling is analogous to the one obtained for a conformal field theory with central charge $c = 1/2$ [247]. This result align with earlier studies [282, 97] that investigated the entanglement scaling in a Kitaev chain with long-range pairing and nearest-neighbor hopping ($\alpha_1 \rightarrow \infty$). Here, we show that this scaling persists for finite α_1 as long as $\alpha_1 > \alpha_2$. Figure 5.3(b) shows the numerical check of the scaling behavior of the entanglement entropy $S_L = S_{1,L}$ for $\alpha_1 > \alpha_2$ and $h = 1$. We obtain an excellent agreement once the subleading corrections are taken into account. In particular, we need to subtract from the numerical data the finite size corrections of the form

$$S_L - \frac{1}{6} \ln L = c_1 + c_2 L^{-c_3}, \quad (5.40)$$

where the $c_i = c_i(\alpha_1, \alpha_2, h)$, $i = 1, 2, 3$, coefficients can be estimated from a fit with the numerical data.

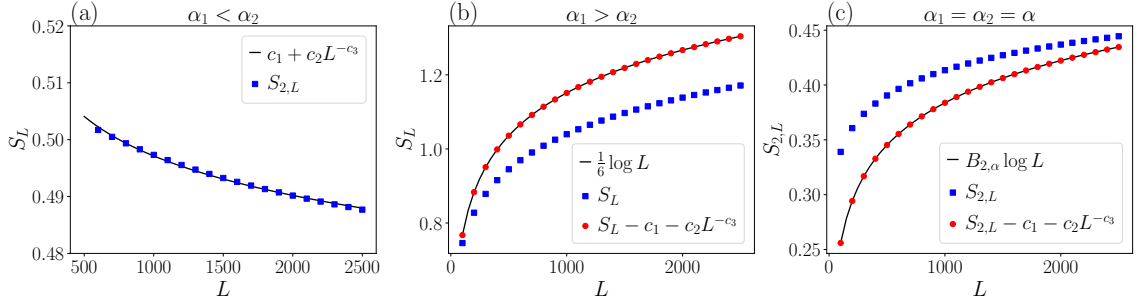


Figure 5.3: Numerical check of the entanglement scaling as a function of the subsystem size L at the quantum critical point with chemical potential $h = 1$ for different values of couplings power law decay exponents $1 < \alpha_1, \alpha_2$. a) Entanglement entropy ($\nu = 1$), with $\alpha_1 = 1.5$ and $\alpha_2 = 1.8$, blue squares represent the numerical data while the black solid line is a fit of a constant and a subleading contribution $c_1 + c_2 L^{-c_3}$. b) Entanglement entropy ($\nu = 1$), with $\alpha_1 = 1.8$ and $\alpha_2 = 1.5$, blue squares represents the numerical data, the black solid line correspond to the curve $(1/6) \ln L$, red dots have been obtained from the numerics by subtracting the fit of the subleading corrections of the form $c_1 + c_2 L^{-c_3}$. c) Rényi-2 entropy ($\nu = 2$) with $\alpha_1 = \alpha_2 = 1.5$, blues squares represents the numerics, the black solid line represents the curve $B_{2,\alpha} \ln L$, red dots are obtained subtracting the subleading corrections to the numerical data as in panel b).

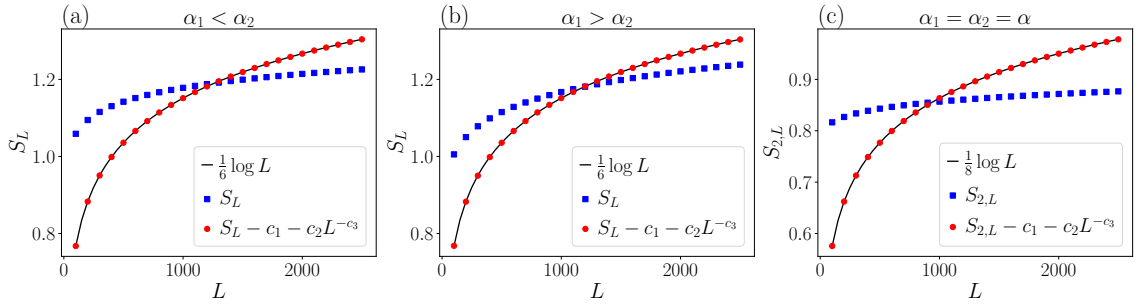


Figure 5.4: Numerical check of the entanglement scaling as a function of the subsystem size L at the quantum critical point with chemical potential $h = -1 + 2^{1-\alpha_1}$ for different values of couplings power law decay exponents: a) $\alpha_1 = 1.5, \alpha_2 = 1.8$, b) $\alpha_1 = 1.8, \alpha_2 = 1.5$, c) $\alpha_1 = \alpha_2 = 1.5$. As in Fig.5.3, blue squares represents the numerical data, the black solid line represents our analytical prediction for the scaling in the $L \gg 1$ limit, red dots are obtained from the numerics by subtracting the subleading corrections.

The most interesting case corresponds to the condition $\alpha_1 = \alpha_2 = \alpha$ which, as previously stated, is related to the long-range interacting quantum Ising chain. In this regime the matrix symbol G_k , hosts non-commuting lateral limits as $k \rightarrow 0^\pm$ (see Eq. (5.36)). This leads to the non-trivial dependence of the logarithmic contribution coefficient on α , leading the logarithmic scaling behavior of the Rényi entropy

$$S_{\nu,L} = B_{\nu,\alpha} \ln L + \mathcal{O}(1), \quad (5.41)$$

where

$$B_{\nu,\alpha} = \frac{1}{\pi^2(\nu-1)} \sum_{k=1}^{\nu} \arctan^2 \left[\frac{\cos(\alpha\pi/2)}{\sqrt{\sin^2(\alpha\pi/2) + |z_{k,\nu}|^2}} \right], \quad (5.42)$$

with $z_{k,\nu} = i \tan(\pi(2k-1)/2\nu)$. In particular, for $\nu = 2, 3$, the sum in the previous expression reduces to

$$B_{2,\alpha} = \frac{2}{\pi^2} \arctan^2 \left[\frac{\cos(\alpha\pi/2)}{\sqrt{\sin^2(\alpha\pi/2) + 1}} \right], \quad (5.43)$$

$$B_{3,\alpha} = \frac{1}{\pi^2} \arctan^2 \left[\frac{\cos(\alpha\pi/2)}{\sqrt{\sin^2(\alpha\pi/2) + 1/3}} \right]. \quad (5.44)$$

This analytical scaling of $S_{2,\nu}$ at $h = 1$ and for $\alpha_1 = \alpha_2 = \alpha$ is compared with the numerical result in Fig. 5.3(c). Also in this case, a good agreement is found once the subleading corrections (5.40) are taken into account.

We note that the expression for the scaling coefficients in Eq. (5.42) is valid only for integers $\nu > 1$. Indeed, in this case ds_ν/dz is a meromorphic function with poles located on the imaginary axis. This allows us to evaluate the integral in (5.5) by summing over the residues at these poles (see Section 5.2.4). On the other hand, for $\nu = 1$, we have that

$$\frac{ds_{\nu=1}(1+\epsilon, z)}{dz} = \ln \left(\frac{1+\epsilon-z}{1+\epsilon+z} \right), \quad (5.45)$$

which has two branch cuts from $\pm(1+\epsilon)$ to infinity (see Section 5.2.4). Therefore, to evaluate the integral in Eq. (5.5) for $\nu = 1$, we perform the integration along these cuts and take into account the change in the phase of the logarithm when we go around the branch points. This reduces the integral to two real integrals, which we may evaluate numerically. In the case where $\alpha_1 = \alpha_2 = \alpha$ and $h = 1$, the integrand still depends on α even for $\nu = 1$, so we can still expect the coefficient for the logarithmic divergence of the von Neumann entropy $S_{1,L}$ to have a nontrivial α dependence. It is important to observe that at variance with the $\alpha_1 \neq \alpha_2$ cases, the scaling coefficient $B_{\nu,\alpha}$ cannot be written in the form

$$B_{\nu,\alpha} \neq B_{\nu,\text{CFT}} = \frac{\nu+1}{6\nu} c, \quad (5.46)$$

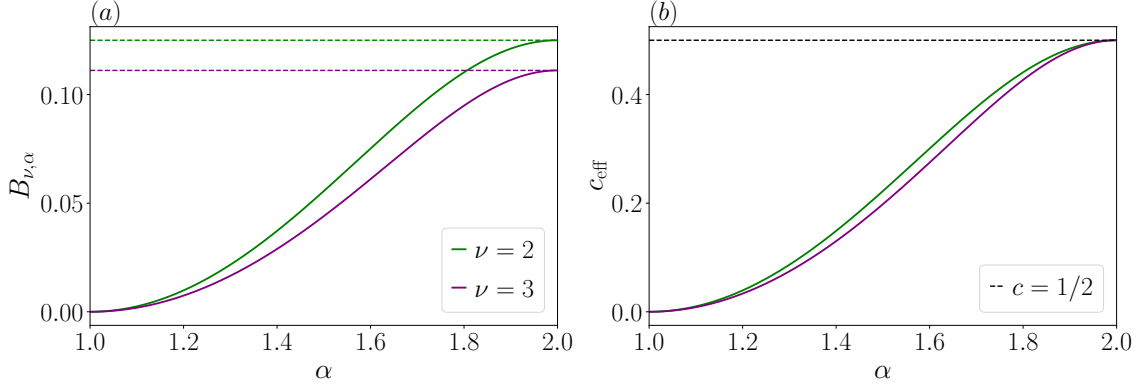


Figure 5.5: *a)* Coefficient $B_{\nu,\alpha}$ of the logarithmic scaling of the ν -Rényi entropy as a function of the power law decay exponent $\alpha = \alpha_1 = \alpha_2$, for $\nu = 2$ (green solid line) and $\nu = 3$ (purple solid line). The dashed lines correspond to the short-range values of the coefficients which are matched by the long-range ones for $\alpha = 2$. *b)* effective central charge, obtained as $c_{\text{eff}} = 6\nu B_{\nu,\alpha}/(\nu + 1)$, as a function of α for $\nu = 2, 3$. The black dashed line represents the central charge for nearest neighbor couplings $c = 1/2$.

where c is the central charge of some conformal field theory describing the model at the quantum critical point. This observation supports our previous claim that the case $\alpha_1 = \alpha_2$ is special and, somehow, closer to the one of a strongly interacting system such as the long-range Ising model. Indeed, while the case $\alpha_1 \neq \alpha_2$ continues to obey the r.h.s. of Eq. (5.46) and, so, is more likely to be described by a CFT, the case $1 < \alpha_1 = \alpha_2 < 2$ goes beyond this description as the scaling of the ground state entanglement at the critical point cannot be related to the universal properties of a conformal field theory. A similar result is expected for the Ising model in a transverse field, where the inclusion of long-range interactions is expected to increase the effective dimension of the model (see Chapter 2) and, so, disrupt any CFT description.

Figure 5.5(a) shows the coefficients $B_{\nu,\alpha}$ for $\nu = 2, 3$ as a function of $\alpha \in [1, 2]$, we notice that the value of the logarithmic scaling coefficients starts from zero at $\alpha = 1$ and then grows with α reaching the short-range value for $\alpha = 2$. Moreover, Fig. 5.5(b) shows the α dependence of the effective central charge defined as $c_{\text{eff}}(\alpha) = 6\nu B_{\nu,\alpha}/(\nu + 1)$ as a function of α . We notice that, apart from the extrema $c_{\text{eff}}(1) = 0$ and $c_{\text{eff}}(2) = 1/2$, the effective charge also depends on the Rényi entropy order ν , thus confirming the fact that it cannot be considered as the proper central charge of a conformal field theory. These results are in agreement with the findings of Ref. [309], where the breakdown of conformal symmetry in a long-range fermionic chain was established.

Finally, we consider the critical point $h = -1 + 2^{1-\alpha_1}$. In this case, the power of the dispersion relation near the soft mode $k = \pi$ is not affected by the presence of long-range

couplings. More precisely, in this case the Taylor expansions around the critical mode $k = \pi$ are derived from the expansions at $k = 0$, by using the following property of the polylogarithm

$$\text{Li}_\alpha(ze^{i\pi}) = 2^{1-\alpha}\text{Li}_\alpha(z^2) - \text{Li}_\alpha(z). \quad (5.47)$$

Applying this property to the definitions of \tilde{t}_k and $\tilde{\Delta}_k$, we obtain

$$\tilde{t}_k = 2^{1-\alpha_1}\tilde{t}_{2(k-\pi)} - \tilde{t}_{k-\pi} \quad (5.48)$$

$$\tilde{\Delta}_k = 2^{1-\alpha_2}\tilde{\Delta}_{2(k-\pi)} - \tilde{\Delta}_{k-\pi}. \quad (5.49)$$

The Taylor expansion of \tilde{t}_k and $\tilde{\Delta}_k$ around $k = \pi$ follows by applying the expansion around $k' = 0$ to $t_{k'}$ and $\Delta_{k'}$ with $k' = 2(k - \pi)$ and $k' = k - \pi$, respectively, leading to

$$\begin{aligned} \tilde{t}_k &= -1 + 2^{1-\alpha_1} - \frac{(2^{3-\alpha_1} - 1)\zeta(\alpha_1 - 2)}{2\zeta(\alpha_1)}(\pi - k)^2 \\ &\quad + \mathcal{O}((\pi - k)^3), \end{aligned} \quad (5.50)$$

$$\tilde{\Delta}_k = \frac{(1 - 2^{2-\alpha_2})\zeta(\alpha_2 - 1)}{\zeta(\alpha_2)}(\pi - k) + \mathcal{O}((\pi - k)^3). \quad (5.51)$$

This leads to the $\alpha_{1,2}$ -independent dispersion relation

$$\omega_k = \begin{cases} |h + 1 - 2^{1-\alpha_1}| + \mathcal{O}((k - \pi)^2) & \text{if } h \neq -1 + 2^{1-\alpha_1} \\ \mathcal{K}(\alpha_2)|\pi - k| + \mathcal{O}((k - \pi)^3) & \text{if } h = -1 + 2^{1-\alpha_1} \end{cases}, \quad (5.52)$$

where $\mathcal{K}(\alpha_2) = (1 - 2^{2-\alpha_2})\zeta(\alpha_2 - 1)/\zeta(\alpha_2)$, $\forall \alpha_1, \alpha_2 > 1$.

Accordingly, also the symbol discontinuity is independent of the value of $\alpha_{1,2}$, in particular, we find

$$G_\pi^\pm = \lim_{k \rightarrow \pi^\pm} G_k = \pm\sigma_y, \quad \forall \alpha_1, \alpha_2 > 1. \quad (5.53)$$

This leads to a logarithmic contribution coefficient

$$b_\pi(z) = \frac{1}{2\pi^2} \left(\ln \left(\frac{z+1}{z-1} \right) \right)^2. \quad (5.54)$$

The corresponding scaling of the entanglement entropy is then the one obtained in Eq. (5.39), which is equivalent to the entanglement scaling in the nearest neighbor Kitaev chain, at a quantum critical point characterized by a conformal field theory with central charge $c = 1/2$. Figure 5.4 shows the entanglement scaling behavior at the non-homogeneous critical point $h = -1 + 2^{1-\alpha_1}$ with $\alpha_1 < \alpha_2$ (Fig. 5.4(a)), $\alpha_1 > \alpha_2$ (Fig. 5.4(b)) and $\alpha_1 = \alpha_2$ (Fig. 5.4(c)). Also in this case a nice agreement with the theoretical prediction in the thermodynamic limit is found once finite size corrections are taken into account.

The results for the entanglement scaling with the subsystem size at different critical points and for different values of the α_1, α_2 parameters within the weak long-range regime considered in this section ($1 < \alpha_1, \alpha_2 < 2$) are summarized in Table 5.1.

	$1 < \alpha_1 < \alpha_2 < 2$	$1 < \alpha_2 < \alpha_1 < 2$	$1 < \alpha_2 = \alpha_1 < 2$
$h = 1$	$S_{\nu,L} = \mathcal{O}(1)$	$S_{\nu,L} \approx \frac{\nu+1}{12\nu} \ln L$	$S_{\nu,L} \approx B_{\nu,\alpha} \ln L$
$h = -1 + 2^{1-\alpha_1}$	$S_{\nu,L} \approx \frac{\nu+1}{12\nu} \ln L$	$S_{\nu,L} \approx \frac{\nu+1}{12\nu} \ln L$	$S_{\nu,L} \approx \frac{\nu+1}{12\nu} \ln L$

Table 5.1: Summary of entanglement scaling results at different quantum critical points and for various values of α_1 and α_2 in the weak long-range regime. The symbol \approx denotes equality up to subleading $\mathcal{O}(1)$ corrections.

5.4 Entanglement scaling in the strong long-range regime

The scenario in the strong long-range regime is more complex. Previous studies on fermionic systems with strong long-range pairing interactions [97, 282, 283] have reported logarithmic violations of the entanglement area law even when the system is not at criticality. In those cases, the noncritical logarithmic scaling of the ground state entanglement was linked to divergences in the long-range couplings, as no Kac scaling was introduced in the model Hamiltonian. This led to the belief that such anomalous scalings were trivially related to the loss of system extensivity.

However, as shown in Section 1.5, introducing the Kac normalization into the Hamiltonian allows for the definition of a model with strong long-range interactions while still preserving energy extensivity. In particular, when the Kac scaling is introduced, the coupling divergences for $\alpha_1, \alpha_2 < 1$ are canceled, and the associated symbol discontinuities are eliminated. However, an infinite number of new nontrivial discontinuities arise due to the fact that the spectrum becomes discrete also in the thermodynamic limit. Specifically, the symbol G_k becomes formally discontinuous at each $k = 2\pi n/N$. Indeed, in the thermodynamic limit, G_k is given by

$$\lim_{N \rightarrow \infty} G_k = G_n = \frac{2(h - \tilde{t}_n)}{\omega_n} \sigma_z - \frac{2\tilde{\Delta}_n}{\omega_n} \sigma_y. \quad (5.55)$$

Then it can be labeled by a discrete integer number n , while the k variable becomes continuous. In practical terms, any real physical implementation of the model is finite. Therefore, the continuum limit as $N \rightarrow \infty$ implies that the difference between two consecutive k values is $\mathcal{O}(N^{-1})$. In the strong long-range case, this difference leads to a finite jump in the spectrum ω_n , which remains discrete in the thermodynamic limit, resulting in a discontinuity of the matrix symbol G_k for any k , irrespective of the chemical potential h .

For any $\alpha_{1,2} > 0$ or $\alpha_1 = \alpha_2 = 0$ with $h \neq 0$, the many-body ground state remains the Bogoliubov vacuum. Thus, the lateral limits corresponding to $k^\pm = 2\pi n/N, 2\pi(n+1)/N$ are

$$G_k^\pm = \begin{cases} G_{n+1} = \cos \phi_{n+1} \sigma_z + \sin \phi_{n+1} \sigma_y \\ G_n = \cos \phi_n \sigma_z + \sin \phi_n \sigma_y \end{cases}, \quad (5.56)$$

where the angles ϕ_n are defined by

$$\cos \phi_n = \frac{2(h - \tilde{t}_n)}{\omega_n}, \quad \sin \phi_n = \frac{-2\tilde{\Delta}_n}{\omega_n}. \quad (5.57)$$

Following the analytic procedure introduced in Section 5.2.4, we derive the logarithmic scaling of the ground state Rényi entropies for any value of h :

$$S_{\nu,L} = B_\nu(h) \ln L + \mathcal{O}(1), \quad (5.58)$$

where the coefficient $B_\nu(h)$ depends on ν , α_1 , α_2 , and h . This coefficient is the sum of contributions from N discontinuities of the symbol, expressed as

$$B_\nu(h) = \sum_{n=-N/2+1}^{N/2} B_\nu^{(n)}(h), \quad (5.59)$$

with each contribution $B_\nu^{(n)}(h)$ derived using Eq. (5.28), and reading

$$B_\nu^{(n)}(h) = \frac{1}{\pi^2(\nu-1)} \sum_{l=1}^{\nu} \arctan^2 \left[\frac{\sin((\phi_{n+1} - \phi_n)/2)}{\sqrt{\cos^2((\phi_{n+1} - \phi_n)/2) + |z_l|^2}} \right]. \quad (5.60)$$

where $|z_l|^2 = \tan^2(\pi(2l-1)/2\nu)$, with $l = 1, \dots, \nu$ and $l \neq (1+\nu)/2$. Specifically, for $\nu = 2$, the sum simplifies to

$$B_2^{(n)}(h) = \frac{2}{\pi^2} \left[\arctan \sqrt{\frac{\omega_{n+1}\omega_n - (h - \tilde{t}_{n+1})(h - \tilde{t}_n) - \tilde{\Delta}_{n+1}\tilde{\Delta}_n}{3\omega_{n+1}\omega_n + (h - \tilde{t}_{n+1})(h - \tilde{t}_n) + \tilde{\Delta}_{n+1}\tilde{\Delta}_n}} \right]^2. \quad (5.61)$$

The most interesting scenario arises when the hopping and pairing amplitudes are equally long-range, i.e., when $\alpha_1 = \alpha_2 = \alpha$, while we expect only minor differences to appear when $\alpha_1 \neq \alpha_2$, as long as they are both smaller than the system dimension (here $d = 1$). Thus, for simplicity, we will focus on the case $\alpha_1 = \alpha_2 = \alpha$ in our analysis of the strong long-range regime.

Figure 5.6(a) illustrates $B_2(h)$ as a function of the chemical potential h for different values of $\alpha_1 = \alpha_2 = \alpha$. Notably, for any non-zero value of the chemical potential ($h \neq 0$) and any positive α , the scaling coefficient remains $B_2(h \neq 0) = \mathcal{O}(1)$, indicating a logarithmic violation of the area law even away from the quantum critical points. Additionally, two singularities appear at the quantum critical points $h = \tilde{t}_0, \tilde{t}_\pi = 1, 0$. Specifically, there is a discontinuity at $h = 1$ and a divergence with subsystem size at $h = 0$, resulting in a subvolume law entanglement scaling.

These facts can be understood as follows. The spectrum is labeled by the discrete index n leading to a finite gap between the ground state and the first excited levels which

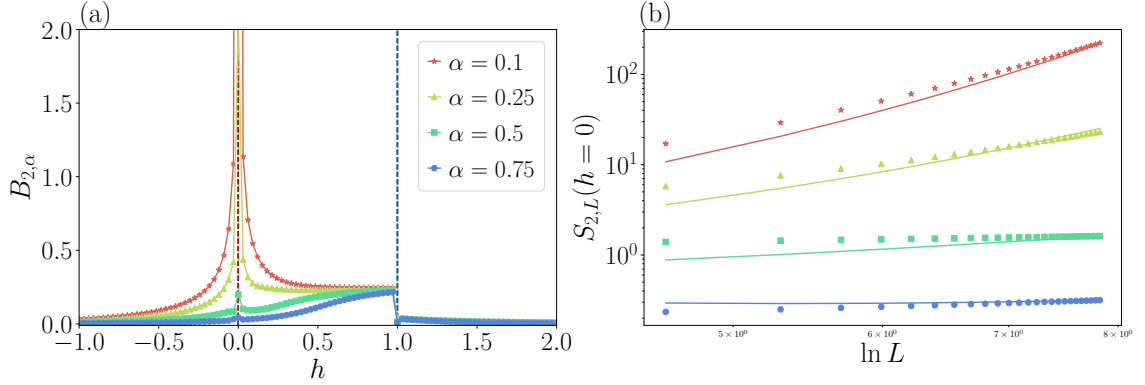


Figure 5.6: a) Rényi-2 scaling coefficient $B_{2,\alpha}$ as a function of the chemical potential h for different values of the power law decay coefficient $0 < \alpha = \alpha_1 = \alpha_2 < 1$. The red and blue vertical lines correspond to the $h = 1$ and $h = 0$ critical points, respectively. b) Numerical check for the entanglement subvolume law scaling at $h = 0$ for different values of $0 < \alpha < 1$, plotted as a function of the logarithm of the subsystem size $\ln L$. Scattered points correspond to the numerical data while solid lines represent our prediction $B_{2,\alpha} \ln L$.

are associated with discontinuities of the symbol. However, for $n \gg 1$ all the modes accumulate around $\omega_\infty = 2|h|$. This means that an extensive number of single-particle states is almost degenerate. Consequently, as long as $h \neq 0$, we may expect only the first few modes around $n = 0$ to provide a significant contribution to the symbol discontinuity leading to a coefficient $B_\nu(h \neq 0) = \mathcal{O}(1)$. Accordingly, we may expect many features of the entanglement scaling coefficients for values of the chemical potential sufficiently far from the $h = 0$ point, to be qualitatively reproduced by considering a single discontinuity approximation in which only the first discontinuity between the $n = 0$ and the first two degenerate levels $n = \pm 1$ is considered,

$$B_\nu(h \neq 0) \approx B_\nu^{(0)} + B_\nu^{(-1)}. \quad (5.62)$$

To compute these contributions, we need to determine the angles ϕ_0 and $\phi_{\pm 1}$ as defined by the conditions in Eq.(5.57). For $n = 0$ we find that, regardless of α , the angle is given by

$$\cos \phi_0 = \begin{cases} -1 & \text{if } h < 1 \\ 0 & \text{if } h > 1 \end{cases}, \quad \phi_0 = \begin{cases} \pi & \text{if } h < 1 \\ 0 & \text{if } h > 1. \end{cases} \quad (5.63)$$

The discontinuity at the quantum critical point $h = 1$ is due to the fact that at this point the spectrum becomes gapless for $n = 0$, which is the source of the discontinuity in the scaling coefficient observed in Fig. 5.6(a). Although the angles for $n = \pm 1$ cannot be computed exactly in closed form for a generic power law decay exponent, the properties

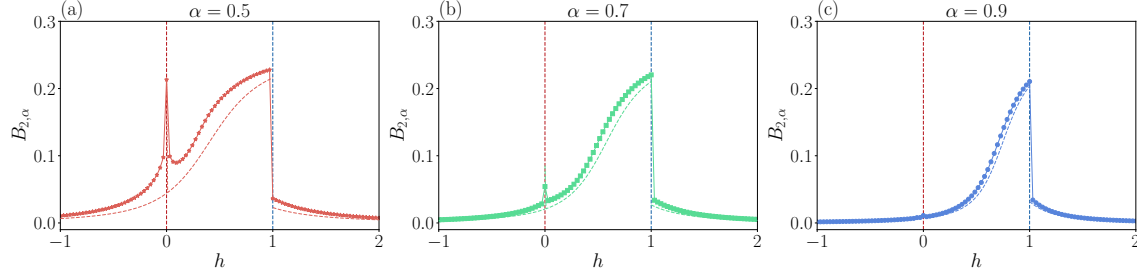


Figure 5.7: Comparison between the exact values of the logarithmic scaling coefficients of the Rényi-2 entropy, and the single discontinuity approximation (dashed lines) results. The coefficients are plotted as function of the chemical potential h for different values of the decay exponent α .

$\tilde{t}_n = \tilde{t}_{-n}$, $\omega_n = \omega_{-n}$ while $\tilde{\Delta}_n = -\tilde{\Delta}_{-n}$ imply that

$$\cos \phi_n = \cos \phi_{-n} \quad \sin \phi_n = -\sin \phi_{-n}, \quad (5.64)$$

leading to $\phi_n = -\phi_{-n}$. Using these properties in Eq. (5.60), we get

$$B_\nu^{(0)} = B_\nu^{(-1)} = \frac{1}{\pi^2(\nu-1)} \sum_{l=1}^{\nu} \arctan^2 \left[\frac{\cos(\phi_1/2)}{1 + \sin^2(\phi_1/2)} \right] \quad \text{if } h < 1, \quad (5.65)$$

$$B_\nu^{(0)} = B_\nu^{(-1)} = \frac{1}{\pi^2(\nu-1)} \sum_{l=1}^{\nu} \arctan^2 \left[\frac{\sin(\phi_1/2)}{1 + \cos^2(\phi_1/2)} \right] \quad \text{if } h > 1. \quad (5.66)$$

Figure 5.7 presents a comparison between the exact logarithmic scaling coefficients of the Rényi-2 entropy B_2 , calculated by incorporating contributions from a formally extensive number of discontinuities (see Eq. (5.60)), and those obtained using the single discontinuity approximation. The single discontinuity approximation accurately captures the qualitative behavior of the scaling coefficients for sufficiently high values of $\alpha > 0.5$ and for chemical potential values h which are sufficiently far from $h = 0$. Notably, the approximation successfully identifies the discontinuity of the coefficients at the quantum critical point $h = 1$.

On the other hand, when the chemical potential approaches the $h \rightarrow 0$ limit and for sufficiently small decay exponents $\alpha < 1/2$, the single discontinuity approximation becomes inaccurate. In this scenario, the number of relevant discontinuities increases with the subsystem size, leading to a subvolume law entanglement scaling. This phenomenon can be understood by examining the $h = 0$ point. In this case, the spectrum accumulation point becomes $\omega_\infty = 0$. Notably, while at leading order as $n \rightarrow \infty$ the spectrum goes to zero as $\omega_n = \mathcal{O}(n^{\alpha-1})$, regardless of mode parity, the next-to-leading order corrections vary depending on whether n is even or odd. By performing a next-to-leading order expansion

of the terms in $B_2^{(m)}$ (see Eq. (5.61)), which corresponds to the discontinuity between the modes $m = 2n$ and $m + 1 = 2n + 1$, we find

$$\tilde{t}_{2n+1}\tilde{t}_{2n} = \frac{s_\alpha^2}{n^{2-2\alpha}} + \mathcal{O}(n^{2\alpha-3}), \quad (5.67)$$

$$\tilde{\Delta}_{2n+1}\tilde{\Delta}_{2n} = \frac{c_\alpha^2}{n^{2-2\alpha}} - \frac{a_\alpha^2}{n^2} + \mathcal{O}(n^{2\alpha-3}), \quad (5.68)$$

$$\omega_{2n+1}\omega_{2n} = \frac{s_\alpha^2 + c_\alpha^2}{n^{2-2\alpha}} + \frac{b_\alpha}{n^2} + \mathcal{O}(n^{2\alpha-3}), \quad (5.69)$$

where we have introduced the expansion coefficients

$$\begin{aligned} s_\alpha &= \sin(\alpha\pi/2)\Gamma(2-\alpha)(2\pi)^{\alpha-1}, \\ c_\alpha &= \cos(\alpha\pi/2)\Gamma(2-\alpha)(2\pi)^{\alpha-1}, \\ a_\alpha &= (1-\alpha)/(2\pi), \\ b_\alpha &= a_\alpha^2(1/2 - \cos^2(\alpha\pi/2)) = a_\alpha^2 \cos(\alpha\pi)/2. \end{aligned} \quad (5.70)$$

Now, inserting the large n expansions of Eqs. (5.67), (5.68) and (5.69) into Eq. (5.61), we see that the denominator is of order $\mathcal{O}(n^{2\alpha-2})$, while in the numerator the leading order cancels out and we are left with a contribution of order $\mathcal{O}(n^{-2})$ if $\alpha < 1/2$ or $\mathcal{O}(n^{2\alpha-3})$ if $\alpha > 1/2$. Finally, summing over all modes, we obtain

$$B_\nu(h=0) = \sum_n B_\nu^{(n)} = \begin{cases} \sum_n \mathcal{O}(n^{-2\alpha}) = \mathcal{O}(L^{1-2\alpha}) & \alpha < 1/2 \\ \sum_n \mathcal{O}(n^{-1}) = \mathcal{O}(1) & \alpha > 1/2 \end{cases}. \quad (5.71)$$

Accordingly, the leading order contribution to the entanglement Rényi entropy of the system ground state at zero chemical potential takes the nontrivial form

$$S_{\nu,L}(h=0) = \begin{cases} \mathcal{O}(L^{1-2\alpha} \ln L) & \text{if } \alpha < 1/2 \\ \mathcal{O}(\ln L) & \text{if } \alpha > 1/2 \end{cases}. \quad (5.72)$$

This analytic result matches numerical data in the large L limit. This is illustrated in Fig. 5.6(b), where the numerical and analytical results for $S_{2,L}$ are plotted as functions of $\ln L$ for different values of α . It is important to notice that approaching the thermodynamic limit in the $h = 0$ case the spectrum becomes increasingly more degenerate approaching the $\alpha = 0$ case. Thus, for each finite N , there exists a large number of states nearly degenerate with the ground state, making the estimation of subleading correction scaling technically challenging.

Finally, in the mean-field case where $\alpha_1 = \alpha_2 = 0$ with zero chemical potential $h = 0$ the quasiparticle spectrum exhibits an extensive number of degenerate zero modes $\omega_n = 0$ corresponding to all even modes with $n = 2m$. As a result, the ground state features a finite fermionic population in these even modes $f_{2m} \neq 0$. The leading order term in the

entanglement scaling for this case is given by the first term of the Fisher-Hartwig expansion, which corresponds to the volume law

$$S_{\nu,L}(\alpha = 0, h = 0) = \frac{1}{1 - \nu} \sum_{n(\text{even})} \ln[(1 - f_n)^\nu + f_n^\nu] + \mathcal{O}(\ln L). \quad (5.73)$$

The maximal Rényi entropy is achieved when $f_n = 1/2$ for all even n . In this case, the logarithmic corrections become zero since in Eq. (5.28) $a_n = b_n = 0$, and therefore $B_\nu^{(n)}(f_n = 1/2) = 0$, while the volume law term simplifies to

$$S_{\nu,L}^{\max}(\alpha = 0, h = 0) = N_0 \ln 2 + \mathcal{O}(1) = \frac{L}{2} \ln 2 + \mathcal{O}(1), \quad (5.74)$$

where N_0 is the number of zero modes, which in this case corresponds to the number of even modes $N_0 \simeq L/2$ and the subleading corrections are at most of order $\mathcal{O}(1)$. It is noteworthy that the maximal Rényi entropy obtained via the Fisher-Hartwig expansion corresponds to the maximum possible entropy allowed by the ground state degeneracy

$$S_{\nu,L}^{\max}(\alpha = 0, h = 0) = \ln \text{Deg}[|\text{gs}_{\alpha=0, h=0}\rangle] = N_0 \ln 2. \quad (5.75)$$

This indicates that the Fisher-Hartwig result, derived as a large subsystem size expansion, becomes exact in this maximally entangled case.

The results for the entanglement scaling with subsystem size for different values of h and $\alpha = \alpha_1 = \alpha_2$ within the strong long-range regime ($0 < \alpha < 1$) are summarized in Table 5.2.

	$\alpha = 0$	$0 < \alpha < 1/2$	$1/2 < \alpha < 1$
$h \neq 0$	$S_{\nu,L} = \mathcal{O}(\ln L)$	$S_{\nu,L} = \mathcal{O}(\ln L)$	$S_{\nu,L} = \mathcal{O}(\ln L)$
$h = 0$	$S_{\nu,L} = \mathcal{O}(L)$	$S_{\nu,L} = \mathcal{O}(L^{1-2\alpha} \ln L)$	$S_{\nu,L} = \mathcal{O}(\ln L)$

Table 5.2: Summary of entanglement scaling results at different quantum critical points and for various values of $\alpha = \alpha_1 = \alpha_2$ in the strong long-range regime.

5.5 Closing remarks

In this Chapter, we have extended the understanding of the peculiar properties of entanglement in quantum systems featuring long-range interactions. Specifically, we investigated the ground state entanglement scaling of a spinless fermionic chain with long-range hopping and pairing amplitudes. The simplicity of this model and its non-additive nature allowed us to unveil a rich and non-trivial phenomenology, characterized both numerically and

analytically across different parameter regimes, notably the power-law decay exponents of the hopping and pairing couplings (α_1, α_2) and the chemical potential (h).

We identified two main regimes: the weak long-range regime ($1 < \alpha_1, \alpha_2 < 2$) and the strong long-range regime ($0 < \alpha_1, \alpha_2 < 1$). In the weak long-range regime, the quasiparticle spectrum becomes continuous in the thermodynamic limit, with non-local couplings modifying the dispersion relation near gapless critical modes. Here, the standard area law for entanglement scaling is satisfied, apart from logarithmic violations at quantum critical points $h = 1$ and $h = -1 + 2^{1-\alpha_1}$. These logarithmic scalings are linked to discontinuities in the symbol of the block Toeplitz correlation matrix, allowing for exact computation of their coefficients. Notably, when $\alpha_1 = \alpha_2 = \alpha$, the coefficient of the critical logarithmic divergence at $h = 1$ exhibits a non-trivial dependence on α .

This coefficient, $B_{\nu, \alpha}$, is non-universal, stemming from the spectrum precise form near the critical modes rather than solely from the dispersion relation power-law exponent. Consequently, the critical entanglement scaling deviates from conformal field theory predictions, highlighting that long-range couplings break conformal symmetry at criticality.

For $\alpha_1 \neq \alpha_2$, the critical entanglement scaling becomes α -independent. When $\alpha_1 > \alpha_2$, with pairing coupling decaying slower than hopping, the entanglement scaling matches that of a conformal field theory with central charge $c = 1/2$, consistent with previous results for long-range pairing and nearest-neighbor hopping Kitaev chains, now extended to any long-range hopping with $\alpha_1 > \alpha_2$. The anisotropy between dominating hopping ($\alpha_1 < \alpha_2$) and dominating pairing ($\alpha_1 > \alpha_2$) is a characteristic of the long-range Kitaev chain.

In the strong long-range regime, the quasiparticle spectrum is no longer continuous in the thermodynamic limit, and the block Toeplitz correlation matrix symbol becomes discontinuous across the spectrum. Nevertheless, only a few discontinuities significantly contribute to the entanglement scaling, leading to a logarithmic dependence on subsystem size even outside criticality. These coefficients were computed analytically for various $\alpha_{1,2}$ and h values.

The most intriguing scenario occurs at zero chemical potential ($h = 0$) in the strong long-range regime, where the coefficient in front of the critical logarithmic entanglement scaling diverges as a power law of the subsystem size, resulting in a fractal subvolume-law entanglement scaling ($S_{\nu, L} \approx L^{1-2\alpha} \ln L$ for $0 < \alpha = \alpha_1 = \alpha_2 < 1/2$ and $\nu > 1$). This phenomenon, observed in other complex scenarios, arises here naturally at equilibrium but requires stronger interactions compared to the dynamical case.

In the mean-field case $\alpha = 0$, the system presents an extensive number of degenerate zero energy modes, leading to an exponentially growing ground state degeneracy and volume law behavior in entanglement scaling ($S_{\nu, L}(\alpha = 0) \approx L$).

Our findings demonstrate that long-range couplings significantly enhance entanglement scaling at equilibrium, positioning long-range interacting quantum systems as promising candidates for robust quantum computation. However, these enhanced entanglement properties might not persist out-of-equilibrium, as long-range interactions can suppress the dynamical spread of entanglement in certain systems.

These insights pave the way for future research into the equilibrium and dynamical properties of long-range interacting quantum systems, offering a deeper understanding of their potential for quantum technological applications.

Chapter 6

Conclusions and outlooks

While each chapter of this thesis presents specific conclusions related to the topics addressed, this final section provides a brief summary of the main results and a more general overview of potential areas for further research.

The core focus of this thesis has been the study of the unique properties of long-range interacting quantum systems, both in and out of equilibrium. The results presented here demonstrate multiple ways in which long-range interactions can be harnessed for quantum technological applications. The key advantages of long-range systems include their ability to evade thermalization and create stable out-of-equilibrium states, their resilience to defect generation during finite-time external driving, and their collective nature, which facilitates the generation of high amount of entanglement. These features collectively have the potential to mitigate the costs of quantum control, reduce energy losses, and preserve locally stored quantum information during dynamic processes, such as quantum simulations or quantum algorithms.

In Chapter 3, we explored the potential advantages of long-range interactions in the context of quantum thermodynamics. By analyzing the universal properties of quantum work statistics in driven long-range systems, we identified conditions under which long-range interactions reduce energy losses during non-adiabatic evolution. This is crucial for enhancing the efficiency and power output of quantum heat engines, especially in finite-time thermal cycles.

We considered two limiting scenarios: sudden and slow driving protocols. In the sudden quench scenario, we mapped the work statistics in a quantum system to a classical problem in a higher effective dimension. This revealed that long-range interactions significantly decrease the irreversible work done during rapid quenches. For slow driving protocols, we studied the scaling behavior of the cumulants of the work distribution with respect to the driving velocity v in the $v \rightarrow 0$ limit, showing that long-range systems exhibit a distinct advantage in reducing non-adiabatic excitations over a broad range of interaction exponents α .

We also investigated the performance of a quantum thermal machine consisting of a chain of fermions with power-law decaying interactions undergoing a quantum Otto cycle. We provided a detailed characterization of the device, detecting several sources of long-range advantage compared to the nearest-neighbor case in the two most useful operation modes for quantum technological applications: the heat-engine and the refrigerator modes.

In Chapter 4, we examined the potential of long-range interactions to stabilize out-of-equilibrium phases. Specifically, we focused on Floquet-driven many-body quantum systems and the stabilization of Discrete Floquet Time Crystals (DFTCs).

The first part of Chapter 4 introduced a novel order parameter ζ capable of unambiguously detecting higher-order DFTCs in clean long-range systems. We used this parameter to derive a new out-of-equilibrium phase diagram for the kicked long-range Ising model, featuring self-similar structures with non-integer, fractal dimensions.

In the second part of Chapter 4, we investigated the potential of superconducting quantum hardware to simulate the dynamics of systems with couplings beyond nearest neighbors. Leveraging the universality of native gates in quantum processors, we successfully implemented couplings among physically disconnected qubits and mitigated the effects of gate noise, measurement errors, and statistical errors. This allowed us to benchmark the stabilization discrete Floquet time-crystalline response in a periodically driven quantum spin chain as the interaction range increased, using IBM superconducting processors.

Finally, in Chapter 5, we explored the potential of quantum Hamiltonians with long-range couplings to host highly entangled ground states, overcoming the limitations imposed by the entanglement area law for local systems.

Specifically, we investigated the ground state entanglement scaling of a spinless fermionic chain with long-range hopping and pairing amplitudes, unveiling a rich phenomenology. In the weak long-range regime, the standard area law for entanglement scaling is satisfied, with logarithmic violations at quantum critical points $h = 1$ and $h = -1 + 2^{1-\alpha_1}$. Notably, when $\alpha_1 = \alpha_2 = \alpha$, the coefficient of the critical logarithmic divergence at $h = 1$ exhibits a non-trivial dependence on α , which is not compatible with results obtained from any conformal field theory, highlighting that long-range couplings explicitly break critical conformal symmetry.

In the strong long-range regime, we observed logarithmic entanglement scaling even outside criticality for every $h \neq 0$. The most intriguing scenario occurs at zero chemical potential ($h = 0$) where the coefficient in front of the critical logarithmic entanglement scaling diverges as a power law of the subsystem size, resulting in a subvolume-law entanglement scaling.

In the mean-field case $\alpha = 0$, the system presents an extensive number of degenerate zero energy modes, leading to an exponentially growing ground state degeneracy and a volume law behavior in entanglement scaling.

Given the findings presented in this thesis, and the fact that many atomic, molecular, and optical (AMO) platforms, the most promising candidates for quantum computing, naturally exhibit long-range couplings, a critical question arises: Are we fully harnessing

the potential of existing quantum processors? Considering that these processors inherently support long-range couplings, it is worth exploring whether quantum algorithms that explicitly incorporate and exploit this property could significantly reduce the required number of qubits. Despite their instrumental role in the achievements of current quantum processors, long-range interactions have yet to be fully leveraged in the design of quantum algorithms and simulations. This untapped potential offers a unique opportunity for innovation and advancement in the field. For example, in the context of search algorithms, long-range quantum walks are known to boost search times. However, many open questions remain regarding the advantages of long-range couplings in such setups, necessitating deeper investigation. Furthermore, the presence of long-range couplings could prove beneficial for generic quantum control tasks, such as quantum state preparation. The enhanced robustness against non-adiabatic transitions and defect generation may enable faster state preparation while maintaining high fidelity with the target state.

In conclusion, the work collected in this thesis highlights the significant potential of long-range interacting quantum systems and opens up numerous avenues for future research. We hope that these findings will inspire further investigations in this fascinating field, ultimately contributing to the advancement of quantum technologies.

Bibliography

- [1] Andrea Solfanelli and Nicolò Defenu. Universality in long-range interacting systems: the effective dimension approach. *arXiv:2406.14651*, 2024.
- [2] Andrea Solfanelli and Nicolò Defenu. Universal work statistics in long-range interacting quantum systems. *arXiv:2407.04101*, 2024.
- [3] Andrea Solfanelli, Guido Giachetti, Michele Campisi, Stefano Ruffo, and Nicolò Defenu. Quantum heat engine with long-range advantages. *New Journal of Physics*, 25(3):033030, mar 2023.
- [4] Guido Giachetti, Andrea Solfanelli, Lorenzo Correale, and Nicolò Defenu. Fractal nature of high-order time crystal phases. *Phys. Rev. B*, 108:L140102, Oct 2023.
- [5] Andrea Solfanelli, Stefano Ruffo, Sauro Succi, and Nicolò Defenu. Stabilization of discrete time-crystalline response on a superconducting quantum computer by increasing the interaction range. *Phys. Rev. Res.*, 6:013311, Mar 2024.
- [6] Andrea Solfanelli, Stefano Ruffo, Sauro Succi, and Nicolò Defenu. Logarithmic, fractal and volume-law entanglement in a kitaev chain with long-range hopping and pairing. *Journal of High Energy Physics*, 2023(5):66, May 2023.
- [7] Alessandro Santini, Andrea Solfanelli, Stefano Gherardini, and Mario Collura. Work statistics, quantum signatures, and enhanced work extraction in quadratic fermionic models. *Phys. Rev. B*, 108:104308, Sep 2023.
- [8] Alessandro Santini, Andrea Solfanelli, Stefano Gherardini, and Guido Giachetti. Observation of partial and infinite-temperature thermalization induced by repeated measurements on a quantum hardware. *Journal of Physics Communications*, 7(6):065007, jun 2023.
- [9] Alio Issoufou Arzika, Andrea Solfanelli, Harald Schmid, and Stefano Ruffo. Quantization of integrable and chaotic three-particle fermi–pasta–ulam–tsingou models. *Entropy*, 25(3), 2023.

- [10] Harald Schmid, Johannes Dieplinger, Andrea Solfanelli, Sauro Succi, and Stefano Ruffo. Tricritical point in the quantum hamiltonian mean-field model. *Phys. Rev. E*, 106:024109, Aug 2022.
- [11] Andrea Solfanelli, Alessandro Santini, and Michele Campisi. Quantum thermodynamic methods to purify a qubit on a quantum processing unit. *AVS Quantum Science*, 4(2):026802, 06 2022.
- [12] Andrea Solfanelli, Alessandro Santini, and Michele Campisi. Experimental verification of fluctuation relations with a quantum computer. *PRX Quantum*, 2:030353, Sep 2021.
- [13] Andrea Solfanelli, Marco Falsetti, and Michele Campisi. Nonadiabatic single-qubit quantum otto engine. *Phys. Rev. B*, 101:054513, Feb 2020.
- [14] Andrea Solfanelli, Lorenzo Buffoni, Alessandro Cuccoli, and Michele Campisi. Maximal energy extraction via quantum measurement. *Journal of Statistical Mechanics: Theory and Experiment*, 2019(9):094003, sep 2019.
- [15] Lorenzo Buffoni, Andrea Solfanelli, Paola Verrucchi, Alessandro Cuccoli, and Michele Campisi. Quantum measurement cooling. *Phys. Rev. Lett.*, 122:070603, Feb 2019.
- [16] Nicolò Defenu, Tobias Donner, Tommaso Macrì, Guido Pagano, Stefano Ruffo, and Andrea Trombettoni. Long-range interacting quantum systems. *Rev. Mod. Phys.*, 95:035002, Aug 2023.
- [17] M. Saffman, T. G. Walker, and K. Mølmer. Quantum information with Rydberg atoms. *Rev. Mod. Phys.*, 82(3):2313–2363, August 2010.
- [18] T. Lahaye, C. Menotti, L. Santos, M. Lewenstein, and T. Pfau. The physics of dipolar bosonic quantum gases. *Rep. Prog. Phys.*, 72(12):126401, November 2009.
- [19] Lincoln D Carr, David DeMille, Roman V Krems, and Jun Ye. Cold and ultracold molecules: science, technology and applications. *New J. Phys.*, 11(5):055049, May 2009.
- [20] Helmut Ritsch, Peter Domokos, Ferdinand Brennecke, and Tilman Esslinger. Cold atoms in cavity-generated dynamical optical potentials. *Rev. Mod. Phys.*, 85(2):553–601, April 2013.
- [21] Tobias Donner Farokh Mivehvar, Francesco Piazza and Helmut Ritsch. Cavity qed with quantum gases: new paradigms in many-body physics. *Advances in Physics*, 70(1):1–153, 2021.
- [22] Ch Schneider, Diego Porras, and Tobias Schaetz. Experimental quantum simulations of many-body physics with trapped ions. *Rep. Prog. Phys.*, 75(2), 2012.

- [23] R Blatt and C F Roos. Quantum simulations with trapped ions. *Nat. Phys.*, 8(4):277–284, April 2012.
- [24] C. Monroe, W. C. Campbell, L.-M. Duan, Z.-X. Gong, A. V. Gorshkov, P. W. Hess, R. Islam, K. Kim, N. M. Linke, G. Pagano, P. Richerme, C. Senko, and N. Y. Yao. Programmable quantum simulations of spin systems with trapped ions. *Rev. Mod. Phys.*, 93:025001, Apr 2021.
- [25] Richard Jozsa and Noah Linden. On the role of entanglement in quantum-computational speed-up. *Proc. R. Soc. Lond. A*, 459(2036):2011–2032, Aug 2003.
- [26] Minghua Pan, Daowen Qiu, Paulo Mateus, and Jozef Gruska. Entangling and disentangling in grover’s search algorithm. *Theoretical Computer Science*, 773:138–152, 2019.
- [27] Laszlo Gyongyosi and Sandor Imre. A survey on quantum computing technology. *Computer Science Review*, 31:51–71, 2019.
- [28] M. Kac, G. E. Uhlenbeck, and P. C. Hemmer. On the van der Waals Theory of the Vapor-Liquid Equilibrium. I. Discussion of a One-Dimensional Model. *Journal of Mathematical Physics*, 4(2):216–228, February 1963.
- [29] Alessandro Campa, Thierry Dauxois, and Stefano Ruffo. Statistical mechanics and dynamics of solvable models with long-range interactions. *Phys. Rep.*, 480(3-6):57–159, September 2009.
- [30] A Campa, Thierry Dauxois, D Fanelli, and S Ruffo. *Physics of Long-Range Interacting Systems*. Oxford Univ. Press, 2014.
- [31] Amit Dutta and J. K. Bhattacharjee. Phase transitions in the quantum ising and rotor models with a long-range interaction. *Phys. Rev. B*, 64:184106, Oct 2001.
- [32] Mohammad F. Maghrebi, Zhe-Xuan Gong, Michael Foss-Feig, and Alexey V. Gorshkov. Causality and quantum criticality in long-range lattice models. *Phys. Rev. B*, 93:125128, Mar 2016.
- [33] Nicolò Defenu, Andrea Trombettoni, and Stefano Ruffo. Criticality and phase diagram of quantum long-range $o(n)$ models. *Phys. Rev. B*, 96:104432, Sep 2017.
- [34] Nicolò Defenu, Alessandro Codello, Stefano Ruffo, and Andrea Trombettoni. Criticality of spin systems with weak long-range interactions. *J. Phys. A Math. Gen.*, 53(14):143001, April 2020.
- [35] A. Messiah. *Quantum Mechanics*. Number v. 1 in Quantum Mechanics. North-Holland Publishing Company, 1961.

- [36] Nicolò Defenu, Giovanna Morigi, Luca Dell'Anna, and Tilman Enss. Universal dynamical scaling of long-range topological superconductors. *Phys. Rev. B*, 100:184306, Nov 2019.
- [37] M. Abramowitz and I.A. Stegun. *Handbook of Mathematical Functions: With Formulas, Graphs, and Mathematical Tables*. Applied mathematics series. Dover Publications, 1965.
- [38] Giacomo Bighin, Tilman Enss, and Nicolò Defenu. Universal scaling in real dimension. *Nature Communications*, 15(1):4207, May 2024.
- [39] Kumiko Hattori, Tetsuya Hattori, and Hiroshi Watanabe. Gaussian field theories on general networks and the spectral dimensions. *Progress of Theoretical Physics Supplement*, 92:108–143, 1987.
- [40] Yoram Last. Quantum dynamics and decompositions of singular continuous spectra. *Journal of Functional Analysis*, 142(2):406–445, 1996.
- [41] David Mukamel. Notes on the statistical mechanics of systems with long-range interactions, 2009.
- [42] N. D. Mermin and H. Wagner. Absence of ferromagnetism or antiferromagnetism in one- or two-dimensional isotropic heisenberg models. *Phys. Rev. Lett.*, 17:1133–1136, Nov 1966.
- [43] Michael E. Fisher, Shang-keng Ma, and B. G. Nickel. Critical exponents for long-range interactions. *Phys. Rev. Lett.*, 29:917–920, Oct 1972.
- [44] Cheng Chen, Guillaume Bornet, Marcus Bintz, Gabriel Emperauger, Lucas Leclerc, Vincent S. Liu, Pascal Scholl, Daniel Barredo, Johannes Hauschild, Shubhayu Chatterjee, Michael Schuler, Andreas M. Läuchli, Michael P. Zaletel, Thierry Lahaye, Norman Y. Yao, and Antoine Browaeys. Continuous symmetry breaking in a two-dimensional rydberg array. *Nature*, 616(7958):691–695, 2023.
- [45] Lei Feng, Or Katz, Casey Haack, Mohammad Maghrebi, Alexey V. Gorshkov, Zhexuan Gong, Marko Cetina, and Christopher Monroe. Continuous symmetry breaking in a trapped-ion spin chain. *Nature*, 623(7988):713–717, 2023.
- [46] Maria Chiara Angelini, Giorgio Parisi, and Federico Ricci-Tersenghi. Relations between short-range and long-range ising models. *Phys. Rev. E*, 89:062120, Jun 2014.
- [47] David P. DiVincenzo. The physical implementation of quantum computation. *Fortschritte der Physik*, 48(9-11):771–783, 2000.

- [48] Frank Arute, Kunal Arya, Ryan Babbush, Dave Bacon, Joseph C. Bardin, Rami Barends, Rupak Biswas, Sergio Boixo, Fernando G. S. L. Brandao, David A. Buell, Brian Burkett, Yu Chen, Zijun Chen, Ben Chiaro, Roberto Collins, William Courtney, Andrew Dunsworth, Edward Farhi, Brooks Foxen, Austin Fowler, Craig Gidney, Marissa Giustina, Rob Graff, Keith Guerin, Steve Habegger, Matthew P. Harrigan, Michael J. Hartmann, Alan Ho, Markus Hoffmann, Trent Huang, Travis S. Humble, Sergei V. Isakov, Evan Jeffrey, Zhang Jiang, Dvir Kafri, Kostyantyn Kechedzhi, Julian Kelly, Paul V. Klimov, Sergey Knysh, Alexander Korotkov, Fedor Kostritsa, David Landhuis, Mike Lindmark, Erik Lucero, Dmitry Lyakh, Salvatore Mandrà, Jarrod R. McClean, Matthew McEwen, Anthony Megrant, Xiao Mi, Kristel Michielsen, Masoud Mohseni, Josh Mutus, Ofer Naaman, Matthew Neeley, Charles Neill, Murphy Yuezhen Niu, Eric Ostby, Andre Petukhov, John C. Platt, Chris Quintana, Eleanor G. Rieffel, Pedram Roushan, Nicholas C. Rubin, Daniel Sank, Kevin J. Satzinger, Vadim Smelyanskiy, Kevin J. Sung, Matthew D. Trevithick, Amit Vainsencher, Benjamin Villalonga, Theodore White, Z. Jamie Yao, Ping Yeh, Adam Zalcman, Hartmut Neven, and John M. Martinis. Quantum supremacy using a programmable superconducting processor. *Nature*, 574(7779):505–510, Oct 2019.
- [49] Yulin Wu, Wan-Su Bao, Sirui Cao, Fusheng Chen, Ming-Cheng Chen, Xiawei Chen, Tung-Hsun Chung, Hui Deng, Yajie Du, Daojin Fan, Ming Gong, Cheng Guo, Chu Guo, Shaojun Guo, Lianchen Han, Linyin Hong, He-Liang Huang, Yong-Heng Huo, Liping Li, Na Li, Shaowei Li, Yuan Li, Futian Liang, Chun Lin, Jin Lin, Haoran Qian, Dan Qiao, Hao Rong, Hong Su, Lihua Sun, Liangyuan Wang, Shiyu Wang, Dachao Wu, Yu Xu, Kai Yan, Weifeng Yang, Yang Yang, Yangsen Ye, Jianghan Yin, Chong Ying, Jiale Yu, Chen Zha, Cha Zhang, Haibin Zhang, Kaili Zhang, Yiming Zhang, Han Zhao, Youwei Zhao, Liang Zhou, Qingling Zhu, Chao-Yang Lu, Cheng-Zhi Peng, Xiaobo Zhu, and Jian-Wei Pan. Strong quantum computational advantage using a superconducting quantum processor. *Phys. Rev. Lett.*, 127:180501, Oct 2021.
- [50] Qingling Zhu, Sirui Cao, Fusheng Chen, Ming-Cheng Chen, Xiawei Chen, Tung-Hsun Chung, Hui Deng, Yajie Du, Daojin Fan, Ming Gong, Cheng Guo, Chu Guo, Shaojun Guo, Lianchen Han, Linyin Hong, He-Liang Huang, Yong-Heng Huo, Liping Li, Na Li, Shaowei Li, Yuan Li, Futian Liang, Chun Lin, Jin Lin, Haoran Qian, Dan Qiao, Hao Rong, Hong Su, Lihua Sun, Liangyuan Wang, Shiyu Wang, Dachao Wu, Yulin Wu, Yu Xu, Kai Yan, Weifeng Yang, Yang Yang, Yangsen Ye, Jianghan Yin, Chong Ying, Jiale Yu, Chen Zha, Cha Zhang, Haibin Zhang, Kaili Zhang, Yiming Zhang, Han Zhao, Youwei Zhao, Liang Zhou, Chao-Yang Lu, Cheng-Zhi Peng, Xiaobo Zhu, and Jian-Wei Pan. Quantum computational advantage via 60-qubit 24-cycle random circuit sampling. *Sci. Bull.*, 67(3):240–245, 2022.
- [51] Han-Sen Zhong, Hui Wang, Yu-Hao Deng, Ming-Cheng Chen, Li-Chao Peng, Yi-Han Luo, Jian Qin, Dian Wu, Xing Ding, Yi Hu, Peng Hu, Xiao-Yan Yang, Wei-Jun

- Zhang, Hao Li, Yuxuan Li, Xiao Jiang, Lin Gan, Guangwen Yang, Lixing You, Zhen Wang, Li Li, Nai-Le Liu, Chao-Yang Lu, and Jian-Wei Pan. Quantum computational advantage using photons. *Science*, 370(6523):1460–1463, 2020.
- [52] Han-Sen Zhong, Yu-Hao Deng, Jian Qin, Hui Wang, Ming-Cheng Chen, Li-Chao Peng, Yi-Han Luo, Dian Wu, Si-Qiu Gong, Hao Su, Yi Hu, Peng Hu, Xiao-Yan Yang, Wei-Jun Zhang, Hao Li, Yuxuan Li, Xiao Jiang, Lin Gan, Guangwen Yang, Lixing You, Zhen Wang, Li Li, Nai-Le Liu, Jelmer J. Renema, Chao-Yang Lu, and Jian-Wei Pan. Phase-programmable gaussian boson sampling using stimulated squeezed light. *Phys. Rev. Lett.*, 127:180502, Oct 2021.
- [53] Lars S. Madsen, Fabian Laudenbach, Mohsen Falamarzi. Askarani, Fabien Rortais, Trevor Vincent, Jacob F. F. Bulmer, Filippo M. Miatto, Leonhard Neuhaus, Lukas G. Helt, Matthew J. Collins, Adriana E. Lita, Thomas Gerrits, Sae Woo Nam, Varun D. Vaidya, Matteo Menotti, Ish Dhand, Zachary Vernon, Nicolás Quesada, and Jonathan Lavoie. Quantum computational advantage with a programmable photonic processor. *Nature*, 606(7912):75–81, Jun 2022.
- [54] M. W. Johnson, M. H. S. Amin, S. Gildert, T. Lanting, F. Hamze, N. Dickson, R. Harris, A. J. Berkley, J. Johansson, P. Bunyk, E. M. Chapple, C. Enderud, J. P. Hilton, K. Karimi, E. Ladizinsky, N. Ladizinsky, T. Oh, I. Perminov, C. Rich, M. C. Thom, E. Tolkacheva, C. J. S. Truncik, S. Uchaikin, J. Wang, B. Wilson, and G. Rose. Quantum annealing with manufactured spins. *Nature*, 473(7346):194–198, May 2011.
- [55] Iulia Buluta and Franco Nori. Quantum simulators. *Science*, 326(5949):108–111, 2009.
- [56] I. M. Georgescu, S. Ashhab, and Franco Nori. Quantum simulation. *Rev. Mod. Phys.*, 86:153–185, Mar 2014.
- [57] Javier Argüello-Luengo, Alejandro González-Tudela, Tao Shi, Peter Zoller, and J. Ignacio Cirac. Analogue quantum chemistry simulation. *Nature*, 574(7777):215–218, Oct 2019.
- [58] W Hofstetter and T Qin. Quantum simulation of strongly correlated condensed matter systems. *J. Phys. B*, 51(8):082001, mar 2018.
- [59] Bin Cheng, Xiu-Hao Deng, Xiu Gu, Yu He, Guangchong Hu, Peihao Huang, Jun Li, Ben-Chuan Lin, Dawei Lu, Yao Lu, Chudan Qiu, Hui Wang, Tao Xin, Shi Yu, Man-Hong Yung, Junkai Zeng, Song Zhang, Youpeng Zhong, Xinhua Peng, Franco Nori, and Dapeng Yu. Noisy intermediate-scale quantum computers. *Fron. Phys.*, 18(2):21308, Mar 2023.
- [60] J. I. Cirac and P. Zoller. Quantum computations with cold trapped ions. *Phys. Rev. Lett.*, 74:4091–4094, May 1995.

- [61] Jan Benhelm, Gerhard Kirchmair, Christian F. Roos, and Rainer Blatt. Towards fault-tolerant quantum computing with trapped ions. *Nat. Phys.*, 4(6):463–466, Jun 2008.
- [62] B. P. Lanyon, C. Hempel, D. Nigg, M. Müller, R. Gerritsma, F. Zähringer, P. Schindler, J. T. Barreiro, M. Rambach, G. Kirchmair, M. Hennrich, P. Zoller, R. Blatt, and C. F. Roos. Universal digital quantum simulation with trapped ions. *Science*, 334(6052):57–61, 2011.
- [63] H. Häffner, C.F. Roos, and R. Blatt. Quantum computing with trapped ions. *Phys. Rep.*, 469(4):155–203, 2008.
- [64] Manuel Endres, Hannes Bernien, Alexander Keesling, Harry Levine, Eric R. Anschuetz, Alexandre Krajenbrink, Crystal Senko, Vladan Vuletic, Markus Greiner, and Mikhail D. Lukin. Atom-by-atom assembly of defect-free one-dimensional cold atom arrays. *Science*, 354(6315):1024–1027, 2016.
- [65] T. M. Graham, M. Kwon, B. Grinkemeyer, Z. Marra, X. Jiang, M. T. Lichtman, Y. Sun, M. Ebert, and M. Saffman. Rydberg-mediated entanglement in a two-dimensional neutral atom qubit array. *Phys. Rev. Lett.*, 123:230501, Dec 2019.
- [66] Pascal Scholl, Michael Schuler, Hannah J. Williams, Alexander A. Eberharter, Daniel Barredo, Kai-Niklas Schymik, Vincent Lienhard, Louis-Paul Henry, Thomas C. Lang, Thierry Lahaye, Andreas M. Läuchli, and Antoine Browaeys. Quantum simulation of 2d antiferromagnets with hundreds of rydberg atoms. *Nature*, 595(7866):233–238, Jul 2021.
- [67] Matthew A. Broome, Alessandro Fedrizzi, Saleh Rahimi-Keshari, Justin Dove, Scott Aaronson, Timothy C. Ralph, and Andrew G. White. Photonic boson sampling in a tunable circuit. *Science*, 339(6121):794–798, 2013.
- [68] D. G. Cory, M. D. Price, W. Maas, E. Knill, R. Laflamme, W. H. Zurek, T. F. Havel, and S. S. Somaroo. Experimental quantum error correction. *Phys. Rev. Lett.*, 81:2152–2155, Sep 1998.
- [69] Lieven M. K. Vandersypen, Matthias Steffen, Gregory Breyta, Costantino S. Yannoni, Mark H. Sherwood, and Isaac L. Chuang. Experimental realization of shor’s quantum factoring algorithm using nuclear magnetic resonance. *Nature*, 414(6866):883–887, Dec 2001.
- [70] P. Cappellaro, L. Jiang, J. S. Hodges, and M. D. Lukin. Coherence and control of quantum registers based on electronic spin in a nuclear spin bath. *Phys. Rev. Lett.*, 102:210502, May 2009.

- [71] J. Randall, C. E. Bradley, F. V. van der Gronden, A. Galicia, M. H. Abobeih, M. Markham, D. J. Twitchen, F. Machado, N. Y. Yao, and T. H. Taminiau. Many-body localized discrete time crystal with a programmable spin-based quantum simulator. *Science*, 374(6574):1474–1478, 2021.
- [72] Lieven M. K. Vandersypen and Mark A. Eriksson. Quantum computing with semiconductor spins. *Phys. Today*, 72(8):38–45, 08 2019.
- [73] M. H. Devoret and R. J. Schoelkopf. Superconducting circuits for quantum information: An outlook. *Science*, 339(6124):1169–1174, 2013.
- [74] Alexandre Blais, Arne L. Grimsmo, S. M. Girvin, and Andreas Wallraff. Circuit quantum electrodynamics. *Rev. Mod. Phys.*, 93:025005, May 2021.
- [75] G Wendin. Quantum information processing with superconducting circuits: a review. *Rep. Prog. Phys.*, 80(10):106001, sep 2017.
- [76] Gadi Aleksandrowicz, Thomas Alexander, Panagiotis Barkoutsos, Luciano Bello, Yael Ben-Haim, David Bucher, Francisco Jose Cabrera-Hernández, Jorge Carballo-Franquis, Adrian Chen, Chun-Fu Chen, Jerry M. Chow, Antonio D. Córcoles-Gonzales, Abigail J. Cross, Andrew Cross, Juan Cruz-Benito, Chris Culver, Salvador De La Puente González, Enrique De La Torre, Delton Ding, Eugene Dumitrescu, Ivan Duran, Pieter Eendebak, Mark Everitt, Ismael Faro Sertage, Albert Frisch, Andreas Fuhrer, Jay Gambetta, Borja Godoy Gago, Juan Gomez-Mosquera, Donny Greenberg, Ikko Hamamura, Vojtech Havlicek, Joe Hellmers, Łukasz Herok, Hiroshi Horii, Shaohan Hu, Takashi Imamichi, Toshinari Itoko, Ali Javadi-Abhari, Naoki Kanazawa, Anton Karazeev, Kevin Krsulich, Peng Liu, Yang Luh, Yunho Maeng, Manoel Marques, Francisco Jose Martín-Fernández, Douglas T. McClure, David McKay, Srujan Meesala, Antonio Mezzacapo, Nikolaj Moll, Diego Moreda Rodríguez, Giacomo Nannicini, Paul Nation, Pauline Ollitrault, Lee James O’Riordan, Hanhee Paik, Jesús Pérez, Anna Phan, Marco Pistoia, Viktor Prutyaynov, Max Reuter, Julia Rice, Abdón Rodríguez Davila, Raymond Harry Putra Rudy, Mingi Ryu, Ninad Sathaye, Chris Schnabel, Eddie Schoute, Kanav Setia, Yunong Shi, Adenilton Silva, Yukio Siraichi, Seyon Sivarajah, John A. Smolin, Mathias Soeken, Hitomi Takahashi, Ivano Tavernelli, Charles Taylor, Pete Taylour, Kenso Trabing, Matthew Treinish, Wes Turner, Desiree Vogt-Lee, Christophe Vuillot, Jonathan A. Wildstrom, Jessica Wilson, Erick Winston, Christopher Wood, Stephen Wood, Stefan Wörner, Ismail Yunus Akhalwaya, and Christa Zoufal. Qiskit: An Open-source Framework for Quantum Computing, February 2019.
- [77] Kristan Temme, Sergey Bravyi, and Jay M. Gambetta. Error mitigation for short-depth quantum circuits. *Phys. Rev. Lett.*, 119:180509, Nov 2017.

- [78] Pengfei Wang, Chun-Yang Luan, Mu Qiao, Mark Um, Junhua Zhang, Ye Wang, Xiao Yuan, Mile Gu, Jingning Zhang, and Kihwan Kim. Single ion qubit with estimated coherence time exceeding one hour. *Nat. Commun.*, 12(1):233, Jan 2021.
- [79] Rachel Noek, Geert Vrijsen, Daniel Gaultney, Emily Mount, Taehyun Kim, Peter Maunz, and Jungsang Kim. High speed, high fidelity detection of an atomic hyperfine qubit. *Opt. Lett.*, 38(22):4735–4738, Nov 2013.
- [80] K. Wright, K. M. Beck, S. Debnath, J. M. Amini, Y. Nam, N. Grzesiak, J. S. Chen, N. C. Pisenti, M. Chmielewski, C. Collins, K. M. Hudek, J. Mizrahi, J. D. Wong-Campos, S. Allen, J. Apisdorf, P. Solomon, M. Williams, A. M. Ducore, A. Blinov, S. M. Kreikemeier, V. Chaplin, M. Keesan, C. Monroe, and J. Kim. Benchmarking an 11-qubit quantum computer. *Nat. Comm.*, 10(1):5464, 2019.
- [81] I. Pogorelov, T. Feldker, Ch. D. Marciniak, L. Postler, G. Jacob, O. Kriegelsteiner, V. Podlesnic, M. Meth, V. Negnevitsky, M. Stadler, B. Höfer, C. Wächter, K. Lakhmanskiy, R. Blatt, P. Schindler, and T. Monz. Compact ion-trap quantum computing demonstrator. *PRX Quantum*, 2:020343, Jun 2021.
- [82] Thomas Monz, Daniel Nigg, Esteban A. Martinez, Matthias F. Brandl, Philipp Schindler, Richard Rines, Shannon X. Wang, Isaac L. Chuang, and Rainer Blatt. Realization of a scalable shor algorithm. *Science*, 351(6277):1068–1070, 2016.
- [83] C. Figgatt, D. Maslov, K. A. Landsman, N. M. Linke, S. Debnath, and C. Monroe. Complete 3-qubit grover search on a programmable quantum computer. *Nat. Commun.*, 8(1):1918, Dec 2017.
- [84] D. Bluvstein, A. Omran, H. Levine, A. Keesling, G. Semeghini, S. Ebadi, T. T. Wang, A. A. Michailidis, N. Maskara, W. W. Ho, S. Choi, M. Serbyn, M. Greiner, V. Vuletić, and M. D. Lukin. Controlling quantum many-body dynamics in driven rydberg atom arrays. *Science*, 371(6536):1355–1359, 2021.
- [85] Sepehr Ebadi, Tout T. Wang, Harry Levine, Alexander Keesling, Giulia Semeghini, Ahmed Omran, Dolev Bluvstein, Rhine Samajdar, Hannes Pichler, Wen Wei Ho, Soonwon Choi, Subir Sachdev, Markus Greiner, Vladan Vuletić, and Mikhail D. Lukin. Quantum phases of matter on a 256-atom programmable quantum simulator. *Nature*, 595(7866):227–232, 2021.
- [86] G. Semeghini, H. Levine, A. Keesling, S. Ebadi, T. T. Wang, D. Bluvstein, R. Verresen, H. Pichler, M. Kalinowski, R. Samajdar, A. Omran, S. Sachdev, A. Vishwanath, M. Greiner, V. Vuletić, and M. D. Lukin. Probing topological spin liquids on a programmable quantum simulator. *Science*, 374(6572):1242–1247, December 2021.

- [87] Renate Landig, Lorenz Hruby, Nishant Dogra, Manuele Landini, Rafael Mottl, Tobias Donner, and Tilman Esslinger. Quantum phases from competing short-and long-range interactions in an optical lattice. *Nature*, 532(7600):476–479, 2016.
- [88] H.J. Lipkin, N. Meshkov, and A.J. Glick. Validity of many-body approximation methods for a solvable model: (i). exact solutions and perturbation theory. *Nuclear Physics*, 62(2):188–198, 1965.
- [89] Stefan Schütz and Giovanna Morigi. Prethermalization of atoms due to photon-mediated long-range interactions. *Phys. Rev. Lett.*, 113:203002, Nov 2014.
- [90] Mickael Antoni and Stefano Ruffo. Clustering and relaxation in hamiltonian long-range dynamics. *Phys. Rev. E*, 52:2361–2374, Sep 1995.
- [91] M. Morgado and S. Whitlock. Quantum simulation and computing with rydberg-interacting qubits. *AVS Quantum Science*, 3(2):023501, Jun 2021.
- [92] Nicolò Defenu, Alessio Lerose, and Silvia Pappalardi. Out-of-equilibrium dynamics of quantum many-body systems with long-range interactions. *Physics Reports*, 1074:1–92, 2024. Out-of-equilibrium dynamics of quantum many-body systems with long-range interactions.
- [93] Stefano Gherardini, Lorenzo Buffoni, and Nicolò Defenu. Universal defects statistics with strong long-range interactions, 2023.
- [94] Shamik Gupta, Alessandro Campa, and Stefano Ruffo. Overdamped dynamics of long-range systems on a one-dimensional lattice: Dominance of the mean-field mode and phase transition. *Phys. Rev. E*, 86:061130, Dec 2012.
- [95] Michael Kastner. Diverging equilibration times in long-range quantum spin models. *Phys. Rev. Lett.*, 106:130601, Mar 2011.
- [96] A Yu Kitaev. Unpaired majorana fermions in quantum wires. *Physics-Uspekhi*, 44(10S):131–136, oct 2001.
- [97] Davide Vodola, Luca Lepori, Elisa Ercolessi, Alexey V. Gorshkov, and Guido Pupillo. Kitaev chains with long-range pairing. *Phys. Rev. Lett.*, 113:156402, Oct 2014.
- [98] Somnath Maity, Utso Bhattacharya, and Amit Dutta. One-dimensional quantum many body systems with long-range interactions. *Journal of Physics A: Mathematical and Theoretical*, 53(1):013001, dec 2019.
- [99] Philipp Uhrich, Nicolò Defenu, Rouhollah Jafari, and Jad C. Halimeh. Out-of-equilibrium phase diagram of long-range superconductors. *Phys. Rev. B*, 101:245148, Jun 2020.

- [100] Antonio Alecce and Luca Dell'Anna. Extended kitaev chain with longer-range hopping and pairing. *Phys. Rev. B*, 95:195160, May 2017.
- [101] Simon B. Jäger, Luca Dell'Anna, and Giovanna Morigi. Edge states of the long-range kitaev chain: An analytical study. *Phys. Rev. B*, 102:035152, Jul 2020.
- [102] Wade DeGottardi, Manisha Thakurathi, Smitha Vishveshwara, and Diptiman Sen. Majorana fermions in superconducting wires: Effects of long-range hopping, broken time-reversal symmetry, and potential landscapes. *Phys. Rev. B*, 88:165111, Oct 2013.
- [103] Nicolò Defenu. Metastability and discrete spectrum of long-range systems. *Proceedings of the National Academy of Sciences*, 118(30):e2101785118, 2021.
- [104] L Lepori and L Dell'Anna. Long-range topological insulators and weakened bulk-boundary correspondence. *New Journal of Physics*, 19(10):103030, 2017.
- [105] Jacek Dziarmaga. Dynamics of a quantum phase transition and relaxation to a steady state. *Advances in Physics*, 59(6):1063–1189, 2010.
- [106] Lev Davidovich Landau. Zur theorie der energieubertragung ii. *Z. Sowjetunion*, 2:46–51, 1932.
- [107] Clarence Zener and Ralph Howard Fowler. Non-adiabatic crossing of energy levels. *Proceedings of the Royal Society of London. Series A, Containing Papers of a Mathematical and Physical Character*, 137(833):696–702, 1932.
- [108] E. C. G. Stueckelberg. Theorie der unelastischen stösse zwischen atomen. *Helvetica Physica Acta*, 5(VI):369, 1932.
- [109] Ettore Majorana. Atomi orientati in campo magnetico variabile. *Il Nuovo Cimento (1924-1942)*, 9(2):43–50, Feb 1932.
- [110] N. V. Vitanov and B. M. Garraway. Landau-zener model: Effects of finite coupling duration. *Phys. Rev. A*, 53:4288–4304, Jun 1996.
- [111] C. De Grandi and A. Polkovnikov. *Adiabatic Perturbation Theory: From Landau-Zener Problem to Quenching Through a Quantum Critical Point*, pages 75–114. Springer Berlin Heidelberg, Berlin, Heidelberg, 2010.
- [112] J. Sak. Recursion relations and fixed points for ferromagnets with long-range interactions. *Phys. Rev. B*, 8:281–285, Jul 1973.
- [113] R. A. Baños, L. A. Fernandez, V. Martin-Mayor, and A. P. Young. Correspondence between long-range and short-range spin glasses. *Phys. Rev. B*, 86:134416, Oct 2012.

- [114] Nicolás Defenu, Andrea Trombettoni, and Alessandro Codello. Fixed-point structure and effective fractional dimensionality for $o(n)$ models with long-range interactions. *Phys. Rev. E*, 92:052113, Nov 2015.
- [115] Ivan Balog, Gilles Tarjus, and Matthieu Tissier. Critical behaviour of the random-field ising model with long-range interactions in one dimension. *Journal of Statistical Mechanics: Theory and Experiment*, 2014(10):P10017, October 2014.
- [116] Erik Luijten and Henk W. J. Blöte. Boundary between long-range and short-range critical behavior in systems with algebraic interactions. *Phys. Rev. Lett.*, 89:025703, Jun 2002.
- [117] Toshiki Horita, Hidemaro Suwa, and Synge Todo. Upper and lower critical decay exponents of ising ferromagnets with long-range interaction. *Phys. Rev. E*, 95:012143, Jan 2017.
- [118] Connor Behan, Leonardo Rastelli, Slava Rychkov, and Bernardo Zan. A scaling theory for the long-range to short-range crossover and an infrared duality. *Journal of Physics A: Mathematical and Theoretical*, 50(35):354002, August 2017.
- [119] J. Zinn-Justin. *Quantum Field Theory and Critical Phenomena*. International series of monographs on physics. Oxford University Press, 2021.
- [120] Kenneth G. Wilson. The renormalization group and critical phenomena. *Rev. Mod. Phys.*, 55:583–600, Jul 1983.
- [121] Joseph Polchinski. Renormalization and effective lagrangians. *Nuclear Physics B*, 231(2):269–295, 1984.
- [122] Christof Wetterich. Exact evolution equation for the effective potential. *Physics Letters B*, 301(1):90–94, 1993.
- [123] Daniel F. Litim. Critical exponents from optimised renormalisation group flows. *Nuclear Physics B*, 631(1):128–158, 2002.
- [124] Nicolò Defenu, Andrea Trombettoni, and Stefano Ruffo. Anisotropic long-range spin systems. *Phys. Rev. B*, 94:224411, Dec 2016.
- [125] Alessandro Codello, Nicolás Defenu, and Giulio D’Odorico. Critical exponents of $o(n)$ models in fractional dimensions. *Phys. Rev. D*, 91:105003, May 2015.
- [126] Tim R Morris. On truncations of the exact renormalization group. *Physics Letters B*, 334(3-4):355–362, 1994.

- [127] Connor Behan, Edoardo Lauria, Maria Nocchi, and Philine van Vliet. Analytic and numerical bootstrap for the long-range ising model. *Journal of High Energy Physics*, 2024(3):136, 2024.
- [128] Erik Luijten and Henk W.J. Blöte. Monte carlo method for spin models with long-range interactions. *International Journal of Modern Physics C*, 06(03):359–370, 1995.
- [129] T. Blanchard, M. Picco, and M. A. Rajabpour. Influence of long-range interactions on the critical behavior of the ising model. *Europhysics Letters*, 101(5):56003, mar 2013.
- [130] Peter Grassberger. Two-dimensional sir epidemics with long range infection. *Journal of Statistical Physics*, 153(2):289–311, Oct 2013.
- [131] Sheer El-Showk, Miguel Paulos, David Poland, Slava Rychkov, David Simmons-Duffin, and Alessandro Vichi. Conformal field theories in fractional dimensions. *Phys. Rev. Lett.*, 112:141601, Apr 2014.
- [132] H. Zu, W. Dai, and A.T.A.M. de Waele. Development of dilution refrigerators—a review. *Cryogenics*, 121:103390, 2022.
- [133] John Preskill. Quantum Computing in the NISQ era and beyond. *Quantum*, 2:79, 2018.
- [134] D. Aharonov and M. Ben-Or. Fault-tolerant quantum computation with constant error. In *Proceedings of the Twenty-Ninth Annual ACM Symposium on Theory of Computing*, STOC '97, page 176–188, New York, NY, USA, 1997. Association for Computing Machinery.
- [135] A Yu Kitaev. Quantum computations: algorithms and error correction. *Russian Mathematical Surveys*, 52(6):1191–1249, dec 1997.
- [136] Emanuel Knill, Raymond Laflamme, and Wojciech H. Zurek. Resilient quantum computation. *Science*, 279(5349):342–345, 1998.
- [137] Alexia Auffèves. Quantum technologies need a quantum energy initiative. *PRX Quantum*, 3:020101, Jun 2022.
- [138] Nathan M. Myers, Obinna Abah, and Sebastian Deffner. Quantum thermodynamic devices: From theoretical proposals to experimental reality. *AVS Quantum Science*, 4(2):027101, 2022.
- [139] R Alicki. The quantum open system as a model of the heat engine. *Journal of Physics A: Mathematical and General*, 12(5):L103–L107, may 1979.

- [140] Armen E. Allahverdyan, Ramandeep S. Johal, and Guenter Mahler. Work extremum principle: Structure and function of quantum heat engines. *Phys. Rev. E*, 77:041118, Apr 2008.
- [141] Michele Campisi, Jukka Pekola, and Rosario Fazio. Nonequilibrium fluctuations in quantum heat engines: theory, example, and possible solid state experiments. *New J. Phys.*, 17(3):035012, 2015.
- [142] Michele Campisi and Rosario Fazio. The power of a critical heat engine. *Nat. Commun.*, 7(1):11895, Jun 2016.
- [143] B. Karimi and J. P. Pekola. Otto refrigerator based on a superconducting qubit: Classical and quantum performance. *Phys. Rev. B*, 94:184503, Nov 2016.
- [144] Alexander Friedenberger and Eric Lutz. When is a quantum heat engine quantum? *EPL (Europhysics Letters)*, 120(1):10002, oct 2017.
- [145] Ronnie Kosloff and Yair Rezek. The quantum harmonic otto cycle. *Entropy*, 19(4), 2017.
- [146] Sebastian Deffner and Steve Campbell. Thermodynamics of quantum systems. In *Quantum Thermodynamics*, 2053-2571, pages 2–1 to 2–37. Morgan & Claypool Publishers, 2019.
- [147] Jean-Philippe Brantut, Charles Grenier, Jakob Meineke, David Stadler, Sebastian Krinner, Corinna Kollath, Tilman Esslinger, and Antoine Georges. A thermoelectric heat engine with ultracold atoms. *Science*, 342(6159):713–715, 2013.
- [148] Johannes Roßnagel, Samuel T. Dawkins, Karl N. Tolazzi, Obinna Abah, Eric Lutz, Ferdinand Schmidt-Kaler, and Kilian Singer. A single-atom heat engine. *Science*, 352(6283):325–329, 2016.
- [149] Noah Van Horne, Dahyun Yum, Tarun Dutta, Peter Hänggi, Jiangbin Gong, Dario Poletti, and Manas Mukherjee. Single-atom energy-conversion device with a quantum load. *npj Quantum Information*, 6(1):37, May 2020.
- [150] Jan Klaers, Stefan Faelt, Atac Imamoglu, and Emre Togan. Squeezed thermal reservoirs as a resource for a nanomechanical engine beyond the carnot limit. *Phys. Rev. X*, 7:031044, Sep 2017.
- [151] D. von Lindenfels, O. Gräß, C. T. Schmiegelow, V. Kaushal, J. Schulz, Mark T. Mitchison, John Goold, F. Schmidt-Kaler, and U. G. Poschinger. Spin heat engine coupled to a harmonic-oscillator flywheel. *Phys. Rev. Lett.*, 123:080602, Aug 2019.

- [152] John P. S. Peterson, Tiago B. Batalhão, Marcela Herrera, Alexandre M. Souza, Roberto S. Sarthour, Ivan S. Oliveira, and Roberto M. Serra. Experimental characterization of a spin quantum heat engine. *Phys. Rev. Lett.*, 123:240601, Dec 2019.
- [153] James Klatzow, Jonas N. Becker, Patrick M. Ledingham, Christian Weinzetl, Krzysztof T. Kaczmarek, Dylan J. Saunders, Joshua Nunn, Ian A. Walmsley, Raam Uzdin, and Eilon Poem. Experimental demonstration of quantum effects in the operation of microscopic heat engines. *Phys. Rev. Lett.*, 122:110601, Mar 2019.
- [154] Quentin Bouton, Jens Nettersheim, Sabrina Burgardt, Daniel Adam, Eric Lutz, and Artur Widera. A quantum heat engine driven by atomic collisions. *Nature Communications*, 12(1):2063, Apr 2021.
- [155] Dominik Hahn, Maxime Dupont, Markus Schmitt, David J. Luitz, and Marin Bukov. Quantum many-body jarzynski equality and dissipative noise on a digital quantum computer. *Phys. Rev. X*, 13:041023, Nov 2023.
- [156] Enrico Fermi. *Thermodynamics*. Dover Publications, 1956.
- [157] Xi Chen, A. Ruschhaupt, S. Schmidt, A. del Campo, D. Guéry-Odelin, and J. G. Muga. Fast optimal frictionless atom cooling in harmonic traps: Shortcut to adiabaticity. *Phys. Rev. Lett.*, 104:063002, Feb 2010.
- [158] A. del Campo, J. Goold, and M. Paternostro. More bang for your buck: Superadiabatic quantum engines. *Scientific Reports*, 4(1):6208, Aug 2014.
- [159] Obinna Abah and Eric Lutz. Energy efficient quantum machines. *EPL (Europhysics Letters)*, 118(4):40005, may 2017.
- [160] D. Guéry-Odelin, A. Ruschhaupt, A. Kiely, E. Torrontegui, S. Martínez-Garaot, and J. G. Muga. Shortcuts to adiabaticity: Concepts, methods, and applications. *Rev. Mod. Phys.*, 91:045001, Oct 2019.
- [161] Steve Campbell and Sebastian Deffner. Trade-off between speed and cost in shortcuts to adiabaticity. *Phys. Rev. Lett.*, 118:100601, Mar 2017.
- [162] Obinna Abah and Eric Lutz. Performance of shortcut-to-adiabaticity quantum engines. *Phys. Rev. E*, 98:032121, Sep 2018.
- [163] Peter Talkner, Eric Lutz, and Peter Hänggi. Fluctuation theorems: Work is not an observable. *Phys. Rev. E*, 75:050102, May 2007.
- [164] John Goold, Francesco Plastina, Andrea Gambassi, and Alessandro Silva. *The Role of Quantum Work Statistics in Many-Body Physics*, pages 317–336. Springer International Publishing, Cham, 2018.

- [165] Andrea Gambassi and Alessandro Silva. Large deviations and universality in quantum quenches. *Phys. Rev. Lett.*, 109:250602, Dec 2012.
- [166] Andrea Gambassi and Alessandro Silva. Statistics of the work in quantum quenches, universality and the critical casimir effect, 2011.
- [167] Michael Krech. *The Casimir Effect in Critical Systems*. WORLD SCIENTIFIC, 1994.
- [168] M Krech. Fluctuation-induced forces in critical fluids. *Journal of Physics: Condensed Matter*, 11(37):R391, sep 1999.
- [169] Andrea Gambassi. The casimir effect: From quantum to critical fluctuations. *Journal of Physics: Conference Series*, 161(1):012037, apr 2009.
- [170] K. Binder, F. F. Haas, and F. Schmid. Critical phenomena at the surface of systems undergoing a bulk first order transition: Are they understood? In David P. Landau, Steven P. Lewis, and Heinz-Bernd Schüttler, editors, *Computer Simulation Studies in Condensed-Matter Physics XIV*, pages 85–96, Berlin, Heidelberg, 2002. Springer Berlin Heidelberg.
- [171] Hugo Touchette. The large deviation approach to statistical mechanics. *Physics Reports*, 478(1):1–69, 2009.
- [172] Alessandro Silva. Statistics of the work done on a quantum critical system by quenching a control parameter. *Phys. Rev. Lett.*, 101:120603, Sep 2008.
- [173] Krissia Zawadzki, Anthony Kiely, Gabriel T. Landi, and Steve Campbell. Non-gaussian work statistics at finite-time driving. *Phys. Rev. A*, 107:012209, Jan 2023.
- [174] Anatoli Polkovnikov. Universal adiabatic dynamics in the vicinity of a quantum critical point. *Phys. Rev. B*, 72:161201, Oct 2005.
- [175] Adolfo del Campo. Universal statistics of topological defects formed in a quantum phase transition. *Phys. Rev. Lett.*, 121:200601, Nov 2018.
- [176] Zhaoyu Fei, Nahuel Freitas, Vasco Cavina, H. T. Quan, and Massimiliano Esposito. Work statistics across a quantum phase transition. *Phys. Rev. Lett.*, 124:170603, May 2020.
- [177] Federico Balducci, Mathieu Beau, Jing Yang, Andrea Gambassi, and Adolfo del Campo. Large deviations beyond the kibble-zurek mechanism. *Phys. Rev. Lett.*, 131:230401, Dec 2023.

- [178] Anatoli Polkovnikov, Krishnendu Sengupta, Alessandro Silva, and Mukund Vengalattore. Colloquium: Nonequilibrium dynamics of closed interacting quantum systems. *Rev. Mod. Phys.*, 83:863–883, Aug 2011.
- [179] Emma C. King, Michael Kastner, and Johannes N. Kriel. Long-range kitaev chain in a thermal bath: Analytic techniques for time-dependent systems and environments, 2022.
- [180] H. Quan, Yu Xi Liu, C. Sun, and Franco Nori. Quantum thermodynamic cycles and quantum heat engines. *Phys. Rev. E*, 76:031105, 2007.
- [181] Nicolas Gisin, Grégoire Ribordy, Wolfgang Tittel, and Hugo Zbinden. Quantum cryptography. *Rev. Mod. Phys.*, 74:145–195, Mar 2002.
- [182] Vittorio Giovannetti, Seth Lloyd, and Lorenzo Maccone. Advances in quantum metrology. *Nature Photonics*, 5(4):222–229, Apr 2011.
- [183] J. Zhang, G. Pagano, P. W. Hess, A. Kyprianidis, P. Becker, H. Kaplan, A. V. Gorshkov, Z.-X. Gong, and C. Monroe. Observation of a many-body dynamical phase transition with a 53-qubit quantum simulator. *Nature*, 551(7682):601–604, November 2017.
- [184] P. Jurcevic, H. Shen, P. Hauke, C. Maier, T. Brydges, C. Hempel, B. P. Lanyon, M. Heyl, R. Blatt, and C. F. Roos. Direct observation of dynamical quantum phase transitions in an interacting many-body system. *Phys. Rev. Lett.*, 119:080501, Aug 2017.
- [185] Milena Grifoni and Peter Hänggi. Driven quantum tunneling. *Physics Reports*, 304(5):229–354, 1998.
- [186] Marcos Rigol, Vanja Dunjko, and Maxim Olshanii. Thermalization and its mechanism for generic isolated quantum systems. *Nature*, 452(7189):854–858, Apr 2008.
- [187] Adam M. Kaufman, M. Eric Tai, Alexander Lukin, Matthew Rispoli, Robert Schittko, Philipp M. Preiss, and Markus Greiner. Quantum thermalization through entanglement in an isolated many-body system. *Science*, 353(6301):794–800, 2016.
- [188] Takashi Mori, Tatsuhiko N Ikeda, Eriko Kaminishi, and Masahito Ueda. Thermalization and prethermalization in isolated quantum systems: a theoretical overview. *Journal of Physics B: Atomic, Molecular and Optical Physics*, 51(11):112001, may 2018.
- [189] Luca D'Alessio, Yariv Kafri, Anatoli Polkovnikov, and Marcos Rigol. From quantum chaos and eigenstate thermalization to statistical mechanics and thermodynamics. *Advances in Physics*, 65(3):239–362, May 2016.

- [190] M. Heyl, A. Polkovnikov, and S. Kehrein. Dynamical quantum phase transitions in the transverse-field ising model. *Phys. Rev. Lett.*, 110:135704, Mar 2013.
- [191] Markus Heyl. Dynamical quantum phase transitions: a review. *Reports on Progress in Physics*, 81(5):054001, apr 2018.
- [192] Bojan Žunkovič, Markus Heyl, Michael Knap, and Alessandro Silva. Dynamical quantum phase transitions in spin chains with long-range interactions: Merging different concepts of nonequilibrium criticality. *Phys. Rev. Lett.*, 120:130601, Mar 2018.
- [193] Markus Karl, Halil Cakir, Jad C. Halimeh, Markus K. Oberthaler, Michael Kastner, and Thomas Gasenzer. Universal equilibrium scaling functions at short times after a quench. *Phys. Rev. E*, 96:022110, Aug 2017.
- [194] Jad C. Halimeh, Valentin Zauner-Stauber, Ian P. McCulloch, Inés de Vega, Ulrich Schollwöck, and Michael Kastner. Prethermalization and persistent order in the absence of a thermal phase transition. *Physical Review B*, 95(2), January 2017.
- [195] Frank Wilczek. Quantum time crystals. *Phys. Rev. Lett.*, 109:160401, Oct 2012.
- [196] Patrick Bruno. Impossibility of spontaneously rotating time crystals: A no-go theorem. *Phys. Rev. Lett.*, 111:070402, Aug 2013.
- [197] Haruki Watanabe and Masaki Oshikawa. Absence of quantum time crystals. *Phys. Rev. Lett.*, 114:251603, Jun 2015.
- [198] Krzysztof Sacha. Modeling spontaneous breaking of time-translation symmetry. *Phys. Rev. A*, 91:033617, Mar 2015.
- [199] Dominic V. Else, Bela Bauer, and Chetan Nayak. Floquet time crystals. *Phys. Rev. Lett.*, 117:090402, Aug 2016.
- [200] Vedika Khemani, Achilleas Lazarides, Roderich Moessner, and S. L. Sondhi. Phase structure of driven quantum systems. *Phys. Rev. Lett.*, 116:250401, Jun 2016.
- [201] J. Zhang, P. W. Hess, A. Kyprianidis, P. Becker, A. Lee, J. Smith, G. Pagano, I.-D. Potirniche, A. C. Potter, A. Vishwanath, N. Y. Yao, and C. Monroe. Observation of a discrete time crystal. *Nature*, 543(7644):217–220, Mar 2017.
- [202] Soonwon Choi, Joonhee Choi, Renate Landig, Georg Kucsko, Hengyun Zhou, Junichi Isoya, Fedor Jelezko, Shinobu Onoda, Hitoshi Sumiya, Vedika Khemani, Curt von Keyserlingk, Norman Y. Yao, Eugene Demler, and Mikhail D. Lukin. Observation of discrete time-crystalline order in a disordered dipolar many-body system. *Nature*, 543(7644):221–225, Mar 2017.

- [203] Jared Rovny, Robert L. Blum, and Sean E. Barrett. Observation of discrete-time-crystal signatures in an ordered dipolar many-body system. *Phys. Rev. Lett.*, 120:180603, May 2018.
- [204] Pranjal Bordia, Henrik Lüschen, Ulrich Schneider, Michael Knap, and Immanuel Bloch. Periodically driving a many-body localized quantum system. *Nature Physics*, 13(5):460–464, May 2017.
- [205] Angelo Russomanno, Fernando Iemini, Marcello Dalmonte, and Rosario Fazio. Floquet time crystal in the lipkin-meshkov-glick model. *Phys. Rev. B*, 95:214307, Jun 2017.
- [206] D. Mukamel, S. Ruffo, and N. Schreiber. Breaking of ergodicity and long relaxation times in systems with long-range interactions. *Phys. Rev. Lett.*, 95:240604, Dec 2005.
- [207] Shane P. Kelly, Eddy Timmermans, Jamir Marino, and S.-W. Tsai. Stroboscopic aliasing in long-range interacting quantum systems. *SciPost Phys. Core*, 4:021, 2021.
- [208] Federica Maria Surace, Angelo Russomanno, Marcello Dalmonte, Alessandro Silva, Rosario Fazio, and Fernando Iemini. Floquet time crystals in clock models. *Phys. Rev. B*, 99:104303, Mar 2019.
- [209] Manuel H. Muñoz Arias, Karthik Chinni, and Pablo M. Poggi. Floquet time crystals in driven spin systems with all-to-all p -body interactions. *Phys. Rev. Res.*, 4:023018, Apr 2022.
- [210] Mario Collura, Andrea De Luca, Davide Rossini, and Alessio Lerose. Discrete time-crystalline response stabilized by domain-wall confinement. *Phys. Rev. X*, 12:031037, Sep 2022.
- [211] Francisco Machado, Dominic V. Else, Gregory D. Kahanamoku-Meyer, Chetan Nayak, and Norman Y. Yao. Long-range prethermal phases of nonequilibrium matter. *Phys. Rev. X*, 10:011043, Feb 2020.
- [212] Andrea Pizzi, Johannes Knolle, and Andreas Nunnenkamp. Higher-order and fractional discrete time crystals in clean long-range interacting systems. *Nature Communications*, 12(1):2341, Apr 2021.
- [213] Alessio Lerose, Jamir Marino, Andrea Gambassi, and Alessandro Silva. Prethermal quantum many-body kapitza phases of periodically driven spin systems. *Phys. Rev. B*, 100:104306, Sep 2019.
- [214] Bruno Sciola and Giulio Biroli. Quantum quenches, dynamical transitions, and off-equilibrium quantum criticality. *Physical Review B*, 88(20), November 2013.

- [215] AN Kolmogorov. On the conservative of conditionally periodic motions for a small change in hamilton's function (in russ.), dokl. acad. nauk sssr 98,(1954), 524–530; english transl. *Lecture Notes in Physics*, 93:51–56, 1979.
- [216] Vladimir I Arnold. Proof of a theorem of an kolmogorov on the invariance of quasi-periodic motions under small perturbations of the hamiltonian. *Collected Works: Representations of Functions, Celestial Mechanics and KAM Theory, 1957–1965*, pages 267–294, 2009.
- [217] J Möser. On invariant curves of area-preserving mappings of an annulus. *Nachr. Akad. Wiss. Göttingen, II*, pages 1–20, 1962.
- [218] M. Brown and W. D. Neumann. Proof of the Poincaré-Birkhoff fixed point theorem. *Michigan Mathematical Journal*, 24(1):21 – 31, 1977.
- [219] Pedro Ribeiro, Julien Vidal, and Rémy Mosseri. Exact spectrum of the lipkin-meshkov-glick model in the thermodynamic limit and finite-size corrections. *Physical Review E*, 78(2), August 2008.
- [220] Assa Auerbach. *Interacting electrons and quantum magnetism*. Springer Science & Business Media, 2012.
- [221] M. B. Hastings. Exact multifractal spectra for arbitrary laplacian random walks. *Phys. Rev. Lett.*, 88:055506, Jan 2002.
- [222] Bertrand Duplantier. Conformally invariant fractals and potential theory. *Phys. Rev. Lett.*, 84:1363–1367, Feb 2000.
- [223] Wouter Kager and Bernard Nienhuis. A guide to stochastic löwner evolution and its applications. *Journal of Statistical Physics*, 115(5):1149–1229, Jun 2004.
- [224] John Cardy. Sle for theoretical physicists. *Annals of Physics*, 318(1):81–118, 2005. Special Issue.
- [225] R.S. MacKay. A renormalization approach to invariant circles in area-preserving maps. *Physica D: Nonlinear Phenomena*, 7(1):283–300, 1983.
- [226] Massimo Cencini, Fabio Cecconi, and Angelo Vulpiani. *Chaos*. WORLD SCIENTIFIC, 2009.
- [227] H. P. Ojeda Collado, Gonzalo Usaj, C. A. Balseiro, Damián H. Zanette, and José Lorenzana. Emergent parametric resonances and time-crystal phases in driven bardeen-cooper-schrieffer systems. *Phys. Rev. Res.*, 3:L042023, Nov 2021.

- [228] Xiao Mi, Matteo Ippoliti, Chris Quintana, Ami Greene, Zijun Chen, Jonathan Gross, Frank Arute, Kunal Arya, Juan Atalaya, Ryan Babbush, Joseph C. Bardin, Joao Basso, Andreas Bengtsson, Alexander Bilmes, Alexandre Bourassa, Leon Brill, Michael Broughton, Bob B. Buckley, David A. Buell, Brian Burkett, Nicholas Bushnell, Benjamin Chiaro, Roberto Collins, William Courtney, Dripto Debroy, Sean Demura, Alan R. Derk, Andrew Dunsworth, Daniel Eppens, Catherine Erickson, Edward Farhi, Austin G. Fowler, Brooks Foxen, Craig Gidney, Marissa Giustina, Matthew P. Harrigan, Sean D. Harrington, Jeremy Hilton, Alan Ho, Sabrina Hong, Trent Huang, Ashley Huff, William J. Huggins, L. B. Ioffe, Sergei V. Isakov, Justin Iveland, Evan Jeffrey, Zhang Jiang, Cody Jones, Dvir Kafri, Tanuj Khattar, Seon Kim, Alexei Kitaev, Paul V. Klimov, Alexander N. Korotkov, Fedor Kostritsa, David Landhuis, Pavel Laptev, Joonho Lee, Kenny Lee, Aditya Locharla, Erik Lucero, Orion Martin, Jarrod R. McClean, Trevor McCourt, Matt McEwen, Kevin C. Miao, Masoud Mohseni, Shirin Montazeri, Wojciech Mroczkiewicz, Ofer Naaman, Matthew Neeley, Charles Neill, Michael Newman, Murphy Yuezhen Niu, Thomas E. O'Brien, Alex Opremcak, Eric Ostby, Balint Pato, Andre Petukhov, Nicholas C. Rubin, Daniel Sank, Kevin J. Satzinger, Vladimir Shvarts, Yuan Su, Doug Strain, Marco Szalay, Matthew D. Trevithick, Benjamin Villalonga, Theodore White, Z. Jamie Yao, Ping Yeh, Juhwan Yoo, Adam Zalcman, Hartmut Neven, Sergio Boixo, Vadim Smelyanskiy, Anthony Megrant, Julian Kelly, Yu Chen, S. L. Sondhi, Roderich Moessner, Kostyantyn Kechedzhi, Vedika Khemani, and Pedram Roushan. Time-crystalline eigenstate order on a quantum processor. *Nature*, 601(7894):531–536, Jan 2022.
- [229] Philipp Frey and Stephan Rachel. Realization of a discrete time crystal on 57 qubits of a quantum computer. *Science Advances*, 8(9):eabm7652, 2022.
- [230] K. J. Satzinger, Y.-J. Liu, A. Smith, C. Knapp, M. Newman, C. Jones, Z. Chen, C. Quintana, X. Mi, A. Dunsworth, C. Gidney, I. Aleiner, F. Arute, K. Arya, J. Atalaya, R. Babbush, J. C. Bardin, R. Barends, J. Basso, A. Bengtsson, A. Bilmes, M. Broughton, B. B. Buckley, D. A. Buell, B. Burkett, N. Bushnell, B. Chiaro, R. Collins, W. Courtney, S. Demura, A. R. Derk, D. Eppens, C. Erickson, L. Faoro, E. Farhi, A. G. Fowler, B. Foxen, M. Giustina, A. Greene, J. A. Gross, M. P. Harrigan, S. D. Harrington, J. Hilton, S. Hong, T. Huang, W. J. Huggins, L. B. Ioffe, S. V. Isakov, E. Jeffrey, Z. Jiang, D. Kafri, K. Kechedzhi, T. Khattar, S. Kim, P. V. Klimov, A. N. Korotkov, F. Kostritsa, D. Landhuis, P. Laptev, A. Locharla, E. Lucero, O. Martin, J. R. McClean, M. McEwen, K. C. Miao, M. Mohseni, S. Montazeri, W. Mroczkiewicz, J. Mutus, O. Naaman, M. Neeley, C. Neill, M. Y. Niu, T. E. O'Brien, A. Opremcak, B. Pató, A. Petukhov, N. C. Rubin, D. Sank, V. Shvarts, D. Strain, M. Szalay, B. Villalonga, T. C. White, Z. Yao, P. Yeh, J. Yoo, A. Zalcman, H. Neven, S. Boixo, A. Megrant, Y. Chen, J. Kelly, V. Smelyanskiy, A. Kitaev, M. Knap, F. Pollmann, and P. Roushan. Realizing topologically ordered states on a quantum processor. *Science*, 374(6572):1237–1241, 2021.

- [231] Xu Zhang, Wenjie Jiang, Jinfeng Deng, Ke Wang, Jiachen Chen, Pengfei Zhang, Wenhui Ren, Hang Dong, Shibo Xu, Yu Gao, Feitong Jin, Xuhao Zhu, Qiujiang Guo, Hekang Li, Chao Song, Alexey V. Gorshkov, Thomas Iadecola, Fangli Liu, Zhe-Xuan Gong, Zhen Wang, Dong-Ling Deng, and H. Wang. Digital quantum simulation of floquet symmetry-protected topological phases. *Nature*, 607(7919):468–473, Jul 2022.
- [232] X. Mi, M. Sonner, M. Y. Niu, K. W. Lee, B. Foxen, R. Acharya, I. Aleiner, T. I. Andersen, F. Arute, K. Arya, A. Asfaw, J. Atalaya, J. C. Bardin, J. Basso, A. Bengtsson, G. Bortoli, A. Bourassa, L. Brill, M. Broughton, B. B. Buckley, D. A. Buell, B. Burkett, N. Bushnell, Z. Chen, B. Chiaro, R. Collins, P. Conner, W. Courtney, A. L. Crook, D. M. Debroy, S. Demura, A. Dunsworth, D. Eppens, C. Erickson, L. Faoro, E. Farhi, R. Fatemi, L. Flores, E. Forati, A. G. Fowler, W. Giang, C. Gidney, D. Gilboa, M. Giustina, A. G. Dau, J. A. Gross, S. Habegger, M. P. Harrigan, M. Hoffmann, S. Hong, T. Huang, A. Huff, W. J. Huggins, L. B. Ioffe, S. V. Isakov, J. Iveland, E. Jeffrey, Z. Jiang, C. Jones, D. Kafri, K. Kechedzhi, T. Khattar, S. Kim, A. Y. Kitaev, P. V. Klimov, A. R. Klots, A. N. Korotkov, F. Kostritsa, J. M. Kreikebaum, D. Landhuis, P. Laptev, K.-M. Lau, J. Lee, L. Laws, W. Liu, A. Locharlar, O. Martin, J. R. McClean, M. McEwen, B. Meurer Costa, K. C. Miao, M. Mohseni, S. Montazeri, A. Morvan, E. Mount, W. Mroczkiewicz, O. Naaman, M. Neeley, C. Neill, M. Newman, T. E. O’Brien, A. Opremcak, A. Petukhov, R. Potter, C. Quintana, N. C. Rubin, N. Saei, D. Sank, K. Sankaragomathi, K. J. Satzinger, C. Schuster, M. J. Shearn, V. Shvarts, D. Strain, Y. Su, M. Szalay, G. Vidal, B. Villalonga, C. Vollgraft-Heidweiller, T. White, Z. Yao, P. Yeh, J. Yoo, A. Zalcman, Y. Zhang, N. Zhu, H. Neven, D. Bacon, J. Hilton, E. Lucero, R. Babbush, S. Boixo, A. Megrant, Y. Chen, J. Kelly, V. Smelyanskiy, D. A. Abanin, and P. Roushan. Noise-resilient edge modes on a chain of superconducting qubits. *Science*, 378(6621):785–790, 2022.
- [233] Alessandro Santini and Vittorio Vitale. Experimental violations of Leggett-Garg inequalities on a quantum computer. *Phys. Rev. A*, 105:032610, Mar 2022.
- [234] Matteo Ippoliti, Kostyantyn Kechedzhi, Roderich Moessner, S.L. Sondhi, and Vedika Khemani. Many-body physics in the nisq era: Quantum programming a discrete time crystal. *PRX Quantum*, 2:030346, Sep 2021.
- [235] Tim Weaving, Alexis Ralli, William M. Kirby, Peter J. Love, Sauro Succi, and Peter V. Coveney. Benchmarking noisy intermediate scale quantum error mitigation strategies for ground state preparation of the hcl molecule. *Phys. Rev. Res.*, 5:043054, Oct 2023.
- [236] Michael A. Nielsen and Isaac L. Chuang. *Quantum Computation and Quantum Information: 10th Anniversary Edition*. Cambridge University Press, 2010.
- [237] Ying Li and Simon C. Benjamin. Efficient variational quantum simulator incorporating active error minimization. *Phys. Rev. X*, 7:021050, Jun 2017.

- [238] Abhinav Kandala, Kristan Temme, Antonio D. Córcoles, Antonio Mezzacapo, Jerry M. Chow, and Jay M. Gambetta. Error mitigation extends the computational reach of a noisy quantum processor. *Nature*, 567(7749):491–495, Mar 2019.
- [239] Tudor Giurgica-Tiron, Yousef Hindy, Ryan LaRose, Andrea Mari, and William J. Zeng. Digital zero noise extrapolation for quantum error mitigation. In *2020 IEEE International Conference on Quantum Computing and Engineering (QCE)*, pages 306–316, 2020.
- [240] Charles H Bennett and David P DiVincenzo. Quantum information and computation. *Nature*, 404(6775):247–255, 2000.
- [241] Xiao-Song Ma, Thomas Herbst, Thomas Scheidl, Daqing Wang, Sebastian Kropatschek, William Naylor, Bernhard Wittmann, Alexandra Mech, Johannes Kofler, Elena Anisimova, et al. Quantum teleportation over 143 kilometres using active feed-forward. *Nature*, 489(7415):269–273, 2012.
- [242] Ryszard Horodecki, Paweł Horodecki, Michał Horodecki, and Karol Horodecki. Quantum entanglement. *Reviews of modern physics*, 81(2):865, 2009.
- [243] Mark Srednicki. Entropy and area. *Phys. Rev. Lett.*, 71:666–669, Aug 1993.
- [244] J. Eisert, M. Cramer, and M. B. Plenio. Colloquium: Area laws for the entanglement entropy. *Rev. Mod. Phys.*, 82:277–306, Feb 2010.
- [245] M B Hastings. An area law for one-dimensional quantum systems. *Journal of Statistical Mechanics: Theory and Experiment*, 2007(08):P08024, aug 2007.
- [246] Pasquale Calabrese and John Cardy. Entanglement entropy and quantum field theory. *Journal of Statistical Mechanics: Theory and Experiment*, 2004(06):P06002, jun 2004.
- [247] Pasquale Calabrese and John Cardy. Entanglement entropy and conformal field theory. *Journal of Physics A: Mathematical and Theoretical*, 42(50):504005, dec 2009.
- [248] Christoph Holzhey, Finn Larsen, and Frank Wilczek. Geometric and renormalized entropy in conformal field theory. *Nuclear Physics B*, 424(3):443–467, 1994.
- [249] G. Vidal, J. I. Latorre, E. Rico, and A. Kitaev. Entanglement in quantum critical phenomena. *Phys. Rev. Lett.*, 90:227902, Jun 2003.
- [250] J. I. Latorre, E. Rico, and G. Vidal. Ground state entanglement in quantum spin chains. *Quantum Info. Comput.*, 4(1):48–92, jan 2004.

- [251] J I Latorre and A Riera. A short review on entanglement in quantum spin systems. *Journal of Physics A: Mathematical and Theoretical*, 42(50):504002, dec 2009.
- [252] Luca Bombelli, Rabinder K. Koul, Joochan Lee, and Rafael D. Sorkin. Quantum source of entropy for black holes. *Phys. Rev. D*, 34:373–383, Jul 1986.
- [253] Xi Dong. The gravity dual of rényi entropy. *Nature communications*, 7(1):1–6, 2016.
- [254] Shinsei Ryu and Tadashi Takayanagi. Holographic derivation of entanglement entropy from the anti-de sitter space/conformal field theory correspondence. *Phys. Rev. Lett.*, 96:181602, May 2006.
- [255] Mark Van Raamsdonk. Building up spacetime with quantum entanglement. *General Relativity and Gravitation*, 42(10):2323–2329, oct 2010.
- [256] J. Maldacena and L. Susskind. Cool horizons for entangled black holes. *Fortschritte der Physik*, 61(9):781–811, 2013.
- [257] Luigi Amico, Rosario Fazio, Andreas Osterloh, and Vlatko Vedral. Entanglement in many-body systems. *Rev. Mod. Phys.*, 80:517–576, May 2008.
- [258] Pasquale Calabrese, John Cardy, and Benjamin Doyon. Entanglement entropy in extended quantum systems. *J. Phys. A*, 42(50):500301, 2009.
- [259] Nicolas Laflorencie. Quantum entanglement in condensed matter systems. *Physics Reports*, 646:1–59, 2016.
- [260] Zhe-Xuan Gong, Michael Foss-Feig, Fernando G. S. L. Brandão, and Alexey V. Gorshkov. Entanglement area laws for long-range interacting systems. *Phys. Rev. Lett.*, 119:050501, Jul 2017.
- [261] Tomotaka Kuwahara and Keiji Saito. Area law of noncritical ground states in 1d long-range interacting systems. *Nature Communications*, 11(1):4478, Sep 2020.
- [262] Silvia Pappalardi, Angelo Russomanno, Bojan Žunkovič, Fernando Iemini, Alessandro Silva, and Rosario Fazio. Scrambling and entanglement spreading in long-range spin chains. *Phys. Rev. B*, 98:134303, Oct 2018.
- [263] Alessio Lerose and Silvia Pappalardi. Origin of the slow growth of entanglement entropy in long-range interacting spin systems. *Phys. Rev. Research*, 2:012041, Feb 2020.
- [264] Alessio Lerose and Silvia Pappalardi. Bridging entanglement dynamics and chaos in semiclassical systems. *Phys. Rev. A*, 102:032404, Sep 2020.

- [265] Guido Giachetti and Nicolò Defenu. Entanglement propagation and dynamics in non-additive quantum systems. *Scientific Reports*, 13(1):12388, Jul 2023.
- [266] Silvia Pappalardi, Pasquale Calabrese, and Giorgio Parisi. Entanglement entropy of the long-range dyson hierarchical model. *Journal of Statistical Mechanics: Theory and Experiment*, 2019(7):073102, jul 2019.
- [267] Yaodong Li, Xiao Chen, and Matthew P. A. Fisher. Quantum zeno effect and the many-body entanglement transition. *Phys. Rev. B*, 98:205136, Nov 2018.
- [268] Brian Skinner, Jonathan Ruhman, and Adam Nahum. Measurement-induced phase transitions in the dynamics of entanglement. *Phys. Rev. X*, 9:031009, Jul 2019.
- [269] Amos Chan, Rahul M. Nandkishore, Michael Pretko, and Graeme Smith. Unitary-projective entanglement dynamics. *Phys. Rev. B*, 99:224307, Jun 2019.
- [270] Xiangyu Cao, Antoine Tilloy, and Andrea De Luca. Entanglement in a fermion chain under continuous monitoring. *SciPost Phys.*, 7:024, 2019.
- [271] Michael J. Gullans and David A. Huse. Dynamical purification phase transition induced by quantum measurements. *Phys. Rev. X*, 10:041020, Oct 2020.
- [272] Xhek Turkeshi, Alberto Biella, Rosario Fazio, Marcello Dalmonte, and Marco Schiró. Measurement-induced entanglement transitions in the quantum ising chain: From infinite to zero clicks. *Phys. Rev. B*, 103:224210, Jun 2021.
- [273] O. Alberton, M. Buchhold, and S. Diehl. Entanglement transition in a monitored free-fermion chain: From extended criticality to area law. *Phys. Rev. Lett.*, 126:170602, Apr 2021.
- [274] Shenglong Xu. Long-range coupling affects entanglement dynamics. *Physics*, 15:2, 2022.
- [275] Takaaki Minato, Koudai Sugimoto, Tomotaka Kuwahara, and Keiji Saito. Fate of measurement-induced phase transition in long-range interactions. *Phys. Rev. Lett.*, 128:010603, Jan 2022.
- [276] Maxwell Block, Yimu Bao, Soonwon Choi, Ehud Altman, and Norman Y. Yao. Measurement-induced transition in long-range interacting quantum circuits. *Phys. Rev. Lett.*, 128:010604, Jan 2022.
- [277] T. Müller, S. Diehl, and M. Buchhold. Measurement-induced dark state phase transitions in long-ranged fermion systems. *Phys. Rev. Lett.*, 128:010605, Jan 2022.

- [278] Shraddha Sharma, Xhek Turkeshi, Rosario Fazio, and Marcello Dalmonte. Measurement-induced criticality in extended and long-range unitary circuits. *SciPost Phys. Core*, 5:023, 2022.
- [279] Pengfei Zhang, Chunxiao Liu, Shao-Kai Jian, and Xiao Chen. Universal Entanglement Transitions of Free Fermions with Long-range Non-unitary Dynamics. *Quantum*, 6:723, May 2022.
- [280] Matteo Ippoliti, Tibor Rakovszky, and Vedika Khemani. Fractal, logarithmic, and volume-law entangled nonthermal steady states via spacetime duality. *Phys. Rev. X*, 12:011045, Mar 2022.
- [281] Davide Vodola, Luca Lepori, Elisa Ercolessi, and Guido Pupillo. Long-range ising and kitaev models: phases, correlations and edge modes. *New Journal of Physics*, 18(1):015001, dec 2015.
- [282] Filiberto Ares, José G. Esteve, Fernando Falceto, and Amilcar R. de Queiroz. Entanglement in fermionic chains with finite-range coupling and broken symmetries. *Phys. Rev. A*, 92:042334, Oct 2015.
- [283] Filiberto Ares, José G. Esteve, Fernando Falceto, and Amilcar R. de Queiroz. Entanglement entropy in the long-range kitaev chain. *Phys. Rev. A*, 97:062301, Jun 2018.
- [284] Filiberto Ares, Sara Murciano, and Pasquale Calabrese. Symmetry-resolved entanglement in a long-range free-fermion chain. *Journal of Statistical Mechanics: Theory and Experiment*, 2022(6):063104, jun 2022.
- [285] Giacomo Gori, Simone Paganelli, Auditya Sharma, Pasquale Sodano, and Andrea Trombettoni. Explicit hamiltonians inducing volume law for entanglement entropy in fermionic lattices. *Phys. Rev. B*, 91:245138, Jun 2015.
- [286] Luca Lepori, Simone Paganelli, Fabio Franchini, and Andrea Trombettoni. Mutual information for fermionic systems. *Phys. Rev. Research*, 4:033212, Sep 2022.
- [287] Subir Sachdev and Jinwu Ye. Gapless spin-fluid ground state in a random quantum heisenberg magnet. *Physical review letters*, 70(21):3339, 1993.
- [288] Juan Maldacena and Douglas Stanford. Remarks on the sachdev-ye-kitaev model. *Physical Review D*, 94(10):106002, 2016.
- [289] Pengfei Zhang. Quantum entanglement in the sachdev—ye—kitaev model and its generalizations. *Frontiers of Physics*, 17(4):43201, Apr 2022.
- [290] Chunxiao Liu, Xiao Chen, and Leon Balents. Quantum entanglement of the sachdev-ye-kitaev models. *Phys. Rev. B*, 97:245126, Jun 2018.

- [291] Wenbo Fu and Subir Sachdev. Numerical study of fermion and boson models with infinite-range random interactions. *Phys. Rev. B*, 94:035135, Jul 2016.
- [292] Yichen Huang and Yingfei Gu. Eigenstate entanglement in the sachdev-ye-kitaev model. *Phys. Rev. D*, 100:041901, Aug 2019.
- [293] Pengfei Zhang, Chunxiao Liu, and Xiao Chen. Subsystem Rényi entropy of thermal ensembles for SYK-like models. *SciPost Phys.*, 8:094, 2020.
- [294] Arijit Halder, Surajit Bera, and Sumilan Banerjee. Rényi entanglement entropy of fermi and non-fermi liquids: Sachdev-ye-kitaev model and dynamical mean field theories. *Phys. Rev. Research*, 2:033505, Sep 2020.
- [295] M. Ghasemi Nezhadhighi and M. A. Rajabpour. Entanglement entropy in long-range harmonic oscillators. *Europhysics Letters*, 100(6):60011, jan 2013.
- [296] Shraddha Sharma, Simon B. Jäger, Rebecca Kraus, Tommaso Roscilde, and Giovanna Morigi. Quantum critical behavior of entanglement in lattice bosons with cavity-mediated long-range interactions. *Phys. Rev. Lett.*, 129:143001, Sep 2022.
- [297] José I. Latorre, Román Orús, Enrique Rico, and Julien Vidal. Entanglement entropy in the lipkin-meshkov-glick model. *Phys. Rev. A*, 71:064101, Jun 2005.
- [298] Julien Vidal, Sébastien Dusuel, and Thomas Barthel. Entanglement entropy in collective models. *Journal of Statistical Mechanics: Theory and Experiment*, 2007(01):P01015, jan 2007.
- [299] Román Orús, Sébastien Dusuel, and Julien Vidal. Equivalence of critical scaling laws for many-body entanglement in the lipkin-meshkov-glick model. *Phys. Rev. Lett.*, 101:025701, Jul 2008.
- [300] José A Carrasco, Federico Finkel, Artemio González-López, Miguel A Rodríguez, and Piergiulio Tempesta. Generalized isotropic lipkin–meshkov–glick models: ground state entanglement and quantum entropies. *Journal of Statistical Mechanics: Theory and Experiment*, 2016(3):033114, mar 2016.
- [301] Meenu Kumari and Álvaro M. Alhambra. Eigenstate entanglement in integrable collective spin models. *Quantum*, 6:701, April 2022.
- [302] Michael E. Fisher and Robert E. Hartwig. *Toeplitz Determinants: Some Applications, Theorems, and Conjectures*, pages 333–353. John Wiley & Sons, Ltd, 1969.
- [303] Estelle L. Basor and Kent E. Morrison. The fisher-hartwig conjecture and toeplitz eigenvalues. *Linear Algebra and its Applications*, 202:129–142, 1994.

- [304] Ingo Peschel. Calculation of reduced density matrices from correlation functions. *Journal of Physics A: Mathematical and General*, 36(14):L205, mar 2003.
- [305] B-Q Jin and Vladimir E Korepin. Quantum spin chain, toeplitz determinants and the fisher—hartwig conjecture. *Journal of statistical physics*, 116(1):79–95, 2004.
- [306] AR Its, F Mezzadri, and MY2443301 Mo. Entanglement entropy in quantum spin chains with finite range interaction. *Communications in mathematical physics*, 284(1):117–185, 2008.
- [307] Harold Widom. Asymptotic behavior of block toeplitz matrices and determinants. *Advances in Mathematics*, 13(3):284–322, 1974.
- [308] Harold Widom. Asymptotic behavior of block toeplitz matrices and determinants. ii. *Advances in Mathematics*, 21(1):1–29, 1976.
- [309] L. Lepori, D. Vodola, G. Pupillo, G. Gori, and A. Trombettoni. Effective theory and breakdown of conformal symmetry in a long-range quantum chain. *Annals of Physics*, 374:35–66, 2016.